THESE DE DOCTORAT DE L'ETABLISSEMENT UNIVERSITE BOURGOGNE FRANCHE-COMTE

PREPAREE A L'UNIVERSITE DE FRANCHE-COMTE

Ecole doctorale n° ED 553
Carnot-Pasteur

Doctorat de Chimie

Par
Lucia LAIN AMADOR

Production of ultra-high-vacuum chambers with integrated getter thin-film coatings by electroforming

Thèse présentée et soutenue à Besançon, le 3 mai 2019

Composition du Jury

Mme. Roy Sudipta	Professor, University of Strathclyde, Glasgow	Rapporteur
M. Pollet Bruno	Professor, NTNU University, Trondheim	Rapporteur
M. Tavares Pedro	Project manager MAX IV, University of Lund, Lund	Président
M. Hihn Jean-Yves	Professor, Université de Franche-Comté, Besançon	Directeur de thèse
M. Taborelli Mauro	Section leader, CERN, Geneva	Codirecteur de thèse
Mme. Doche Marie-Laure	Senior lecturer, Université de Franche-Comté, Besançon	Codirectrice de thèse
M. Ferreira Leonel	Chemical engineer, CERN, Geneva	Invité et codirecteur

Acknowledgments

I would like to thank first of all Mauro Taborelli and Paolo Chiggiato, section and group leaders of TE-VSC-(SCC) at CERN, for giving me the opportunity to do my PhD thesis at CERN in this very interesting topic. Thanks Mauro for the regular discussions and all the support, and for reading the thesis as many times I needed. Thanks Paolo for the regular meetings and the motivation you transmitted me that was crucial at the hardest moments of the thesis.

I would also like to express my deepest gratitude to Prof. Jean-Yves Hihn, deputy head of the Utinam institute, for accepting to supervise my PhD thesis under the topic proposed by CERN. I would like to thank him for all his advices, coffees, calls during this period. He was extremelly careful and helpful. I would also like to thank Dr. Marie-Laure Doche for accepting to co-supervise the thesis and for her time and good advices.

I would like to thank Leonel Ferreira for all the support in the development of this topic as co-supervisor and for believing in it from the first moment. I would like to thank the other members of the TE-VSC-SCC section; I have been quite lucky to work with many of you, but especial thanks to Benoit, Colette, Holger, Wil, Guillaume, Pedro, Antonios, Pau, Tony, Paul, Serge, Pierre, Florent, Marc, Marcel, Danilo and Christina. I also thank the colleagues from EN-MME, who machined and measured my samples when I needed, thanks Jean-Marie, Jacky, Angelo, Miguel, Laurent, Anite, Mickael, Arthur, Elisa and Josep.

I would like to thank my friends who supported me during the months of writting: Paz, Sanne and Geneva crew. The people in the open-space deserves another big thanks for all the coffees and courage sentences and every smile you transmitted me. Most of all, I want to thank my mother, Martina and my father, Francisco, for all their support during these years abroad and my sister, Celia. Finally, a very important thanks to the person who has supported me in all moments (good or bad) these last years, thanks for all the support and caring Rodrigo.

To all of you, thank you.

Contents

List of abbreviations

AC	Alternating Current
AP	Ammonium Persulfate
AR	Aspect Ratio
ASTM	American Society for Testing and Materials
BE	Binding energy
CAD	Computer-aided Design
CERN	European Organization for Nuclear Research
CR	Cold-Rolled
Cu-OFE	Oxygen-Free Electronic Copper
Cu-OFS	Silver-Bearing Oxygen-Free Copper
DC	Direct Current
DI	DeIonized
DP	Direct Plated
E	Elastic modulus
Er	Reduced Elastic modulus
EBSD	Electron Back-Scatter Diffraction
EDX	Energy Dispersive X-ray spectroscopy
EN-AW	European standard for Wrought Aluminium
ESCA	Electron Spectroscopy for Chemical Analysis
FIB	Focused Ion Beam
Ff	Fundamental resonant frequency
G	ASTM grain size number
GDOES	Glow Discharge Optical Emission Spectrometry
GE	Gelatin
JCPDS	Joint Committee on Powder Diffraction Standards
KE	Kinetic energy

LEP	Large ElectronPositron Collider
LHC	Large Hadron Collider
ML	Monolayer
MPSA	3-Mercapto-1-PropaneSulfonic Acid
NEG	Non-Evaporable Getter
PAG	Polyalkylene glycol
PEG	Polyethylene glycol
PC	Pulsed Current
PP	Pulsed Plated
PVC	Polyvinyl Chloride
PVD	Physical Vapour Deposition
RGA	Residual Gas Analysis
RF	Radio Frequency
RT	Room Temperature
RTC	Relative Texture Coefficient
SCE	Saturated Calomel Electrode
SEM	Scanning Electron Microscopy
SEY	Secondary Electron Yield
SIMS	Secondary Ion-Mass Spectrometry
SPS	Bis(3-Sulfo-Propyl)di-Sulfite
SRF	Superconducting Radiofrequency
SS	Stainless Steel
Ta	Activation temperature
Ton	On-time in a pulse wave
Toff	Off-time in a pulse wave
TDS	Thermal Desorption Spectroscopy
TMP	Turbo Molecular Pump
TPD	Temperature Programmed Desorption
TU	Thiourea
UHV	Ultra-High Vacuum
UTM	Universal Testing Machine
UTS	Ultimate Tensile Strength
μ	Poisson's ratio
XPS	X-ray Photo-electron Spectroscopy
XRD	X-Ray Diffraction
XRF	X-Ray Fluorescence Spectroscopy
YS	Yield Strength

Thesis introduction

Large particle accelerators are used either to search for the ultimate structure and origin of matter or as powerful light sources to investigate properties of materials at the microscopic scale. Only few gas residues, a thousand of billions less pressure than in the atmosphere surrounding us, are present in the pipe where the particle beam circulates. This enables to avoid beam perturbations by collision with the gas. The ultimate pump to achieve the lowest gas pressure is a getter: a surface of a getter has the property to trap gas molecules, since they stick on it when striking its surface. The existing coating technique enables to deposit a layer of getter, ten times thinner than a hair, on the inner wall of metal pipes building the accelerator.

To achieve a better focussing and brighter light sources, the steering magnet poles should get closer and closer to the beam itself. This is only possible by shrinking the pipe diameter. Nevertheless, the available getter coating technology is based on a plasma, which cannot be sustained in such a narrow pipe. For this reason, this thesis has developed a new method, the inverted getter scheme. Firstly, the thin getter film is deposited by the usual technique on the external surface of a cylindrical core, called mandrel. Secondly, copper is deposited onto the mandrel by electro-chemical plating. In this way, a copper pipe is built around the mandrel. Thirdly, the central mandrel is dissolved chemically and the final result is a copper tube with a layer of getter inside.

The feasibility of production of electroformed vacuum chambers with integrated getter thin film coatings is presented within this work. The thesis is divided in seven chapters.

Chapter 1 overviews the history of getter pumps and getter thin film coatings. Future trends in vacuum chamber design requires the development of new coating approaches. The main motivation for this development, which is based on copper electroforming a vacuum chamber into a pre-deposited mandrel, is presented. To lay the background of the new technique, a literature review of electroforming is included.

Chapter 2 presents the main steps of the reverse coating process. The electroforming step will attach the stainless steel flanges to the tube in the same galvanic step of chamber production. Examples of different prototypes are presented.

Chapter 3 introduces the methods concerning the characterization of the TiZrV thin film coatings. Furthermore, the methods to characterize the electroformed copper are described. These will be used in the following chapters in order to evaluate the performance of the electroformed assemblies.

Chapter 4 discusses the main results concerning the developed vacuum chambers. The mechanical performance of these chambers is examined and compared to reference copper OFE values. The TiZrV coatings are characterized for topography, adhesion, crystallinity and composition. The pumping speed of the chambers is evaluated for different gases at various in-situ activation temperatures.

Chapter 5 evaluates possible sources of contamination due to the production process. Thermal desorption analysis is used to measure the impurities in the electroformed layer. XPS surface and bulk analysis help to identify the impurities in the getter thin film.

Chapter 6 studies the effect of wave modulation parameters and organic additives on the incorporation of hydrogen, as impurity in the electroformed layer. Different trapping states of hydrogen are discussed which depend in the pulse on-time. In addition, the addition of d-xylose decreases the presence of H_2 for all tested situations.

In **Chapter 7**, the transfer of technology to real-scale prototypes is discussed with the development of 2 meters length prototypes. Future developments to cope with future chamber designs are also discussed.

Finally, the conclusions of the thesis are presented and the future work on this project is considered.

1 Introduction to vacuum chambers in particle accelerators: applications, elaboration and recent trends

The history of ultra-high vacuum in particle accelerators is briefly reviewed. Storage rings demand linearly distributed pumping to limit the pressure rise due to the outgassing induced by the circulated beams and, thus, to lower influence of pressure on beam lifetime. Non-evaporable getters can provide linear pumping in the form of a strip or a thin film. Thin films are widely used at CERN, but the application in new accelerator synchrotron light sources can be limited due to the small apertures of the modern vacuum chambers. A new coating-assembly technique is proposed which relies upon the use of an aluminium sacrificial mandrel as the substrate of the getter coating and the production of the vacuum chamber by copper electroforming around it.

1.1 Vacuum in particle accelerators

Vacuum in particle accelerators aims to reduce beam-gas interactions that are responsible for machine performance limitations: lower beam lifetime, radiation, emittance growth, noise in instrumentation, etc. In addition, it sets the background for the experiments performed at the accelerator.

The first motivation to incorporate UHV technology into accelerators design came in 1956, with the invention of the storage ring based on an idea of Gerald K O'Neill [1]. In his concept, particles would be accelerated in a conventional synchroton or linac and then would be injected in a storage ring, which would consist of strongly focused guiding magnets. He estimated that the storage time of the beam would be a few seconds in the typical 1×10^{-7} torr vacuum environment. He later proposed [2] that if this pressure was reduced it could lead to a improvement in beam lifetime from seconds to hours.

The development of machines like the first proton storage ring, the Intersecting Storage Ring (ISR) built at CERN, was a milestone for UHV development [3]. New vacuum vessel designs and fabrication methods, distributed vacuum pumping schemes and surface conditioning techniques were developed. These innovations helped coping with the effect of incident synchrotron

radiation which was responsible for gas desorption from the walls.

Furthermore, two different classes of distributed pumps (ion pumps and non-evaporable getters) were developed for storage rings and had a big impact on the further development of UHV [4]. The Large Electron-Positron (LEP) at CERN [5, 6] included a distributed pumping scheme based on integrated ion pumps and incorporated Non-Evaporable getters (NEG) strips within the vacuum chamber. The NEG strips were positioned in an innovative parallel channel within the LEP vacuum chamber (the antichamber, see Figure 1.1) [6] and consisted on a 100-μm thick layer of ZrAl powder coating on a CuNi strip (NEG strip St101, provided by SAES Getters, Milan, Italy). This strip required an in-situ heating of 750 °C for about 30 minutes in order to be activated. This temperature was reached by passing a current throughout the strip. Further developments at SAES made feasible to reduce the activation temperature of the strips to 400 °C.

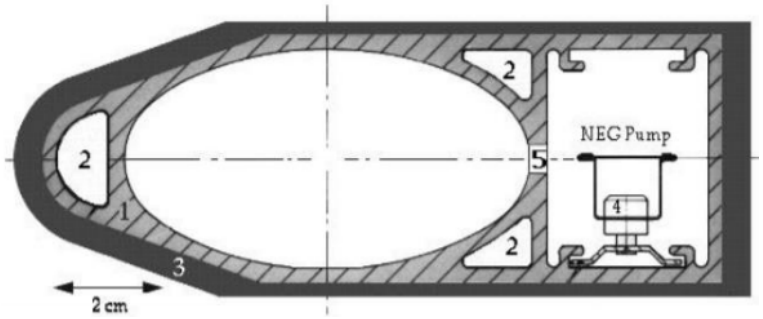

Figure 1.1. LEP vacuum chamber section made of: 1. extruded aluminium, 2. cooling water, 3. lead shield, 4. NEG strip, 5. pumping port from Grobner [7].

From this point, getter technology started to evolve in order to further decrease the activation temperatures and to move the NEG pumps from the anti-chamber closer to the vacuum walls of the beam chamber.

1.2 Getter materials

Getters are materials that are able to bind gas molecules on their surface with chemical bonds. They are classified in two families depending on the method used for the production of the active surface: evaporable and non-evaporable getters.

Evaporable getters recover a clean surface by continuous in-situ deposition of a fresh thin film. Typical materials for evaporable getters are barium and titanium. The latter is used widely in sublimation pumps for UHV applications [8]. Ti is sublimated from filaments made of Ti alloys that are heated up to 1500 °C. Once deposited, Ti films provide a sticking probability for H_2 and CO of 1-5 $\times$ 10^{-2} and 0.4-0.6, respectively, at room temperature.

Non-evaporable getters obtain an active surface by heating the material in vacuum to a characteristic temperature that leads to the diffusion of the oxygen from the surface oxide layer into the bulk. NEGs are usually produced by fixing a powder of the getter material to a metal substrate by pressing, sintering or by cathaphoresis. Usually NEGs are alloys of the elements of the IV group of the periodic table to which actinides and rare earths could be added [9]. Also aluminium is often used to increase the diffusivity of the absorbed gas species when heating.

NEG strips made of alloys of ZrAl, are activated after half an hour heating at 750 °C and provide a pumping speed for H_2 of about $2000\,\mathrm{l\,s^{-1}\,m^{-1}}$. Lowering the activation temperature of the NEG would allow a passive activation of the strips during the bake-out of the vacuum chambers. This can be achieved using the NEG Strips St707 ($Zr_{70}V_{24,6}Fe_{5,4}$ weight percentage), whose activation temperature is around 400 °C, compatible with stainless steel vacuum chamber bake-out temperature. The latter allowed a pumping speed larger than $10\,000\,\mathrm{l\,s^{-1}\,m^{-1}}$ and pressure in the 1×10^{-14} Torr range.

In addition, a new solution was proposed which involved covering the inner surface of the vacuum chamber with St707 strips (Figure 1.2). This provided both pumping efficiency, since the pump is closer to the wall, and simplified the design, since there was no need of active heating. On the contrary, the problems of chamber wall outgassing and space constraint were not solved.

Figure 1.2. Schematic view of the St-707 total NEG pump [10].

1.3 From bulk to NEG thin film getter coating

The NEG thin film coating [11–13] was a further development in UHV technology. NEG coated inner walls provide an integrated linear pumping solution for vacuum chambers with small conductance.

NEG thin film coating was deposited using magnetron sputtering techniques. Sputtering allows uniform and distributed coating of long, narrow vacuum chambers, and can produce alloys by

using composite cathodes. Many metal coatings were studied at CERN since 1999 with the main goal of reducing the activation temperature; so these coatings could also be used in aluminium alloys, which cannot be baked at temperatures higher than 200 °C [14,15]. The selected materials should have a high solubility limit and high diffusivity for oxygen [14]. A high oxygen diffusivity implies a lower activation temperature for the getter, while the high solubility enables a higher number of activation cycles and leads to a expanded lifetime of the getter. Good candidates are the elements from the IV and V column of the periodic table. The transition metals of the IV group (Ti, Zr, Hf) have a high solubility limit for oxygen while the transition metals from the V group (V, Nb, Ta) provide a high oxygen diffusivity. The goal of low activation temperature was achieved with a TiZrV alloy [12]. This alloy would be highly pyrophoric when used as a powder, but does not present this risk in the form of a thin film.

NEG thin film coatings present innumerable advantages when compared to traditional getter strips applied to vacuum chambers. These advantages are listed below.

a) Low outgassing
The getter thin film transforms the outgassing surface into a chemical pump. The coating reduces thermal outgassing of the vacuum chamber by trapping the gas coming from the underlying bulk. Furthermore, the activated thin film reduces the dynamic outgassing, which is induced by the impinging electrons, photons or ions.

b) Simplified assembly of the chamber
Before the coating development, for the application of industrial NEG strips a complex shape of the vacuum chamber was necessary to place the getter. In addition, it needed a feed-trough and power lines to be activated by resistive heating. The NEG thin film is deposited on the inner walls of the chamber, which allows simpler chamber design, and is activated in a common bake-out procedure.

c) Low secondary electron yield
Once activated, TiZrV surfaces achieve a low secondary electron yield of 1.1 [16]. This means that for every primary electron impinging in the surface, there is 1.1 secondary electrons produced from this interaction. A low secondary electron yield reduces the risk of resonant electron multiplication. The also called electron cloud is known for reducing the particle beam quality.

1.4 NEG coating process

TiZrV films are deposited via DC magnetron sputtering. This deposition method uses a process inert gas (Ar,Kr) which is partly ionized. In order to ionize the gas, a DC voltage of some hundreds of V to kV is applied between the target (cathode) and the substrate which produces a plasma consisting in ions and electrons. The charged ions are then accelerated towards the

cathode and impinge to its surface [17]. The ejected atoms from the target are condensed on the surrounding surfaces, progressively forming a thin film coating.

The minimum energy which is required to expel an atom from a target is called the sputtering threshold, and corresponds to the binding energy of the most weakly bound surface atom.

The sputtering yield is the ratio of the number of atoms that are ejected to the number of incident bombarding particles [18]. This ratio depends on the chemical bonding of the target atoms, the energy that is transferred in the collision, the incident angle of the ions and the crystal structure of the target surface. In literature [19–21], sputtering yields for Ti, Zr and V are reported for argon ions (Ar^+) and for different impinging energies. The deposition rate will depend on the sputtering yield and on the distance of the substrate to the cathode.

In the magnetron process, a magnetic field parallel to the cathode surface is added. The magnetic field is oriented so that the electrons in the glow discharge follow a cycled motion and the drift followed by them is a closed loop. This electron trapping and longer path in the gas increases the collisions between the electrons and the gas molecules. This enables to work with lower pressures and the sputtered particles cross the discharge space without collisions, resulting in high deposition rates.

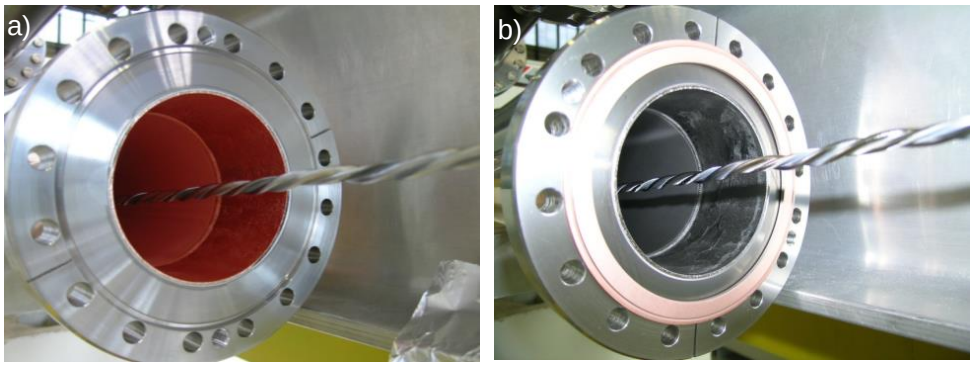

Figure 1.3. In (a) vacuum chamber before TiZrV coating. In (b) vacuum chamber after coating.

There are two main configurations for the magnetron sputtering. Planar sputtering and coaxial magnetron sputtering, also called cylindrical magnetron. For TiZrV coatings on the inner wall of beam pipes, the most used technique is the cylindrical magnetron (as seen in Figure 1.3). The cathode consists of three twisted wires of Ti, Zr and V. The alloy composition can be varied by modifying the number of wires for a given element or by modifying the diameters. The final thickness achieved by the sputtering process is typically 1.5 µm.

1.5 General properties of TiZrV films

TiZrV alloys have been extensively studied [12,13,22–24] in order to have a full understanding of the vacuum properties. Different TiZrV films were studied by changing the coating parameters or the sputtering target. The parameters under study can be summarized in:

- Elemental atomic composition
- Thin film crystallinity
- Roughness of the film
- Temperature of the coating
- Discharge gas used for coating

The effect of the bulk composition (at.%) of TiZrV alloys on the activation behavior was reported in Ref [12, 13]. For this study, the coatings were performed in the planar magnetron sputtering system and three different cathodes were used, made of Ti, Zr and V. The concentration of the three elements in the coating was varied by changing the power for each cathode individually. The samples were analyzed after the coating by Auger Electron Spectroscopy. In this case, the activation of the samples was measured by the change of the Zr MNV Auger peak, after in-situ thermal activation at different temperatures. R was calculated as the ratio of the intensity of the Zr metallic peak to the oxidized metallic peak. A high R value indicated a high degree of activation.

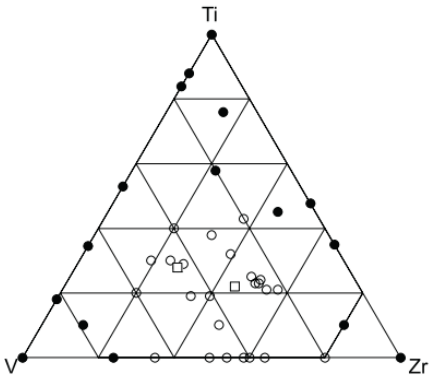

Figure 1.4. Quality composition of TiZrV coatings based on the R criteria as a function of the in-depth elemental composition (measured by EDX). The samples with a R $\geq$ 0.5 are represented by empty symbols and the samples with a R <0.5 are represented with black symbols. From Prodromides [24].

The samples are then classified between low activation and high activation temperatures (see Figure 1.4), and it can be noticed that the coatings which exhibited lower activation tempera-

tures have a composition defined in the region: Ti(10 - 40%), Zr (20 - 50%) and V (20 - 50%). In addition, compositions with higher content of V (40 - 50%) showed higher pumping speed values for H_2 when activated at 200 °C for 2 hours [24].

In addition, Prodromides et al. [22,24] found a relation between the TiZrV composition and the morphology and grain size of the coating. Two different film structures were found by tuning the composition of the coating as it is seen in Figure 1.5. Represented with close circles in the ternary diagram of Figure 1.5, are the compositions whose diffractogram (Fig. 1.5a) contains sharp well-defined diffraction peaks at 32° and 38°. On the contrary, open circles are the alloys whose diffractogram (Fig. 1.5b) contains only a broad peak around 38° which correspond to a nanocrystalline structure.

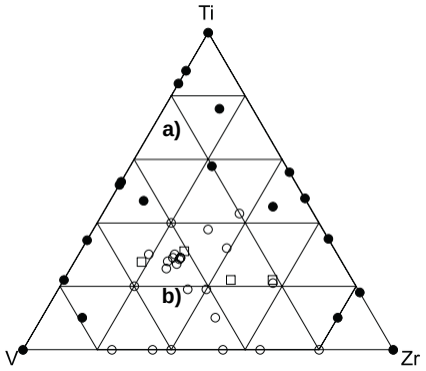

Figure 1.5. Structure composition map of TiZrV films based on the crystal average grain size. In (a) represented with black symbols, grain sizes larger than 100 nm. In (b) represented with open circles, grain size below 5 nm. From Prodromides [24].

Applying Scherrer equation (eq. 1.1), the crystallite size can be determined:

$$w = \frac{K \cdot \lambda}{\beta cos\Theta} \tag{1.1}$$

Where w is the mean size of the ordered crystalline domain, λ is the wavelength of the X-ray source, K is a dimensionless shape factor (which has a typical value of 0.9), β is the line broadening at half of the maximum intensity, after subtracting the instrumental line broadening (in radians) and θ is the Bragg angle. The average grain sizes (w) calculated from Figure 1.6a and 1.6b are 200 nm and 5 nm respectively, representing two classes of film crystallinity. Moreover, Prodromides et al. [23, 24] found that the coatings with a nanocrystalline structure (grain size < 5 nm) exhibited better pumping speed and lower activation temperatures.

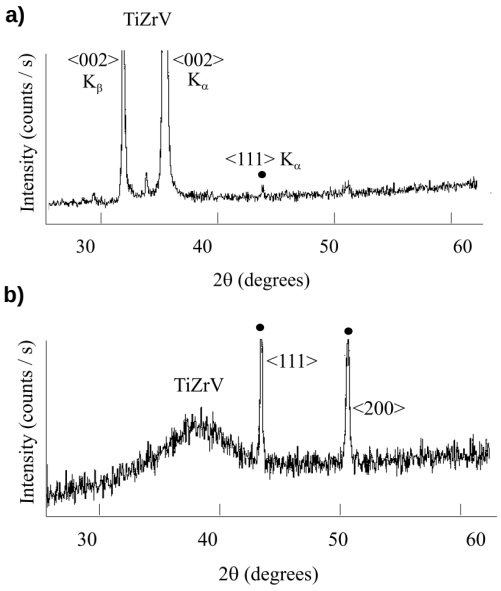

Figure 1.6. XRD diffractograms of the TiZrV thin film coatings from the regions mentioned before. In (a) thin film with grain size larger than 100 nm. In (b) thin film with a grain size below 5 nm. From Prodromides [24].

The roughness of the TiZrV coating can be increased by using a rough substrate instead of a smooth one. The influence of the TiZrV surface roughness was investigated [24], since a higher roughness increases the number of active sites (pumping sites) on the surface. Researchers found that the H_2 pumping speed and the CO sorption capacity were enhanced when the deposit showed a rough topography (as observed in Fig. 1.7b) compared to a smooth surface (Fig. 1.7a).

On the other hand, the substrate coating temperature can influence the morphology of the coating. Prodromides [24] evidenced that coatings which were sputtered on smooth copper at temperatures up to 200 °C were compact and smooth, while coatings produced at high temperatures (250-350 °C) had a higher roughness and exhibited granular-like structures (see Figure 1.8). In addition, the average grain size of the coatings produced at high temperatures (300 and 350 °C) was larger (around 10 nm) that the one which was obtained at lower coating temperatures (lower than 5 nm). For the former, the formation of a secondary phase with grains about 9 nm size was observed. The study [24] found that higher temperatures were needed in order to activate the high-temperature coatings which could be explained based on the increased grain size.

Furthermore, the sputtering process gas can be trapped into the TiZrV coating. Coatings elaborated with argon contained around 3500 ppm of the rare gas, whereas those performed with Kr exhibited two orders of magnitude lower quantity [25, 26]. Thus, krypton is normally selected as process gas since it reduces the gas released during the activation procedure. The noble gases are not pumped by the NEG coating, hence a big outgassing quantity could spoil the vacuum of the system.

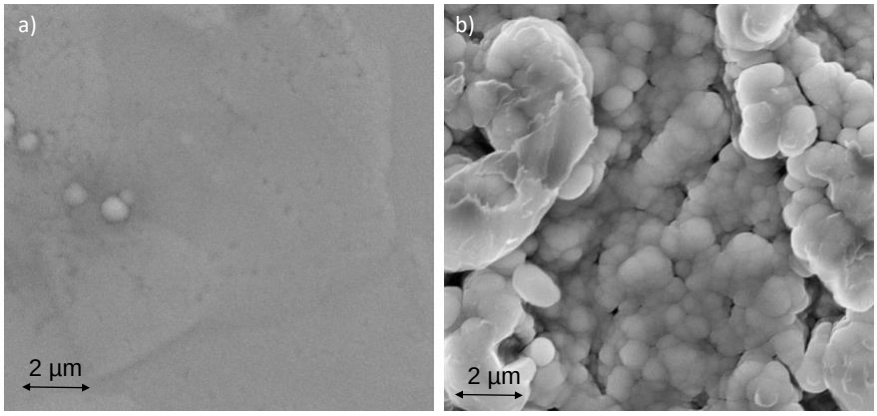

Figure 1.7. SEM micrographs of TiZrV coatings sputtered at 100 °C on smooth copper substrate (a) and on rough copper substrate (b). From Prodromides [24].

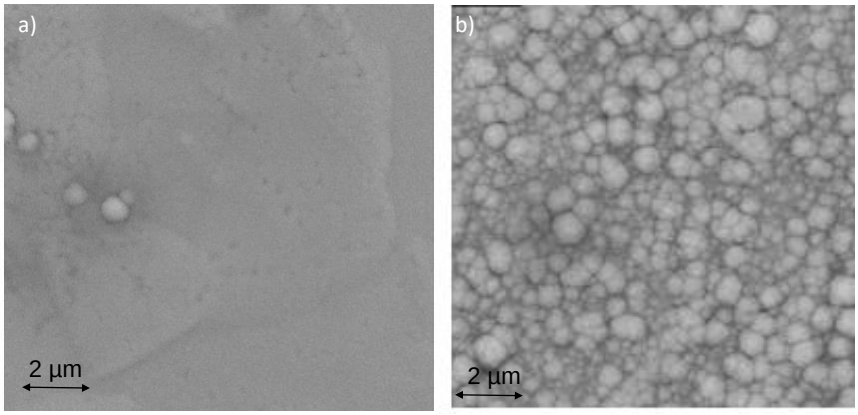

Figure 1.8. SEM micrographs of TiZrV coatings sputtered on a smooth copper surface at 100 °C (a) and at 250 °C (b). From Prodromides [24].

1.6 Vacuum properties of TiZrV films

The TiZrV film can pump the residual gases which remain in the UHV system (H_2, CO, CO_2, N_2, H_2O and O_2) by binding chemically their molecules to the surface. Noble gases are not pumped since they are not chemisorbed to the getter surface. Short-chain hydrocarbons like CH_4 are barely pumped by the NEG surface because of the high dissociation energy of these molecules on a metal surface. On the contrary, long-chain hydrocarbons could be physisorbed to the surface, as on any metallic surface, causing a contamination on the getter.

Among the gases mentioned before, H_2 and CO are the main gases which remain in the residual vacuum in accelerators. They are both captured by the NEG but in different ways. For CO molecules, the pumping mechanism is based on the chemisorption of the molecules to the getter surface. Whilst, in the case of H_2, the pumping mechanism is described as a three steps process:

- The H_2 molecule is dissociated on the getter surface
- H monoatomic is adsorbed on the surface
- H is diffused and dissolved in the bulk

The vacuum properties of TiZrV thin film getters, once activated, are evaluated in terms of pumping speed S ($\mathrm{l\,s^{-1}}$), sticking probability α, surface capacity (molecules $\mathrm{cm^{-2}}$) and ultimate pressure (mbar).

The pumping speed of a pump is defined by the ratio of the throughput of a given gas (Q, mbar $\mathrm{l\,s^{-1}}$) to the partial pressure (p, mbar) of a gas near the pump aperture:

$$S = \frac{Q}{p}(l \cdot s^{-1}) \tag{1.2}$$

The pumping speed per unit area is defined as:

$$S = \alpha C \left(l \cdot s^{-1} cm^{-2}\right) \tag{1.3}$$

Where α is the sticking probability (also called sticking factor) of a determined gas ($0 \leq \alpha \leq 1$), which is defined as the probability for a particle to be adsorbed on a surface in a simple collision and C is the conductance, expressed in ($l \cdot s^{-1} cm^{-2}$). In the molecular flow regime, the conductance does not depend on the pressure and is defined as [10]:

$$C = 3.64\sqrt{\frac{T}{M}}\left(l \cdot s^{-1} cm^{-2}\right) \tag{1.4}$$

Where T is the absolute temperature (K) and M is the molecular weight (g/mol) of the characteristic gas. Therefore, the pumping speed S of a surface can be calculated for a maximum sticking probability α=1 at room temperature: 44.1 $\mathrm{l{\cdot}s^{-1}\,cm^{-2}}$ for H_2 and 11.9 $\mathrm{l{\cdot}s^{-1}\,cm^{-2}}$ for N_2 and CO. A more detailed explanation can be found in reference [27].

Sticking factors of H_2 and CO for TiZrV coatings are summarized in Table 1.1 [24, 28]. The maximum sticking probability of standard NEG coatings were measured after heating at 230° for 24 hours. The sticking coefficients increase if the surface is rough and porous, since there is an increase in collisions on the surface and on the pores. The H_2 sticking factor is two orders of magnitude lower that the one for CO. This is explained considering that for H_2 two adsorption sites are needed to dissociate and adsorb the molecule, compared to one for CO.

Table 1.1. Summary of some functional properties of TiZrV coatings produced by standard PVD technique. From ref [29].

Property		H_2	CO
Max. sticking probability	Smooth	8×10^{-3}	0.7
	Rough	3×10^{-2}	0.9
Surface capacity (molec/cm^2)	Smooth		8×10^{14}
	Rough		8×10^{15}

The surface pumping capacity represents the total number of molecules that are pumped by the getter until it reaches saturation. The pumping speed of any gas will decrease as the coverage of the gas on the getter increases. The single exception is H_2 since it does not stay at the surface and is diffused inside the bulk, leaving the surface sites free for pumping other molecules. In table 1.1 is displayed the maximum number of CO molecules which are pumped by the getter until it reaches saturation. In addition to higher pumping speeds, a rough surface will also increase the surface capacity since the surface is larger.

The ultimate pressure is the one achievable after an in-situ bake-out, and which allows the evaluation of the NEG pumping ability when compared to the case in absence of getters. In Figure 1.9 the ultimate pressure is monitored for a TiZrV coating [26]. After 180 °C, 24 hours, the TiZrV surface is completely activated and the achieved ultimate pressure reaches a minimum. Ideally, the ultimate pressure which is achievable after the TiZrV activation would be limited only by the outgassing of CH_4 and Kr, not pumped by the NEG. However, in real situations the ultimate pressure is subjected to the outgassing of the gauges employed for the measurement and to the pumping speed available at the position of the gauge.

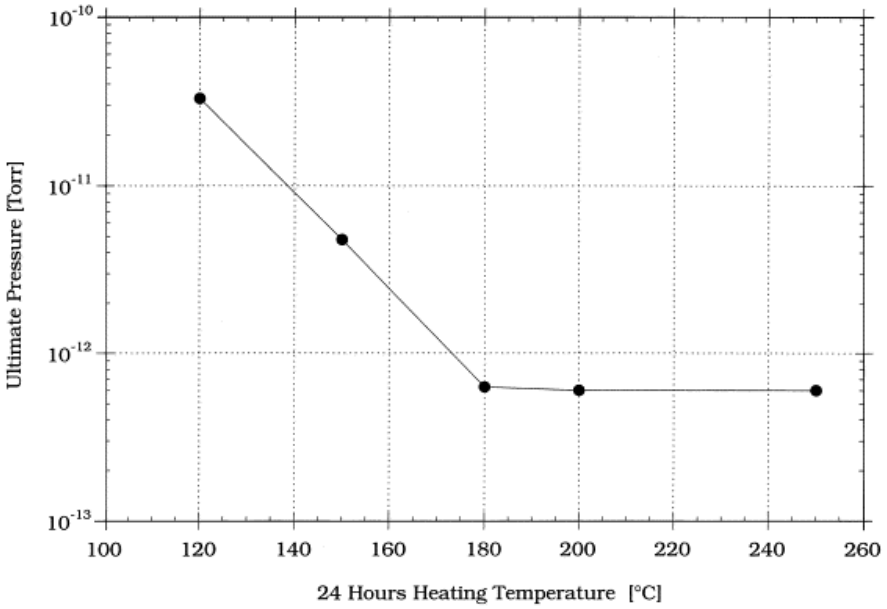

Figure 1.9. Variation of ultimate pressure, measured in a 58 mm inner diameter coated chamber, as a function of the activation temperature. The chamber is not vented to air between the baking cycles. From Benvenuti et al. [26].

When NEG coatings are used in real accelerator applications, other properties which have to be considered are:

- Particle induced desorption yield
- Performance after venting and reactivation steps

The NEG thin film during operation in a high-energy particle accelerator is subjected to bombardment of electrons, photons and ions, which can cause the desorption of a significant quantity of gas molecules [30]. On a conventional metallic surface, the source of such a gas load is expected to be linked to the oxide layer and surface contaminants. Since TiZrV coatings lack of an oxide layer (since it is dissolved during activation), it is expected that they will exhibit a low desorption yield [29]. The photon induced desorption yield of TiZrV coatings was measured by Ady [31] at KEK (Ibaraki, Japan). After several experiments, he concluded that the photon desorption yield of the activated NEG surface was one order of magnitude lower than the one of the uncoated vacuum pipes. In addition, the electron induced desorption rates of TiZrV coatings were measured for H_2 and CO [29]. The results found that the desorption yield was one order of magnitude lower than the one of uncoated stainless steel vacuum chambers baked for the same temperature and time.

Ageing occurs when the NEG is exposed to subsequent cycles of activation and air venting. For each activation, the oxygen from the surface oxide diffuses inside the bulk of the getter

material. For a TiZrV limited thickness, the process will lead to a deterioration of the film since the oxygen content in the bulk will increase after each cycle. Benvenuti et al. [26] investigated the effect of cycling on the H_2 sticking factor for a 5 µm TiZrV thin film on a stainless steel chamber. In Figure 1.10 the hydrogen sticking factor is plotted against the activation-air venting cycles. After the first activation cycle at 200 °C, the sticking factor decreases as the inverse of the number of activation cycles. However, if activations are performed at higher temperatures, the thin film deterioration can be counterbalanced.

Heating at lower temperatures does not allow oxygen to diffuse uniformly inside the film and creates an oxygen diffusion gradient close to the surface [32]. This will slow down further diffusion of oxygen from the surface and will induce the deterioration of the thin film. If higher activation temperatures are used, the oxygen diffusion is enhanced towards the bulk and the coating can recover its optimum pumping speed.

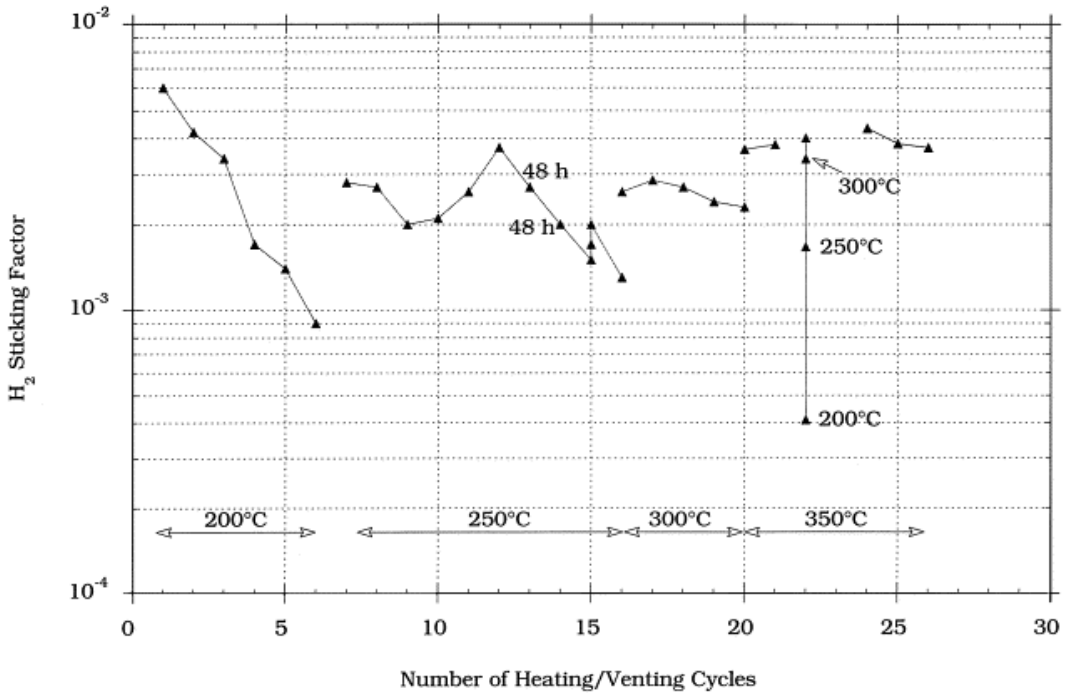

Figure 1.10. Variation of the H_2 sticking factor for a 5 µm thick TiZrV coating as a function of the number of activation-air venting cycles. The activation applied during 24 hours progressively increased to compensate for the decrease of sticking factor. From Benvenuti et al. [26].

1.7 Towards small diameter beampipes

The trend of electron accelerators towards higher energy and/or brightness at a reasonable cost has a common approach of reducing as much as possible the size of the steering magnets and their magnet bore in which the vacuum chamber is inserted with the goal of bringing the poles

of the magnet closer to the beam. From the vacuum technology point of view, this trend implies smaller diameter beam pipes and, consequently, severe conductance limitations [33, 34].

For example, the CLIC accelerator [34, 35] has a design conductance of 6-8 mm internal diameter for the beam pipes of the main-beam quadrupoles (Figure 1.11). The proposed solution is to design the vacuum chamber with two anti-chambers where NEG strips could sit and provide a distributed pumping. But this solution would not benefit of low outgassing of the vacuum chamber surface and would complicate the chamber design.

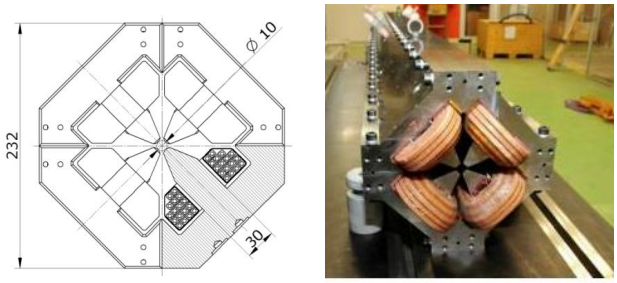

Figure 1.11. CLIC main beam quadrupole magnet [35].

In addition, several 3rd generation synchrotron light sources projects [33, 36] have started to conceive and design insertion devices for high brilliance photon sources, which have the same requirement of a small diameter vacuum chamber to bring the poles of the magnet closer to the particle beam. The main reason for this upgrade is to obtain sharp changes of magnetic field on the beam path. These are only achievable with small magnetic poles placed close to the beam [33]. In example, the MAX IV laboratory (Lund, Sweden) is designing a new high gradient permanent magnet quadrupole [36, 37], which will have a magnet aperture of 11 mm. This will reduce the internal diameter of the beam-pipe to 8-9 mm (as seen in Figure 1.12). Other example is the proposed upgrade ALS-U (Berkeley, US) in which vacuum chambers of 6 and 4 mm internal diameter are expected to be used [33, 38].

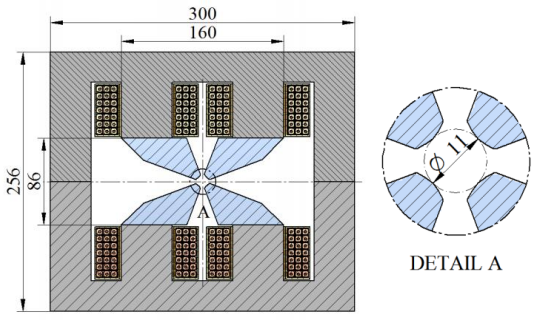

Figure 1.12. Conventional electromagnet proposed for MAXIV future upgrade [37]

The problem of removing gas in such high aspect-ratio beam pipes can be circumvented by coating the inner wall of the vacuum chamber with a NEG thin film [12, 14, 29, 39], which ensures distributed pumping speed and very low beam-induced desorption. However, the application of the NEG sputtering technique is not straightforward in such small cross section tubes whose lengths are several meters. The small diameter of the beam-pipes makes this coating technology extremely difficult, firstly because of the lack of space to insert the sputtering source, and secondly, because of the lack of space to maintain a stable and efficient plasma, as it is needed for the deposition. The practical limit is about 8-10 mm diameter. In addition, beam pipes that have non-cylindrical shapes, as for the systems where the electron and the photon beam coexist, require specific developments [28]. Studies to coat vacuum chambers with a diameter as low as 6 mm by magnetron sputtering are still in progress; [40] the development focuses mostly on the application of HiPIMS (High Power Impulse Magnetron Sputtering). However, the vacuum properties of the coating, i.e. gas sticking probability and maximum gas capacity, are not fully assessed yet.

Due to the need of an alternative, a new process called "reverse coating technique" was designed [41]. It relies on copper electroforming to build a vacuum chamber onto a pre-deposited NEG thin film coating on a sacrificial mandrel. In this method, unlike the usual process, the pipe is built from the inside out. An aluminum mandrel is coated, first, with a NEG thin film (typically 1-2 micrometers) and then with a copper film (few micrometers). Both processes are performed in the usual DC magnetron mode. This assembly is coated with a thick electroplated copper (1-1.5 mm) structural layer (as seen in Figure 1.13). At the end, the mandrel is etched away by chemical means.

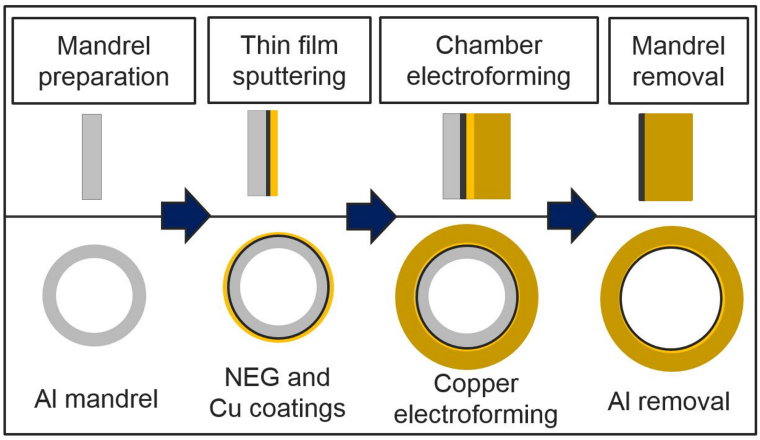

Figure 1.13. Reverse coating production process.

This technology could enable the production of cylindrical chambers of small diameter, moderate wall thickness and more complex shapes, achieving vacuum tightness, low outgassing rate, while keeping NEG pumping performances.

1.8 Copper electroforming

As discussed in Section 1.7, a possible scheme to obtain small diameter vacuum chambers with an internal NEG coating relies on electroforming to produce the vacuum chamber.

Electroformed copper is widely used in radio frequency instruments, heat exchangers, reflectors and aerospace components. Electroformed targets for a 14-MeV neutron source facility were produced using a medium-copper high acid formulation [42]. Furthermore, a 33 GHz accelerator section was electroformed starting from an aluminium mandrel [43] using copper sulphate and copper cyanide solutions. Arranz et al. [44, 45] used electroforming to manufacture the beam dump of the IFMIF-EVEDA linac. The technology helped to produce surfaces without induced stresses and copper with good mechanical properties. Furthermore, electroformed copper has also been used in the nuclear fusion field [46] for some parts of the neutral beam injection system and it was also used in the field of astrophysics detectors, with thickness in the order of 12 mm [47]. Malone et al. [48] used electroforming to develop a thrust chamber of a rocket engine. They reported an extensive study of the additives that they used in the process. Therefore according to literature, there is no limitation on the use of electroformed copper in ultra-high vacuum applications as a substitute for the conventionally used high purity copper.

Electroforming is an electrochemical deposition process which consists of a highly specialised use of electrodeposition for the manufacturing of metal parts. The process requires two electrodes (an anode and a cathode) immersed in a conducting electrolyte containing metallic salts, and a source of direct or pulsed current. During electrolysis, metallic ions in the solution i.e. Cu^{++}, are reduced on the cathode surface to form a metal layer. These result in a layer upon layer deposition to produce a continuous coating. The quantity of metal electrodeposited can be estimated with Faraday's electrolysis law (equation 1.5).

$$m = \left(\frac{Q}{F}\right)\left(\frac{M}{z}\right) \tag{1.5}$$

Where m is the deposited mass (g), Q the total electric charge (C), t is the total time that the current was applied (s), F is the Faraday constant of $96\,485\,\mathrm{C\,mol^{-1}}$, M is the molar mass of the substance $\mathrm{g\,mol^{-1}}$ and z is the valency number of ions of the substance.

Faraday's Law is an absolute law, which gives the theoretical deposited mass. It fails to take into account all the chemical or electrochemical reactions involved at the electrode. Thus, the efficiency of an electrochemical reaction can be determined:

$$\%\ Cathodic\ Efficiency = \frac{actual\ mass\ of\ deposit}{theoretical\ mass\ of\ deposit} \tag{1.6}$$

Several baths designed for copper electroforming are described in literature [49, 50], but only a few have shown to be of commercial relevance. The most frequent solutions that have been used are acid baths (copper fluoroborate, copper sulphate) and salt solutions with complexing agents (copper pyrophosphate, copper cyanide). Copper deposits from cyanide solutions are usually thin (<12.5 µm) and are not suitable for depositing thick layers for electroforming [49]. On the contrary, pyrophosphate solutions could replace high-throw acid sulphate solutions as they are heavily used for plating through holes. The only drawback is the high maintenance requirements of these baths if compared to copper sulphate solutions. Fluoroborate solutions also have the capacity of plating at very high current densities, which is desirable for copper electroforming. However, these solutions are expensive, more difficult to control and more susceptible to include impurities from the components than copper sulphate based solutions.

Copper sulphate ($CuSO_4 \cdot 5\,H_2O$) and sulfuric acid (H_2SO_4) are the main constituents of the copper sulphate acidic bath. Conventional and high-throw solutions can be prepared by variations on the composition (as seen in Table 1.2). The concentration of copper sulphate is not particularly critical, but increasing the concentration leads to a greater resistivity of the solution [51]. Changes in sulfuric acid concentration have more impact in the deposit because they affect the polarization of the electrodes. A high acid concentration (170-280 g/l) increases drastically the throwing power of the solution [52]. Furthermore, chloride ions are added to the acidic copper bath in order to produce an accelerating effect on the deposition of copper [53]. Additionally, a wide range of addition agents are often employed for brightening, hardening, grain refining and surface smoothing. This will be evaluated in Section 1.8.1.

Table 1.2. Formulations of copper sulphate acidic solutions. Retrieved from Dini [49].

Copper sulphate solution	Conventional solution	High-Throw solutions
Copper sulphate $CuSO_4\,5\,H_2O$ (g/l)	200-250	60-100
Sulfuric acid H_2SO_4 (g/l)	45-90	180-270
Chloride (mg/l)	-	50-100

Mandrels used for copper electroforming, may be classified in permanent or expendable types [54]. Various categories are given in Table 1.3.

Table 1.3. Comparison of mandrel materials. Adapted from Spencer [54].

Type	Material	Advantage	Disadvantage
Permanent	Carbon steel	Low cost	Attacked by some plating solutions
	Stainless steel	Inert to plating solutions	Costly. Soft surface
Soluble	Glass	Close tolerance, high finish	Costly. HF dissolution. Requires conductive coating.
	Aluminium	Good machinability	Costly. Soft surface.
	Plastics	Moldable. Low cost.	Inadequate for hot plating baths. Requires conductive coating.
Fusible	Low melting alloy (Pb-Sn-Bi types)	Can be cast at low cost.	Difficult to be removed.
	Waxes	Can be molded at low cost.	Easily scratched. Requires conductive coating.

Sometimes, it is desirable to have a good adherence with the mandrel. This is the case either for mandrels, which will remain as an integral part of the electroformed piece or for achieving smooth inner surfaces. Acid plating solutions because of their acidity, cannot be used to plate directly onto very active metals (materials that are easily oxidized even during rinsing and transfer). Copper electrodeposition directly on these materials produces non-adherent immersion deposits [50]. Therefore, a necessary step involving a thin electroless coating of zinc or tin is required to make the surface receptive to an adherent electrodeposit. This is the case for alloys of aluminium or magnesium. Furthermore, the electrodeposition of thin coatings from specially formulated solutions called strikes are considered stabilizing steps since they provide new, homogeneous surfaces upon which subsequent deposits are plated. Nickel Wood, copper cyanide, silver cyanide or gold cyanide strikes are used in great extent.

1.8.1 The use of additives on the electrodeposition of copper

Additives influence the plating mechanism and hence, the resulting plating deposit. Cathode polarization, plating rate, grain refinement, crystal orientation, texture and purity of the deposit are influenced by them.

Current additive mixtures involve four major components: a suppressor (typically polyalkylene glycol (PAG) type polymers with a molecular weight around 2000), an accelerator (i.e. bis(3sulfopropyl)-disodium-sulfonate (SPS)), a leveler which are typically alkane surfactants containing sulfonic acids and amine or amide functionalities and a promoter such as Cl^- ions [55].

Suppressors limit metal deposition when they are adsorbed at the copper surface and create macro-levelling. The adsorbed molecule increases the polarization resistance of the electrode and regulates the deposition of Cu ions on the cathode. Suppressors produce deposits with finer grains and help to improve the overall plating distribution.

Accelerators increase the speed of metal deposition. When they are added in the deposition process, a transition from suppression to acceleration occurs, as it activates the inhibited copper surface either by: competitive adsorption and displacement of the suppressor [56–58], or by weakening [56] the suppressor-copper bond.

In addition, levelers help to achieve an homogeneous plating thickness in the deposit as they promote deposition on less accessible areas. Finally, the bath is composed of Cl^- ions that act as a promoter and enhance suppressing or accelerating effect of other additives as PAG or SPS.

1.8.2 Morphology of the electroformed deposits

Once electroformed, the deposit can exhibit different grain structures: fine-grained, columnar, fibrous or banded. A picture of the different grain structures in represented in Figure 1.14. Coatings from copper sulphate solutions in presence of complex brighteners exhibit a fine-grained structure while deposits from sulphate solutions containing no addition agents are columnar [49]. When using stress relieving additives (such as gelatin, phenosulfonic acid or coumarin), the structure is fibrous. The latter is considered as an intermediate between the columnar and the fine-grained structures [50]. Banded structures are typical for the deposit from cyanide solutions which are less suitable for electroforming.

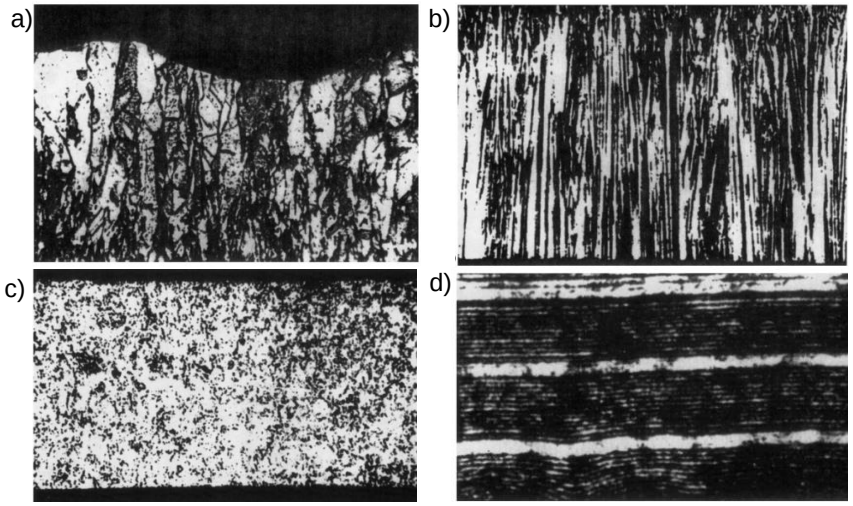

Figure 1.14. Different copper structures; cross-sectional views (500x) after etching with ferric chloride: (a) columnar (b) fibrous (c) fine grained (d) banded (From Lowemheim [59]).

In addition to the dependence of the morphology on the bath composition and additives, the grain size of a deposit will decrease as: (i) current density increases, (ii) cathode potential increases, (iii) agitation increases, (iv) solution temperature decreases and (v) metal ion concentration decreases [50].

The copper micro-structure and grain size will define the tensile strength and hardness of the deposit as the yield strength is inversely proportional to the square root of the grain diameter [60]. Table 1.4 summarizes some mechanical properties of the copper deposits [61]. Columnar deposits show lower strength but higher ductility, whereas fine-grained deposits are strong. Fibrous deposits show intermediate properties. Thus the deposits with fine-grained structures will be stronger than the others and are usually preferred for most applications.

Table 1.4. Mechanical properties of copper deposits on copper acidic sulphate solution using different additives at $4\,\mathrm{A\,dm^{-2}}$. Adapted from Safranek [61].

Structure	Tensile Strength (MPa)	Yield Strength (MPa)	Enlongation (%)
Fine-grained	490	296	7
Fibrous	345	193	20
Columnar	207	62	24

1.8.3 Impurities on electroformed copper

Impurities in electroformed copper are reported widely in literature [50, 62]. Farmer et al. [63] reported instabilities during electroformed copper heat treatment at 450 °C, when a group of proprietary additives was used in the plating, and ascribed it to the presence of voids in the deposit. By contrast, copper electroplated from another acid copper solution with different proprietary additives contained no voids and could be safely heated at 1000 °C.

Sulfur-free deposits, with carbon and nitrogen contents of about 0.015 to 0.003 and 0.001 wt%, respectively, were obtained from solutions containing polypropylene ether [64]. Other additives such as polyethylene glycol (PEG) and organo-sulfide compounds were used to electroplate wafers in which additive incorporation into the deposits was measured by secondary ion-mass spectrometry (SIMS) [65, 66]. Additive derived impurities (C, S, O and Cl) were observed after SIMS measurement, which confirmed the adsorption of brightener-derived products on the copper layer.

Kang et al. [67] studied the incorporation of PEG, SPS and Cl^- ions (used individually or mixed) in the copper deposit by SIMS. The results show that SPS is always included in the electrodeposit, while PEG is never included. They also evidenced that Cl^- ions are only included when SPS is present.

Srivasta et al. [68] found that the impurities decreased with the increase in plating temperature, the increase in acidity of the plating solution, and the addition of $0.1\,\mathrm{g\,l^{-1}}$ gelatin. Other studies found that the addition of pentoses [48, 62, 69], which act as oxygen scavengers and prevent the anodes to be oxidized, improved drastically the purity of the deposits. In Table 1.5, a summary of the copper impurity content according to different plating solutions is displayed. This will be rediscussed in Chapter 6.

Table 1.5. Impurity content (wt. ppm) of various electrodeposited copper solutions from Schuler [70].

	Content (wt. ppm)			
Plating solution	C	H	O	N
Low copper-high acid*	50	11	50	5
High copper-low acid*	190	14	50	9
d-xylose*	12	1	11	2
Pyrophosphate	21	6	140	17

* from the copper sulphate-sulfuric acid bath

1.8.4 Current modulation techniques

Pulse plating and periodic reverse plating are used to improve the deposit properties. Pulse plating operates a periodically interrupted direct current. Every short (usually a few milliseconds) cathodic current pulses is followed by a short break, where no current is applied [71]. In addition in periodic reverse plating, an additional reverse current is applied periodically. Compared to continuous direct current plating, pulse plating exploits the transient process of reactions at the electrodes.

Copper deposits produced from sulphate acid solutions by applying pulsed current often exhibit improved mechanical and physical properties, since finer grain deposits, reduced surface roughness, lower porosity and improved leveling are achieved [60, 72–74]. A detailed review of the effect of the pulse current will be presented in Chapter 6.

Lamb et al. [75], Pearson et al. [76] and Popov et al. [77] studied the application of pulse reverse current to the electrodeposition process. Lamb [75] reported that the reverse current deposits without the addition of any agent exhibited a marked reduction in grain size which yielded to a fibrous structure in comparison with a columnar structure exhibited when a direct current was applied. The mechanical properties of the reverse plated (tensile and yield strengths and hardness) increased significantly. On the contrary, Pearson [76] found that the use of reverse current increased the grain size of their deposit by an order of magnitude and reduced the deposit hardness. Popov et al [77] studied the roughness derived from the electrodeposition process and

found that the reverse plating produced deposits less smooth than when single pulse current was applied.

2 Vacuum chamber production process

The vacuum chamber production steps are described in detail: the mandrel selection, PVD coating of the mandrel, flanges preparation, copper electroforming and mandrel etching steps. Some examples of different geometries are presented.

2.1 Production process

The main steps of the production process presented in Chapter 1.7 and applied to a vacuum chamber are: the preparation of a mandrel; the mandrel thin-film coating by DC magnetron sputtering; the preparation of the flanges; the electroforming of the vacuum chamber onto the coated mandrel; and the removal of the mandrel without damaging the thin film. In principle, such a scheme can be adapted to any geometry for which a mandrel can be manufactured. A scheme of the process is represented in Figure 2.1.

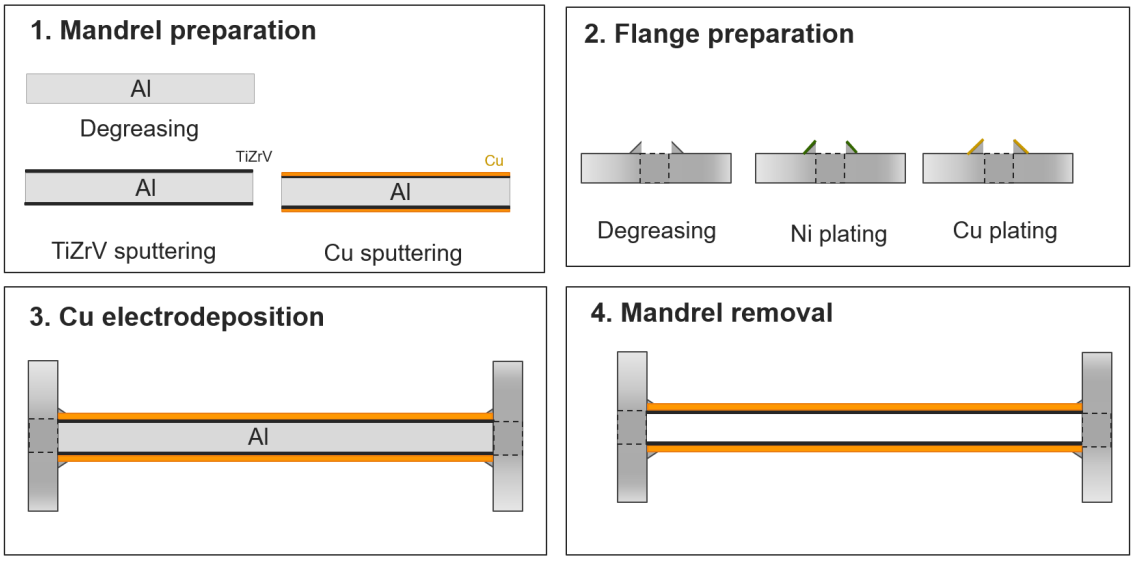

Figure 2.1. The main steps of the production process: 1. preparation of the mandrel and mandrel thin film coating by DC magnetron sputtering, 2. preparation of the flanges, 3. electroforming of the chamber and 4. removal of the mandrel without damaging the thin film.

Another point is the integration of stainless steel flanges to the vacuum chamber. During the electroforming step, adapted stainless steel flanges will be plated together with the mandrel in order to produce a leak-tight assembly.

2.2 Mandrel selection

The mandrel is sacrificial and defines the inner shape of the chamber. Therefore, candidate materials should have the following properties:

- Cheap and easy to shape
- Easy to clean for UHV cleanliness quality
- Compatible with UHV and PVD systems
- Mechanically robust
- Easy to be removed

Materials which were evaluated at the earlier stages of the process [78, 79] ranged from metallised polyimide (high-vacuum compatible, also called Kapton HN, which is metallised with 30 nm of Aluminum), BiSn alloys (low melting point alloys) and aluminium alloys. These mandrels satisfied the first three points, but the first two proposed materials failed in the last two requirements: robustness of the material and easy removal. Kapton mandrel was not stiff and also required different etching steps to ensure the mandrel removal, due to aluminium contained on the Kapton which had to be removed by dissolution in NaOH. BiSn alloy was not completely removed by melting. The best candidate materials were aluminium alloys, which are stiff and can be easily removed by chemical dissolution in NaOH. Aluminium 1050 and 6060 alloys were used equally in this study. The difference in alloy composition can be evaluated from Table 2.1.

Table 2.1. Aluminium mandrel elemental composition in wt.%.

Al type	Al	Cr	Cu	Fe	Mg	Mn	Si	Ti	Zn	Others
AW-1050	99.5% min	-	0.05% max	0.4% max	0.05% max	0.05% max	0.25% max	0.03% max	0.05% max	-
AW-6060	98 - 99.3%	0.05% max	0.1% max	0.1 - 0.3%	0.35 - 0.6%	0.1% max	0.3 - 0.6%	0.1% max	0.15% max	0.15% max

The mandrels were fabricated with the desired geometry either by extrusion of aluminium tubes or by forming and welding from an aluminium sheet. For specific studies, flat samples were produced with aluminium platelets from the same alloys. Thickness of 0.5 mm up to 1.5 mm

were used in this research and the influence of the thickness will be discussed later in the thesis. In addition, mandrels produced by additive manufacturing (3D printing) could also be used to extend the applicability of this technique.

2.3 Coating process

Prior to the coating, the mandrel is cleaned following an established procedure for UHV parts. Samples are degreased with a detergent solution (NGL 17.40 sp ALU III, concentration: 20 g/L, temperature: 60 °C) for about 15 minutes with the use of ultrasonic agitation. Afterwards they are rinsed with deionized water and ethanol, dried in a kiln at 60 °C and individually wrapped in aluminium foil for protection.

Thin film coating of the mandrel is achieved via planar DC Magnetron sputtering. A TiZrV alloy cathode (from NEYCO, $Ti_{33}Zr_{33}V_{33}$) and a copper oxygen-free disk cathode (both 15 cm in diameter) are used to sputter firstly 1.5 µm of NEG and secondly 3 µm of Cu with an average power of 365W and 380W, respectively. A rotational and translational axis is used in order to move the tubular substrates above the cathode targets and perform the coating without venting to air in between the two coating steps (as seen in figure 2.2 and 2.3). In the case of flat samples, they are positioned in a mobile holder on top of the coating targets.

The samples are placed inside the sputtering system and the latter is pumped down until high vacuum is achieved. The vacuum system is not baked before the coating and a pressure of 5×10^{-7} mbar is achieved at the end of the pump-down; Kr is used as sputtering process gas at a working pressure of about 7×10^{-4} mbar. This precise criteria must be fulfilled because a lower pressure value would not induce sufficient ionization of the gas, resulting in a low deposition rate; on the other hand, a too high pressure shortens the mean free path of the sputtered atoms, so fewer atoms are able to reach the substrate, also lowering the deposition rate.

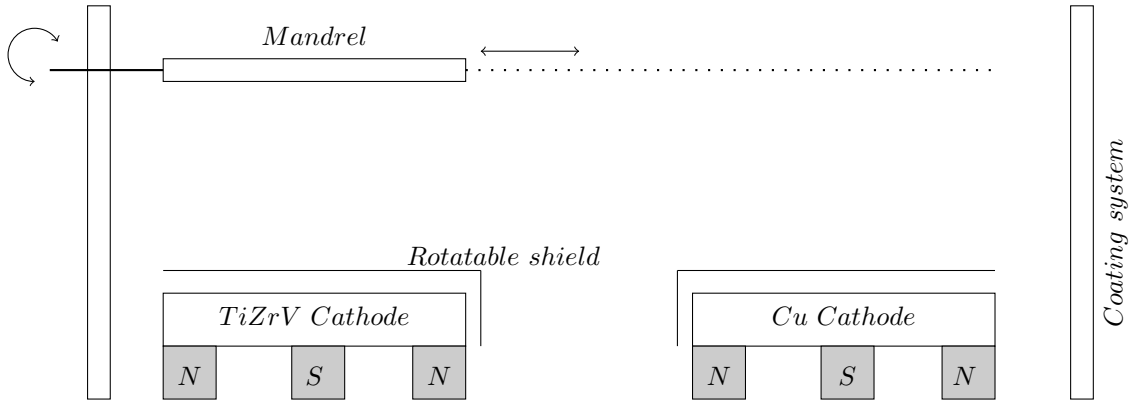

Figure 2.2. Planar magnetron sputtering process for mandrel deposition. The mandrel is the substrate of the coating and the cathodes are the sputtering targets.

Prior to the coating on the samples, the cathodes are conditioned (cleaning by sputtering) for about 15 minutes. This procedure consists of hiding the cathode beneath a shield and generating plasma, which will remove the first surface layers and with it any existing surface contamination from the target (as seen in Figure 2.2). After the conditioning, the shield is opened and the sputtered atoms can reach the substrate. During the coating, the temperature of the substrate is not controlled and no external heating is applied.

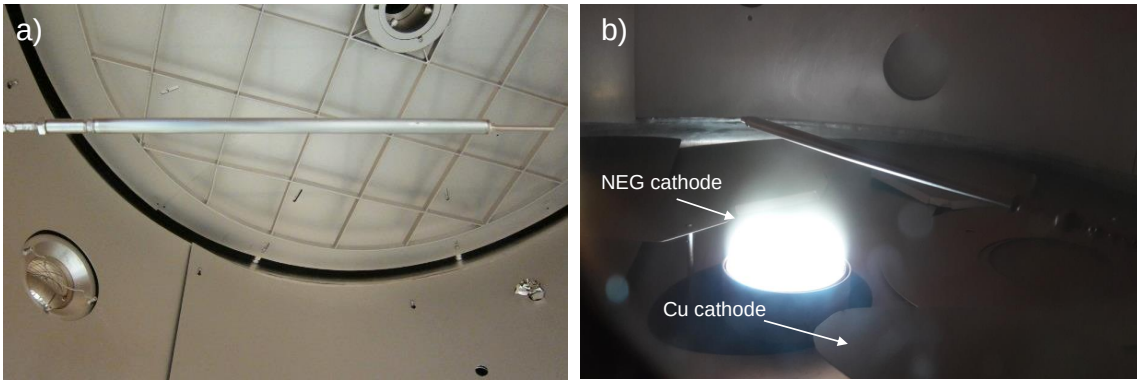

Figure 2.3. In (a) aluminium mandrel on the rotational and translational axis of the coating system. In (b) aluminium mandrel during the NEG deposition.

Immediately after the NEG coating, a layer of copper is deposited on top of the NEG to produce on the mandrel a copper external surface, which is easier to electroplate (as seen in Chapter 1.8, Ti alloys will produce a non-adherent immersion deposit). It also gives the necessary barrier between NEG and the following water based production steps, which culminate with the electroplated copper. This coating sequence is defined by the label Cu/NEG/mandrel sequence.

In addition, a second coating approach was investigated as an alternative to better protect the NEG layer during the etching of the mandrel. It relied on the deposition of a copper sputtered layer on top of the aluminium mandrel, to act as a barrier for impurities coming from the etching process of the mandrel. Afterwards, the NEG coating was performed on top of the Cu PVD coating and then a second layer of PVD copper was deposited on top of the NEG (as in the procedure described just above). This coating sequence will be described thereafter as Cu/NEG/Cu/mandrel sequence.

2.4 Flanges preparation

As previously noticed, the electroforming step should also integrate the assembly of the stainless steel flanges, thus neither electron-beam welding nor brazing is needed in the production process. This assembly is free of thermal damage and reduces the costs. In the present case, the chamber is for UHV applications and the flanges are 316LN ConFlat flanges. Dedicated DN40 or DN16 flanges were designed and machined from stainless steel blind flanges. A conical lip

profile with an angle of 26° was used to smooth the transition between the stainless steel flange and the aluminium tube as seen in Figure 2.4. Two different versions of the flanges were used within this project. Firstly the flange was machined without reducing the overall thickness of the flange (see Figure 2.4, v.1). In a second version (in Figure 2.4, v.2), the overall thickness of the flange was also reduced in order to make the conical shape more accessible for the bath.

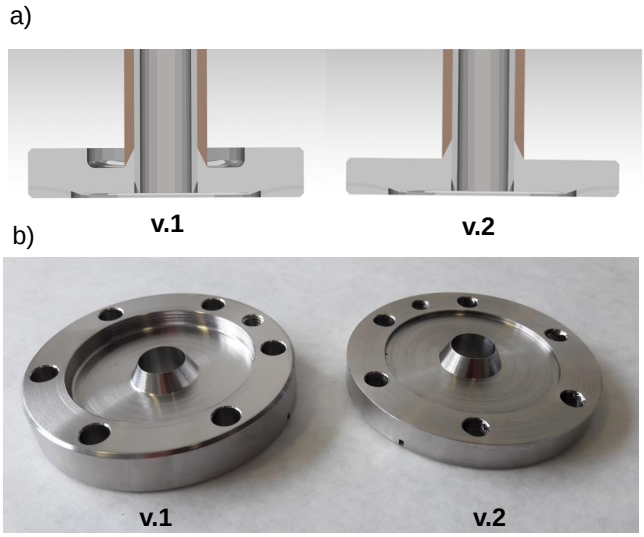

Figure 2.4. In (a) drawing of proposed flanges. In (b) stainless steel flanges after production, prior to nickel plating, for v.1 and v.2 designs.

If electroplating is made directly on stainless steel, the lack of adherence would limit the leak-tightness of the chamber. Therefore, a metal bonding is needed on the stainless steel in order to grow the copper layer. Firstly, the passivated chromium oxide layer of the stainless steel must be removed in order to create a very adherent layer. Nickel flash is used as interlayer to provide good adherence between stainless steel and plated copper. Prior to treatment, scotch tape and rubber accessories are used in order to hide areas which are not involved in the joining. After the masking, the procedure is the following: the flanges are firstly degreased in alkaline solution (40 °C, 30 min) and then degreased in an electrolytic degreasing solution (10 A dm^{-2}, 30 °C, 2 min). After that, the cleaned surface follows a surface preparation step which allows to thin and homogenise the passive layer and increase the surface roughness and an activation step. The flanges are anodically processed in a sulfuric inversion bath (20% H_2SO_4, 5 V) for 1 min and then they are activated in HCl solution (20%v) to remove the passive oxide layer. Afterwards, Nickel Wood bath is used to plate up to 3 µm of nickel on the stainless steel surface (5 A dm^{-2}, 300 g l^{-1} nickel chloride, 30 g l^{-1} H_3BO_3, 50 ml l^{-1} HCl), which will act as a metal bond layer. Afterwards, in order to give a copper finish, 3 µm of copper are plated using a copper sulphate bath (30 g l^{-1} Cu, 100 ml l^{-1} H_2SO_4, Cl^- 0.075 g l^{-1}) using 2 A dm^{-2} during 5 minutes. At the end, the mask is removed and the flanges are rinsed with deionized water and ethanol and dried in a kiln at 60 °C.

2.5 Copper electroforming process

Prior to the electroforming step, the coated aluminum mandrel is assembled mechanically with the stainless steel flanges as shown in Figure 2.5. Then the assembly is masked and prepared for plating. Two blind threaded PVC flanges are added on top and bottom of the chamber enabling the assembly of a feed-through in the shape of a copper threaded rod, which ensures the electrical contact between the mandrel and the power supply.

Once prepared, the whole assembly is degreased in alkaline solution (40 °C, 15 min) and rinsed in an acidic solution of H_2SO_4 20%. Then the electroforming step begins. The masked prototype is immersed in the acidic copper sulphate plating bath (Cu 30 g l^{-1}, H_2SO_4 165 g l^{-1}, Cl^- 0.075 g l^{-1}) as illustrated in Figure 2.6. Two copper phosphorized anodes are placed around the chamber and will undergo the anodic reaction. Prototypes are Cu electroplated using two different electroplating procedures which come from well-known workshop processes used during the last 20 years at CERN (see table 2.2).

Figure 2.5. Coated mandrel and stainless steel flanges mechanically assembled prior to electroforming.

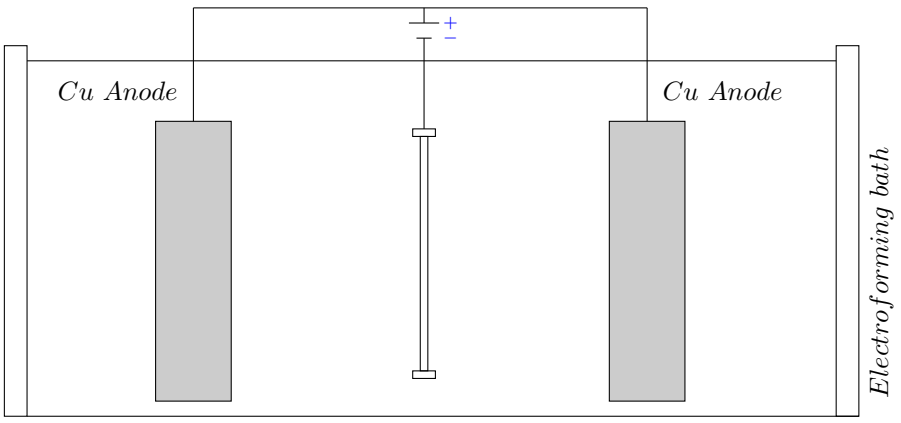

Figure 2.6. Chamber electroforming process.

Figure 2.7. Electroformed chamber with the stainless steel flanges assembled using DC plating in the bath that contains a brightener.

Electroplating of large thicknesses (>0.5 mm) can be achieved by adding a brightener to the bath. For our application copper GLEAM-PC [80] is chosen. The brightener is composed of a mixture of a suppressor, an accelerator and a promoter. The formulation of the brightener is not known but suppressors are usually polyalkylene glycol (PAG) polymers with molecular weight of at least 2000, whereas accelerators are typically propane sulfonic acids, such as bis (3-sulfopropyl) disulfite (SPS) and 3-mercapto-1-propanesulfonic acid (MPSA). The effect of the individual components of the additive in the plating was already described on section 1.8.1. The electroforming process in presence of the brightener is performed in DC mode. Direct current is applied at $2\,\mathrm{A\,dm^{-2}}$ for 40-48 hours in order to achieve a thickness between 1-1.2 mm as seen in Figure 2.7.

A second approach relies on the use of pulsed current in order to produce a thick copper deposit without the use of a brightener in the bath. The goal of this procedure is to avoid the use of any organic additives in the bath by imposing a modulated current (see Figure 2.8), which allows us to control the quality of the deposit. The average current density ($j_{average}$) is calculated with the on-time (t_{on}) and off-time (t_{off}) and the peak current density (j_c) applied as is shown in Equation 2.1 (see also Figure 2.8). The applied sequence for the electroforming includes a on-time and off-time of 7 ms and 8 ms, respectively. The applied average current density is kept to $1.7\,\mathrm{A\,dm^{-2}}$, with a peak current density of $4\,\mathrm{A\,dm^{-2}}$, for 48 hours. Possible modifications of this pulse sequences will be discussed in Chapter 6.

$$j_{average} = \frac{j_c \cdot t_{on}}{t_{on} + t_{off}} \tag{2.1}$$

Table 2.2. Bath concentrations of the two electrolytes and plating processes.

Plating process	Cu (g/l)	H_2SO_4 (g/l)	Cl- (g/l)	Gleam-PC (ml/l)
DC plating (DC)	30	186	0.075	7.5
Pulse plating (PC)	30	186	0.075	-

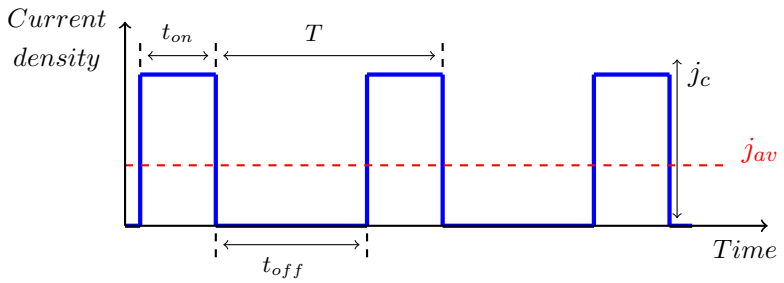

Figure 2.8. Schematic of pulse plating sequence and definition of the parameters. The pulse period, T, is the sum of t_{on} and t_{off}.

After electroforming, the copper thickness was measured along the length of the chamber either with a caliper or with a Hall-effect thickness gauge (Magna-Mike 8600). The two designs of the stainless steel flanges were evaluated, in order to assess the effect on the local electroplated thickness. The results are shown in Figure 2.9. The nominal thickness is kept constant all along the chamber with exception of the area close to the stainless steel flanges where the 26 degrees conical section starts (junction point).

There are two main observations from the results shown in Figure 2.9. First, the brightener provides a better thickness distribution along the junction point, where the tube joins the flange. If compared, the use of brightener increases the copper thickness from 30-45 % to 65-85 % of the nominal value. Second, the effect of the flange design is also observed. The flange which presents a better accessibility to the bath (v.2) exhibits 15-20 % thicker copper layer at the junction point than the alternative flange (v.1).

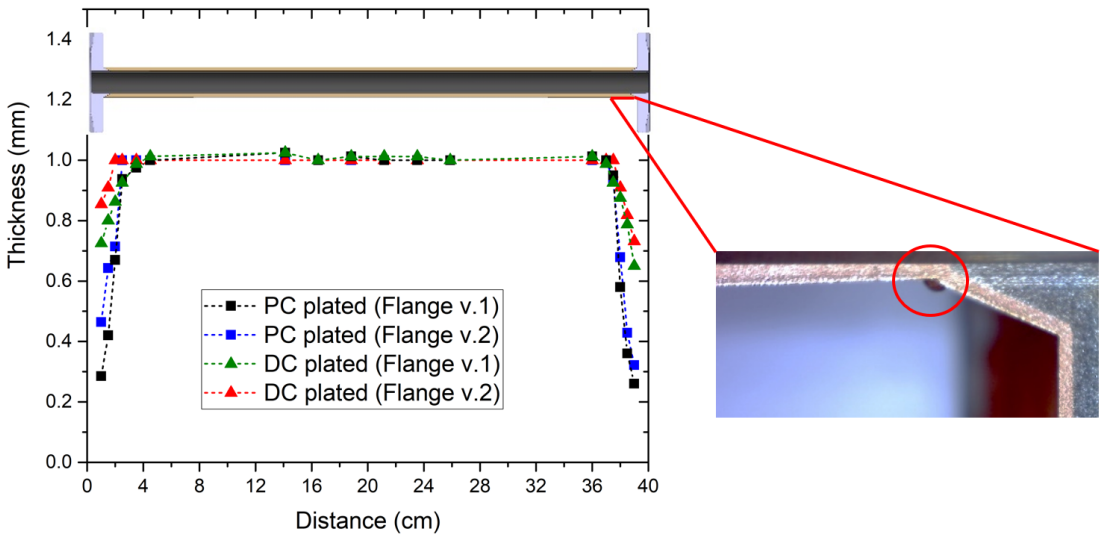

Figure 2.9. Plated copper thickness distribution along the chamber achieved with the different procedures and flanges design. On the right: image of the junction point, where the tube and the flange joins.

2.6 Mandrel removal

The electroformed assembly undergoes chemical etching to remove the aluminium mandrel. Aluminium and aluminium based alloys can be readily etched by either strong acids or strong alkaline solutions. The acid or the alkali reacts with the aluminium and removes a fraction of its surface, generating hydrogen and forming an aluminium salt. An alkaline etching solution, being more convenient and easier to control, is usually preferred with respect to an acid type etching bath [81]. In addition for our case, the solution must not attack the TiZrV thin film.

Pourbaix diagrams help to evaluate the effect of pH and electrochemical potential on the corrosion behaviour of metals [82,83]. The exposed metal can exhibit three different states: corrosion (active state), passivity (corrosion inhibited by the forming of a passive layer) or immunity (thermodynamically stable). The Pourbaix diagrams of Al, Ti, Zr, and V are presented in Appendix I.

Based on the diagrams, the pH region that dissolves the aluminium but does not affect the TiZrV thin layer is found between pH 8 and 11. D. Muehle [79] investigated the corrosion effect with solutions ranging from pH 10 to 14, using different concentrations of NaOH (1M, 2M and 5M) on TiZrV films. She concluded that in this pH range, the TiZrV layer is not attacked by the solution. Moreover, she realized that corrosion kinetics were too low to have an effect on Zr and V metals. In addition, slightly acidic solutions (pH 3) can also be used in order to rinse further the coating.

Therefore in our process, an etching solution of NaOH 5M (200g/l) is used at room temperature to dissolve the aluminium mandrel, following the reaction displayed in equation 2.2. Depending on the chamber dimensions, the procedure will switch between dipping the assembly in a bath or recirculating the solution inside the chamber as described in figure 2.11. During the etching, H_2 is produced as a reaction product. Thus, the cease of H_2 bubbles indicates the full dissolution of the mandrel. After complete removal of the aluminium mandrel, acidic rinsing is performed with amonium persulfate (200 g/l, 30 sec) in order to remove impurities from the newly appearing surface. This will be explained in detail in Chapter 5. Afterwards, the chamber is rinsed with deionized (DI) water and ethanol. After etching and rinsing, the NEG coating is visible on the inner surface of the vacuum chamber.

In the case of performing the Cu/NEG/Cu/mandrel coating sequence, ammonium persulfate (100 g/l, 15 min) was used in order to remove the protective copper layer originally sandwiched between the mandrel and the NEG film. This etching step was controlled visually, or by copper analysis of the last etching bath by means of atomic adsorption spectroscopy. All chemical etchings were performed at room temperature.

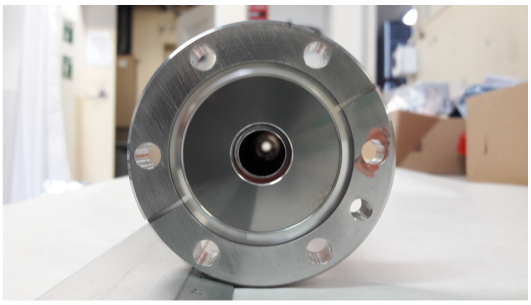

Figure 2.10. Side view of the assembled chamber before the aluminium mandrel dissolution step.

$$2Al_{(s)} + 2NaOH_{(aq)} + 2H_2O_{(aq)} \rightarrow 2NaAlO_{2(aq)} + 3H_2(g) \tag{2.2}$$

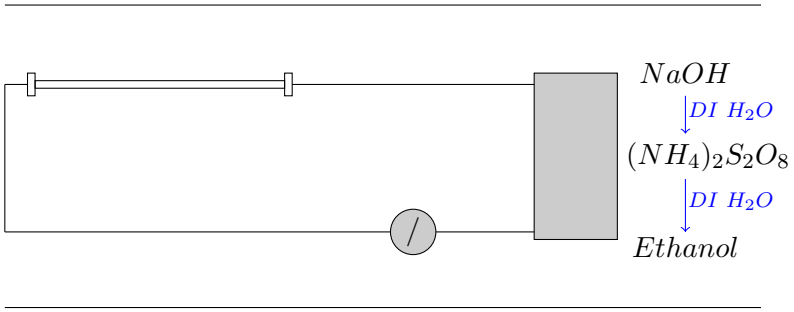

Figure 2.11. Etching chamber procedure: (1) step of aluminium dissolution with NaOH 5M and DI water rinsing;(2) step of acidic rinsing (or Cu etching) and DI water rinsing (3) step of drying with ethanol.

2.7 Example of geometries produced

Different geometries were investigated, sections starting from a 16 mm diameter tubular mandrel down to 3 mm diameter tubular mandrel. Different sets of flanges DN40 and DN16 were used for the different cases. Some examples are shown in Figures 2.12 and 2.13 and 2.14. The production process is robust for all tested geometries.

This process does not find constraints in diameter, as mandrel tubes down to 1 mm where found commercially available. A possible limit would reside in the feasibility of mandrel removal and re-circulation of the etching bath. But even capillaries could be proposed. In this thesis, the smallest coated diameter was 3 mm. Other geometries that could be produced using this technique would be bended sections and non-circular section geometries.

In addition, the maximum length achieved within this work was 2 meters. The detailed process for such a length will be explained in Chapter 7.

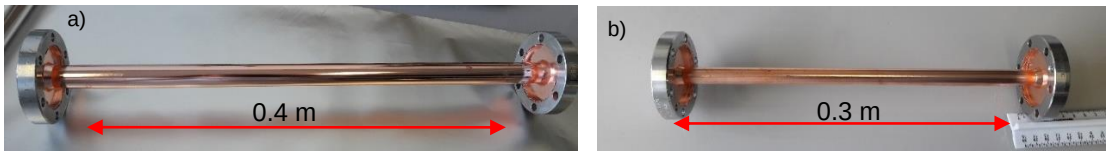

Figure 2.12. NEG coated chambers (with DN40 flanges) with internal diameters of (a) 16 mm and (b) 12 mm, (a) 400 mm and (b) 300 mm length, after production.

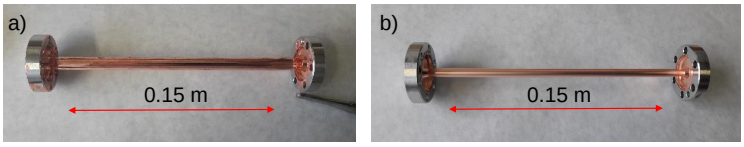

Figure 2.13. NEG coated chambers (with DN16 flanges) with internal diameters of (a) 6 mm and (b) 3 mm, 150 mm length, after production.

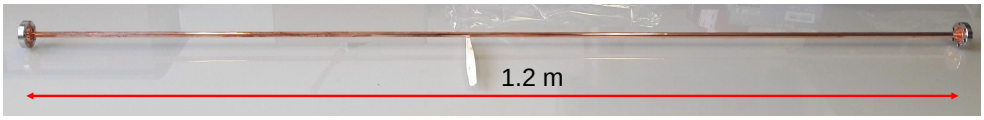

Figure 2.14. NEG coated chamber with 5 mm internal diameter, 1.2 m length, after production.

3 Characterization methods

The chapter introduces the different methods used to characterize the TiZrV thin film coatings in terms of topography, adhesion, crystallinity and composition. It also describes the methods applied for the mechanical characterization of the electroformed copper in order to assess its tensile strength, ductility and hardness. The elastic modulus of the electroformed copper is also evaluated with the impulse excitation method.

3.1 Characterization methods of thin getter coatings

3.1.1 X-ray Fluorescence Spectroscopy (XRF)

X-ray Fluorescense Spectroscopy (XRF) is used in order to determine the bulk composition and the thickness of the TiZrV coating. In the analysis, the specimen is irradiated by a primary X-radiation. The electrons from an inner electron shell are excited and as a result, electrons from higher energy shells decay to fill the existing hole and emit a corresponding fluorescence radiation. The latter is characteristic in its energy distribution for a particular material [84]. A detector is used to measure the energy of the fluorescent X-rays peaks for identification of the elements and for quantification with the given intensities. All elements but low-Z elements can be analyzed.

For the elemental composition and the thickness analysis of thin films, the observed intensities must be corrected for various factors, including the spectral intensity distribution of the incident X-rays, fluorescent yields, matrix effects and absorption, etc. Two different correction methods are used: the empirical parameters method and the fundamental parameters method. The first one needs a large number of standards of known compositions and thicknesses for the predetermination of the empirical parameters before the actual analysis. The second one uses equations derived from first principles. The equations relate intensity, composition and thickness through physical constants (fluorescent yields, atomic transition probabilities and absorption coefficients, etc.) and are solved by complex algorithms and computer iteration. The fundamental parameters method, is very suitable because it only requires a minimum number of pure or mixed element bulk standards.

3.1.2 Scanning Electron Microscopy (SEM) and combined methods

Scanning electron microscopy is used to image the coating surface [85]. Its principle relies on the analysis of emitted secondary or back scattered electrons under the impact of a focused beam of electrons. The focused electron beam is produced at the top of a column and is accelerated by the combination of lenses and apertures. The primary energy electron beam can interact with the electrons producing an inelastic scattering or with the atomic nuclei via elastic scattering. The secondary electrons are produced in-elastically with energies normally lower than 50 eV. Back scattered electrons are higher energy electrons that are mainly elastically scattered by the nuclei. The intensity of the emitted electron signal is displayed as brightness on a display monitor and the morphology of the surface is revealed (chemical homogeneity and topography).

In addition, Electron Back-Scatter Diffraction (EBSD) can be performed in order to do a microstructural and crystallographic characterization of the material. It focuses on the measurement of the back scattered electrons that are diffracted at lattice planes of the crystallites of the sample according to the Bragg's law [86]. The specimen is typically tilted to an angle of 70° with respect to the beam to allow a maximum number of backscattered electrons to exit the sample. Escaping electrons may exit near the Bragg angle and form Kikuchi bands, which correspond to each of the lattice diffracting crystal planes. Kossel cones from diffracting lattice planes are displayed by projection onto a phosphorescent screen. The obtained Kikuchi pattern is recorded by a CCD camera and compared with simulations based on crystallographic data in real time for each measurement spot.

The bulk elemental composition of TiZrV coatings can be analyzed by Energy Dispersive X-ray Spectroscopy (EDX). The EDX is normally combined with the Scanning Electron Microscope and its principle relies on the analysis of the X-rays that are emitted from a sample that has been irradiated with a focused electron beam [87]. When the sample is bombarded by the SEM's electron beam, some electrons are ejected from core shells of the atoms in the sample's surface. The resulting electron vacancies are filled by electrons from a higher energy state, and an X-ray is emitted to balance the energy difference between the two electron states. Therefore, the X-ray is characteristic of the element from which it was emitted.

3.1.3 Focused Ion Beam (FIB)

The focused ion beam technique uses a focused beam of ions to raster over the surface of a sample in a similar way as the electron beam in a scanning electron microscope. The FIB can operate with a light beam of ions for imaging, or a dense source for cutting and milling [88]. It is normally combined with SEM in order to perform high resolution non-destructive images. In our case, the beam is made of Ga^+ ions. Always prior to milling, a Pt 'strap' is deposited on top of the sample in order to preserve the surface topography profile and extract the real surface. FIB is used to mill and then SEM is used to image the profile of the TiZrV coating.

3.1.4 X-ray Diffraction (XRD)

In order to analyze the crystalline structure and grain size of the TiZrV coatings, X-ray diffraction can be used [89]. The source of X-rays is usually copper since it delivers wavelengths in the order of a few angstroms (Å) which is the typical inter-atomic planar distances in polycrystalline solids. The interaction of the incident X-rays with the sample produces constructive interference when the conditions satisfy the Bragg's law (Equation 3.1).

$$n\lambda = 2dsin(\Theta) \tag{3.1}$$

Where n is an integer representing the order of the diffraction peak, λ is the wavelength of the incident X-ray, θ is the scattering angle and d is the spacing between two parallel lattice planes (see Figure 3.1) .

The measurement is performed either using a θ -2θ configuration (Bragg-Brentano) or using a grazing incident angle in a diffractometer Siemens D5000, equipped with a copper monochromatic X-ray source. The axial and equatorial divergence should be limited by using divergence slits (Soller slits). Thanks to this, the radiation from a extended line source can be used without the generation of serious aberrations in the focus.

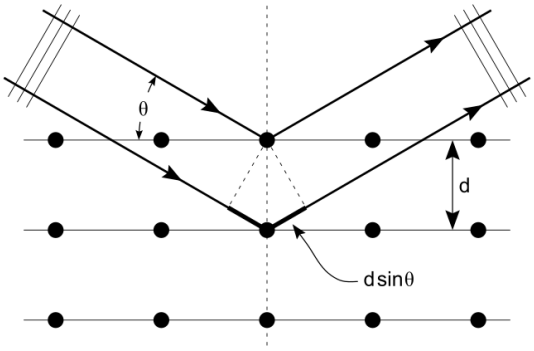

Figure 3.1. Schematic illustration of Bragg's law. From ref. [90].

3.1.5 X-ray Photo-electron spectroscopy (XPS)

The X-ray Photoelectron Spectroscopy (XPS), also called electron spectroscopy for chemical analysis (ESCA), allows the identification and quantification of surface elements (from Li to U) within the topmost 10 nm by evaluation of the characteristic binding energies [91]. It also allows to reveal the chemical environment where the respective element exists. Furthermore, it is easy to manipulate and the sample preparation is minimal [92].

The analysis is carried out by irradiating a solid with monochromatic soft X-rays and analyzing the ejected photo-electrons. For the soft X-ray source, Mg Kα or Al Kα are used. Photo-electrons are produced when an electron initially bonded with an atom is ejected by a photon and they posses a kinetic energy (KE) given by equation 3.2 (see Figure 3.2).

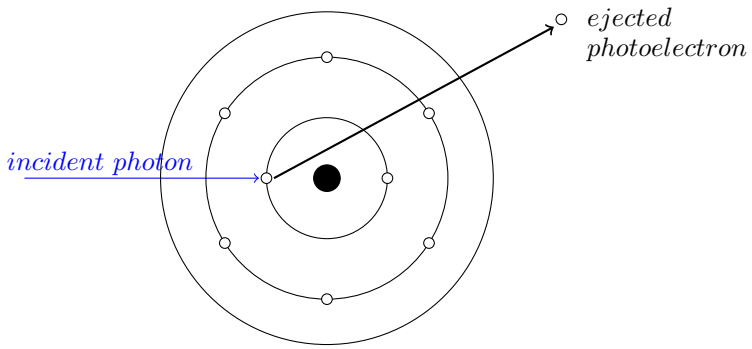

Figure 3.2. Principle of generation of photoelectrons.

$$KE = hv - BE - \phi_s \tag{3.2}$$

Where the energy of the X-ray photon is hv, the binding energy of the atomic orbital from which the electron originates is BE and the spectrometer work function ϕ_s. XPS is a surface sensitive technique because only the electrons generated near the surface escape and are detected.

The binding energy of an element is unique, and allows the XPS to identify and measure the concentrations of elements in the surface. In addition, the chemical state of the material is determined by variations in the elemental binding energy. Additional information can be given by the Auger electrons which are also emitted during the photoelectric process.

Furthermore, XPS can be used for depth profiling when an Ar ion gun is combined with a controlled sputtering process. The sample is analyzed as delivered, and afterwards it follows multiple steps of Ar^+ ion etching and successive XPS data acquisitions. XPS bulk depth profile analysis helps to analyze the presence of impurities in the bulk of the TiZrV film in the range above 0.1 at.%.

3.2 Mechanical characterization methods for electroformed copper

3.2.1 Traction and compression testing

The mechanical characterization is assessed by tensile and compression tests, where the quantities Elastic modulus (E), Yield Strength (YS), Ultimate Yield Strength (UTS), rupture strength and elongation at break are measured [93]. In Figure 3.3, a typical traction curve for metals is presented. The sample's dimension and measurement followed the standard test method for tensile testing of metallic materials (ASTM E-8) [94].

This standard further defines how the quantities must be calculated:

- The UTS is the ratio of the maximum force carried by the sample to the original cross-section of the specimen.
- The YS is usually calculated with the offset method, where it is found as the intercept of a parallel line 0.2% offset from the origin and the traction curve (see Figure 3.3).
- The rupture strength is the one at the moment of failure.
- The elongation at break is the ratio of total deformation to the initial length of the sample.

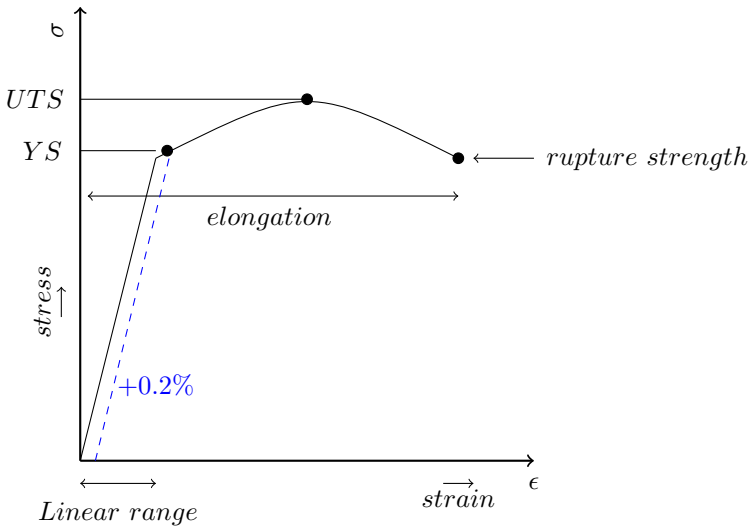

Figure 3.3. Typical stress-strain curve.

- The elastic modulus is obtained by the value of the slope on the quasilinear part of the stress vs. strain curve (as equation 3.3):

$$E = \frac{\sigma}{\epsilon} \qquad where \qquad \sigma = \frac{F}{A} \tag{3.3}$$

  Where σ is the applied stress, F is the applied force on a sample of crosssection (A) and ϵ is the strain or proportional deformation.

The most common testing machine used in tensile/compression testing is the universal testing machine (UTM). This type of machine has two crossheads; one is adjusted for the length of the sample and the other is driven to apply tension to it. A figure of this machine will be shown in Chapter 4.1.1.

3.2.2 Micro-hardness indentation testing

Indentation tests are used in mechanical engineering to determine the hardness of a material to deformation. Hardness test methods use an indenter probe that is displaced into a surface under a specific load. When testing metals, indentation hardness correlates roughly linearly with yield strength. Hardness testing is divided into two ranges: macrohardness and microhardness. Macrohardness covers testing with an applied load over 1 kg or about 10 N. Microhardness testing, with applied loads under 10 N, is typically used for smaller samples, thin specimens, plated surfaces or thin films.

The two most common micro-hardness techniques are the Knoop and Vickers hardness tests. The Knoop test uses an elongated pyramid to indent samples. This elongated pyramid creates a shallow impression, which is beneficial for measuring the hardness of brittle materials or thin components. The Vickers micro-indentation test is carried out with a diamond in the form of a square-based pyramid. The hardness scale (HV) is then determined by the ratio F/A, where F is the force applied to the diamond in kilograms-force and A is the surface area of the resulting indentation in square millimeters:

$$HV = \frac{F}{A} \approx \frac{1.8544F}{d^2} \qquad [kgf/mm^2] \tag{3.4}$$

3.2.3 Impulse excitation method

This test method determines the dynamic elastic properties of elastic materials at room temperature and follows the norm ASTM-E1876-09 [95]. The test measures the fundamental resonant frequency of test specimens with a given geometry by exciting them by a singular elastic strike with an impulse tool. The Young's modulus is computed with the measured mass, geometry and specific resonant frequency.

The resulting mechanical vibrations are sensed by a transducer and transformed to electrical signals. The latter are analyzed and the fundamental resonance frequency is isolated. The dynamic Young's modulus can be calculated if the fundamental flexure frequency is measured, which for a rectangular bar will correspond to Equation 3.5.

$$E = 0.9465 \left(m f_f^2 / b\right) \left(L^3 / t^3\right) T_1 \tag{3.5}$$

Where:
E = Young's modulus,
m = mass of the bar, g,
b = width of the bar, mm,
L = length of the bar, mm,
t = thickness of the bar, mm,
f_f = fundamental resonant frequency of bar in flexure, Hz,
T_1 = correction factor for fundamental flexural mode to account for finite thickness of bar

The correction factor T_1 is calculated with the poisson ratio (μ) as:

$$\begin{aligned} T_1 = 1 + 6.585 \left(1 + 0.0752\mu + 0.8109\mu^2\right) (t/L)^2 - 0.868 \, (t/L)^4 \\ - \left[\frac{8.340(1 + 0.2023\mu + 2.173\mu^2)(t/L)^4}{1 + 6.338(1 + 0.1408\mu + 1.536\mu^2)(t/L)^2}\right] \end{aligned} \tag{3.6}$$

In the case of a bar where the geometry (L/t $\geq$ 20), T_1 can be simplified to the following:

$$T_1 = \left[1 + 6.585(t/L)^2\right] \tag{3.7}$$

In the case of a bar where (L/t <20), T_1 can be calculated with equation 3.6 and then used to calculate E.

3.2.4 Determining the average grain size

Grain size measurement can be performed according to ASTM-E112 [96]. Prior to the measurement, the sample must be polished and micro-etched in order to reveal the grain boundaries.

The procedure is described as the following:

- Sample is mounted in graphite-charged phenolic resin.
- Sample is polished down 10 µm.
- Sample is chemically etched with etching solution N34 (5 g of $FeCl_3$, 50 ml of HCl and 100 ml H_2O) from the ASMT E407-07 [97] for a few seconds to reveal the microstructure.

ASTM grain size number (G) measurements were carried out by linear intercept procedure [96]. This method consists in the counting of intersections of the test pattern with grain boundaries on a micrograph of known magnification. This pattern was applied to at least five blindly selected and widely spaced fields. The average grain size was then determined using the table 4 in the same ASTM by correlation with the assessed G [96].

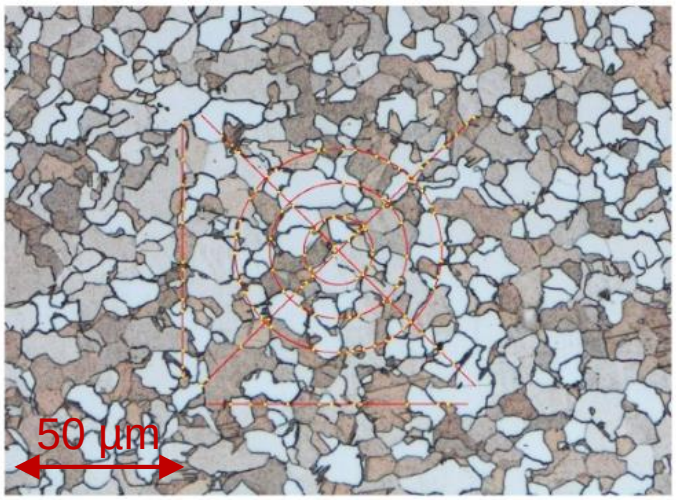

Figure 3.4. Grain boundaries revealed after the micro-etching and grain size enumeration pattern according to ASTM-E112 [96].

4 Results on chamber performance

Electroformed NEG coated chambers were successfully produced using the reverse method. The feasibility of the process was demonstrated for tubes with diameter down to 3 mm. At present, there is no other method capable of integrating a NEG coating inside chambers with such small section. In this chapter, the vacuum chambers produced by electroforming were validated in terms of mechanical resistance and leak-tigthness. Electroformed copper mechanical properties were compared with those of copper OFE and OFS, two main substrates used in UHV chambers. Additionally, the TiZrV coating was characterized for elemental composition, adherence, topography and crystallinity. Finally, the performance of the coatings was investigated by pumping speed measurements and compared to reference NEG coating values.

4.1 Mechanical characterization of the electroformed chambers

The first evaluation of the electroformed chambers concerns the mechanical stability of the assembly. The latter is critical for handling and operation procedures (i.e. mounting, dismounting, thermal cycles). Electroformed copper usually shows a wide range of mechanical properties [49, 50], as it was seen in Section 1.8.2. Grain-refined electroformed copper presents greater mechanical characteristics than columnar or fibrous plated copper and can exceed those of annealed metallurgical counterparts [98]. The ductility of electrodeposits may equal metallurgical counterparts, but is usually lower in the as-plated condition. In general, the physical properties of electrodeposits approach those of cast metals as the purity increases.

In order to validate our prototypes, different factors were taken into account. The robustness of the assembly concerning the junction with the stainless steel flanges, was evaluated directly on the produced chambers. The electroformed copper mechanical properties (elastic modulus, ultimate tensile strength, yield strength and elongation) were analyzed in produced specimens in accordance with ASTM standards. In addition, the impulse excitation technique was used to comfort the data provided by the specimens mentioned above.

4.1.1 Robustness of the assembly

The first evaluation addresses the robustness of the joining of the flanges to the copper tube. To assess it, tensile and compression tests of the electroformed prototypes were carried out with a UTM electro-mechanical testing machine equipped with a 200 kN load cell and a crosshead speed of 1 mm/min. For the tensile test, the tube was assembled on the testing machine by holding its flanges on the equipment jaws, as illustrated in Figure 4.1a. For the compression test, two planar supports on top and bottom were used as base and the chamber was placed between them, as it is seen in Figure 4.1b.

Due to the geometry of the chamber, the main measurement system was the internal load-cell displacement as it was impossible to use external measurement sensors (i.e. extensometers). It is important to note that the displacement of the load-cell was also subjected to the stiffness of the connecting flanges used to attach the chamber. As a consequence, the value of displacement can not be used quantitatively to calculate the strain and only the ultimate tensile stress will be then obtained.

Tensile tests were carried out for different DC electroformed chambers (following the procedure described in Chapter 2.5, which for this plating process includes a brightener). In addition, two different conditions were explored which will be named “non-baked” and “baked” and corresponds to after plating and after thermal annealing situations, respectively. As shown on the load-displacement curve (Figure 4.2), the non-baked chambers exhibit a ultimate tensile strength between 350 and 380 MPa. Three different trials show a good reproducibility of the results. For the annealed chambers, which were baked out at 280 °C for 24 hours, the ultimate tensile strength varies in the range between 180-220 MPa. The ultimate tensile stress quantities of the non-baked and baked chambers can be compared to Cu OFE values [99], which depending on the thermal treatment and work hardening state are: 200-250 MPa for annealed or 300-380 MPa for cold worked copper. The rupture occurs at the level of the lowest copper wall thickness (close to the flange, as seen in section 2.5), resulting in a breakdown of the copper tube just above the flange (Figure 4.3a). The chamber mechanical resistance is driven by the plated copper thickness. No delamination between the stainless steel flanges and copper chamber is detected (Figure 4.3b).

Furthermore, baked chambers were subjected to compression in the same UTM electro-mechanical testing machine. The load-displacement curve is shown in Figure 4.4. The compression behavior shows two well defined regions. First, the force drives an elastic and later plastic deformation of the plated copper in the area with lower thickness (above the flange, seen as a first region in the curve, and observed in Figure 4.5a). On the second recorded displacement, the chamber endures buckling until it collapses on the middle as is seen in Figure 4.5b. The ultimate compression stress is 178 MPa, which is very close to the ultimate tensile stress of the baked chamber. Again in this case, the stainless steel joining is maintained along the test.

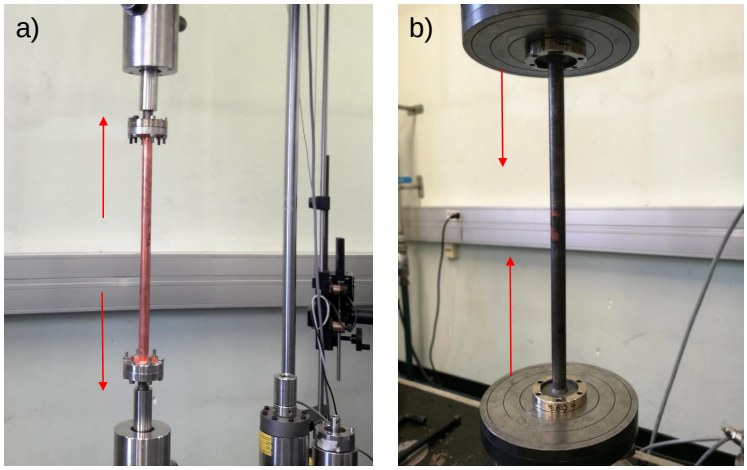

Figure 4.1. UTS electro-mechanical testing machine. In (a) tensile test set-up. In (b) compression test set-up.

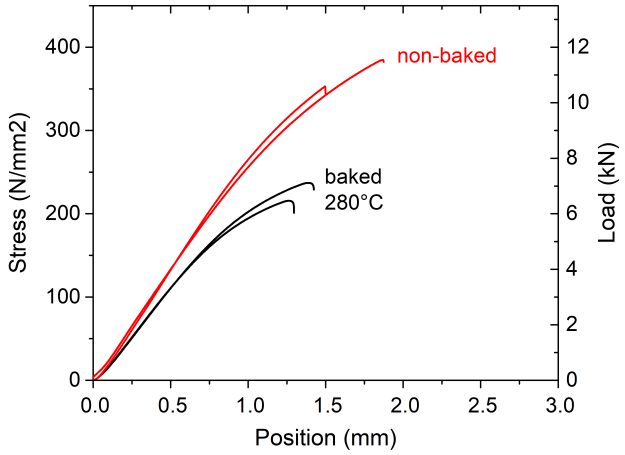

Figure 4.2. Tensile stress vs displacement curve of the non-baked and baked (280 °C) chambers.

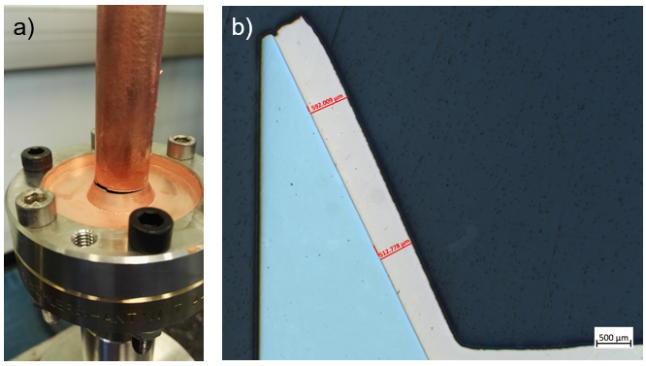

Figure 4.3. In (a) rupture after tensile test. In (b) image of the sectioned flange after rupture, where the good adherence of the nickel and copper layer on the flange is revealed.

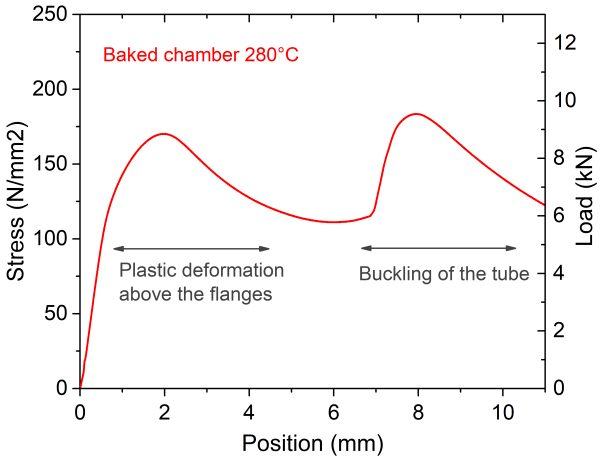

Figure 4.4. Compression stress vs displacement curve of a baked (280 °C) chamber.

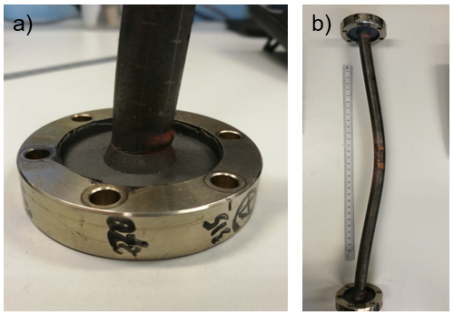

Figure 4.5. In (a) plastic deformation above the flange. In (b) buckling effect on the chamber and final plastic deformation.

Finally, the leak-tightness of the assembly when it is subjected to an external load was controlled in order to evaluate the reliability of the chamber in operational conditions (i. e. heating or cooling under vacuum). For this measurement, a leak detector was integrated in the testing machine (Figure 4.7) and the leak rate was measured at the same time as the load-displacement response of the chamber (which was a 280 °C baked chamber). The leak detector is a mass spectrometer sensitive to atomic mass 4 (for helium) that measures continuously the leak rate in $\mathrm{mbar\,l\,s^{-1}}$. If a small crack is present or forms during the test, the helium will diffuse through it and will be detected by the mass spectrometer. In addition, helium could diffuse through grain boundaries if the thickness is too low and grain size is too big.

In order to evaluate a possible leak, a helium rich volume was created around the tested chamber by flushing helium, during the measurement, inside a plastic hose that surrounded the chamber (Figure 4.7). The results of the measurement are plotted in Figure 4.6 where the initial residual leak rate is below $1 \times 10^{-10}\,\mathrm{mbar\,l\,s^{-1}}$ (detection limit of the apparatus). The load-displacement was recorded in parallel to the leak rate. The rupture of the chamber occurs at 5.8 kN which corresponds to 192 MPa ultimate strength (in the range previously stated for annealed cham-

bers). The leak-rate follows the residual background value during all the measurement until the rupture, when it abruptly rises to $1 \times 10^{-4}\,\mathrm{mbar\,l\,s^{-1}}$. The conclusion from this experiment is that the chamber is leak-tight during all the tensile elongation and plastic deformation regimes, and only looses the leak-tightness when it breaks. This means that the leak-tightness is ensured when the chamber is subjected to reasonable external loads.

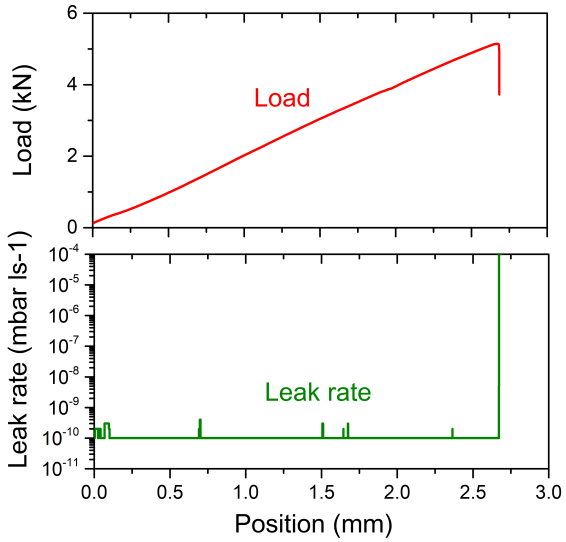

Figure 4.6. Tensile load vs displacement curve and leak rate evolution for the baked chamber.

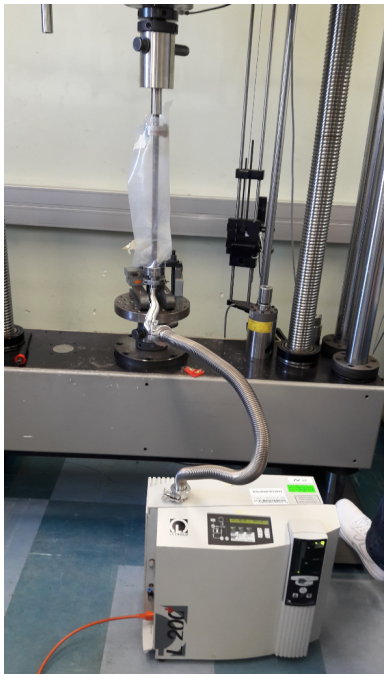

Figure 4.7. Modified set-up for the combined tensile-leak rate measurements.

4.1.2 Mechanical tensile and hardness characterization

The mechanical properties (Young's Modulus, YS, UTS and Elongation) of the electroformed copper were assessed from mechanical tests which followed ASTM standard procedures [94]. Tensile specimens made of electroforming copper were prepared, measured and compared to reference Oxygen-Free Electronic Copper (OFE) and Silver-Bearing Oxygen-Free Copper (OFS), two main copper substrates used in UHV chambers. The specimen shape was optimized following ASTM standard E8M [94, 100] and is shown in Figure 4.8.

The electroformed samples were produced from aluminium planar platelets (AW-1050, 1.5 mm thickness) which were copper coated by magnetron sputtering and then electroformed using the same plating procedures as indicated in Chapter 2.5. After electroforming, the copper plated layer peeled off from the aluminium due to stresses generated during the plating. Various specimens were prepared by precision wire-cutting. The reference samples (OFE and OFS) were produced from standard cold-rolled plates that were prepared with the same cutting technique (see Figure 4.9).

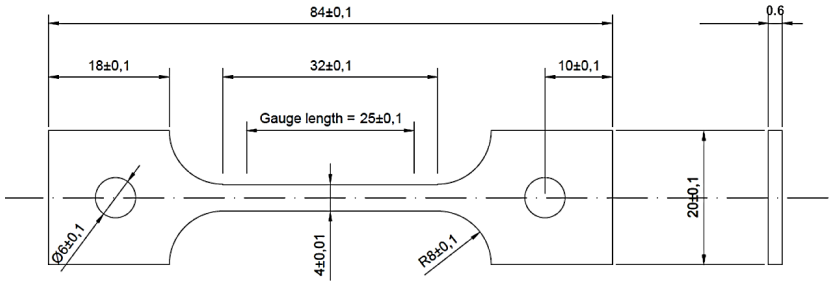

Figure 4.8. Tensile specimen dimensions (in mm) following ASTM E8M [94].

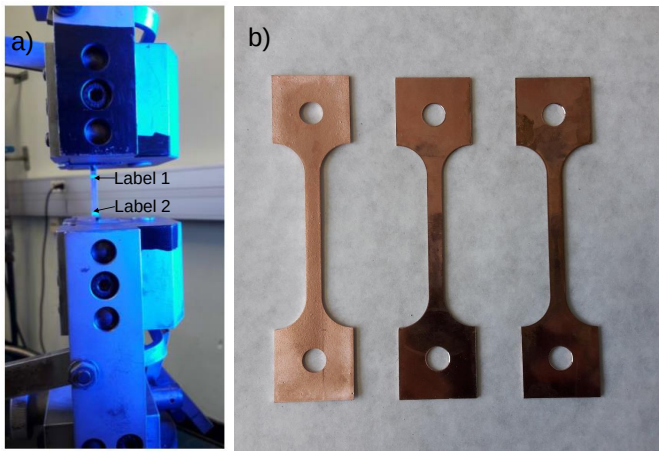

Figure 4.9. In (a) tensile test set-up for the specimens (UTM machine). On the specimen, label 1 and 2 displacement is measured by the video-extensometer. In (b) tensile specimens after machining.

The limited available space to place measurement sensors required the use of a video extensometer. The main components of the measuring system were: the internal load cell placed between the specimen (directly attached to it) and the traction rod, and the video extensometer. Two labels were fixed at the specimen gauge length and their displacement was measured by the video-extensometer as seen in Figure 4.9a.

The results of the tests are shown in Figure 4.10 and the mechanical parameters are listed in Table 4.1. The plated copper specimens exhibit a bigger standard deviation for ultimate tensile strength, yield strength and elastic modulus values, when compared with the OFE and OFS values. The electroformed copper specimens produced with DC plating in presence of Gleam-PC brightener exhibit a higher ultimate tensile strength and yield strength, but similar Youngs modulus compared to reference cold-rolled (CR) OFE and OFS copper.

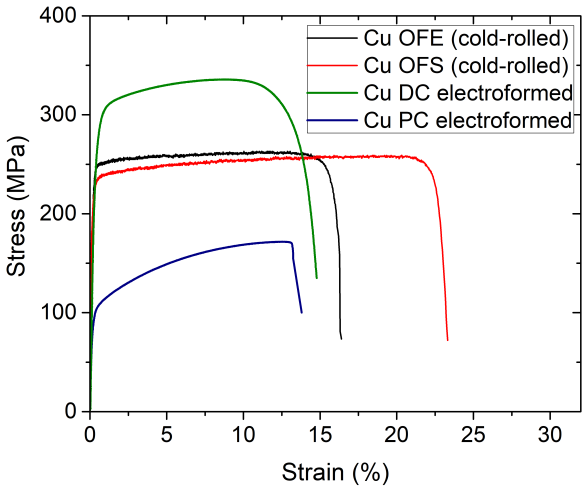

Figure 4.10. Stress vs strain curves for the different copper samples: Cu OFE in black, Cu OFS in red, Cu DC plated in green and Cu pulse plated in blue.

Table 4.1. Ultimate Tensile Strength, Yield Strength, Elongation and Elastic modulus values measured. For each case, five samples were measured.

Specimen	**UTS (MPa)**	**YS (MPa)**	**Elongation (%)**	**E (GPa)**
Cu OFE (CR)	263 ± 1	243 ± 6	16 ± 1	114 ± 1
Cu OFS (CR)	268 ± 2	237 ± 7	24 ± 2	114 ± 6
DC plated Cu	328 ± 22	268 ± 16	14 ± 3	101 ± 14
Pulsed plated Cu	170 ± 15	106 ± 10	13 ± 2	81 ± 23
Cu OFE* (350 °C, 2h)	209 ± 2	40 ± 11	35 ± 5	98 ± 2

* Annealed

The results resumed in Table 4.1 allow to put into evidence that electroformed copper when achieved by pulsed current without additives, is prone to exhibit lower values on the tested

mechanical properties. The yield strength and ultimate tensile strength are lower than the cold-rolled copper OFE ones. Pulse plated copper mechanical properties are closer to those of annealed copper OFE (350 °C for 2 hours), which is added in the Table 4.1. The pulse plated samples have similar ultimate tensile strength, but higher yield strength than the annealed ones.

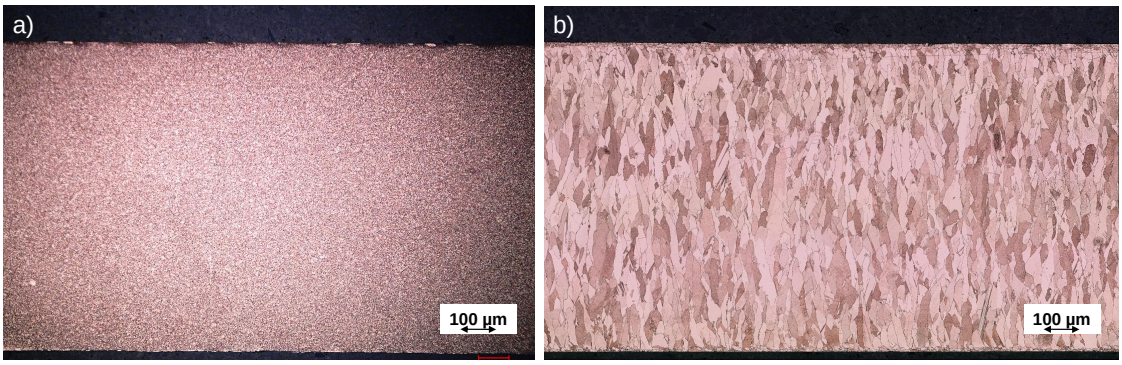

Figure 4.11. Copper microstructure revealed after micro-etching following ASTM E112 [96]. In (a) DC electroformed copper with Gleam-PC. In (b) pulsed current electroformed copper.

The micro-structure of the electroformed copper was revealed by micro-etching the surface after the samples were polished (according to ASTM E112 [96]). The differences in grain structure between the two types of electroforming is evident. DC plated samples exhibit a fine-grained structure with an average grain diameter of 1 µm, while the pulsed plated samples show columnar growth with an average grain size of 15 µm, measured following ASTM-E112 [96] in the horizontal plane. In addition, the pulse plated grains are not equiaxial, and the grain column length was estimated to be between 30 - 100 µm. For copper OFE cold-rolled, the grain size values vary between 10 - 13 µm. The grain size values explain the measured mechanical parameters via the Hall-Petch relationship (eq. 4.1).

$$YS = \sigma_i + k/\sqrt{D} \tag{4.1}$$

This relation indicates that the Yield strength of a material (YS) is equal to the frictional stress (σ_i, constant) and the inverse of the square root of the grain size (D). The smaller grains of the DC plating compared to OFE explain the better mechanical performance. In the same way, the pulse plating large grains explain the poorer mechanical behavior.

In addition, the grain micro-structure was studied using Electron Backscatter Diffraction (EBSD). The grain size was measured from Figure 4.12 by using an image processing software integrated in the system. The DC electroformed sample exhibits an average grain diameter of 1.8 ±0.6 µm. For the pulsed plated sample, which presents no equiaxial grains, the distribution of grain area represents more accurately the real grain morphology (Figure 4.13). In addition the distribution of aspect ratios is given in Figure 4.13, with an average grain aspect ratio of 2.9.

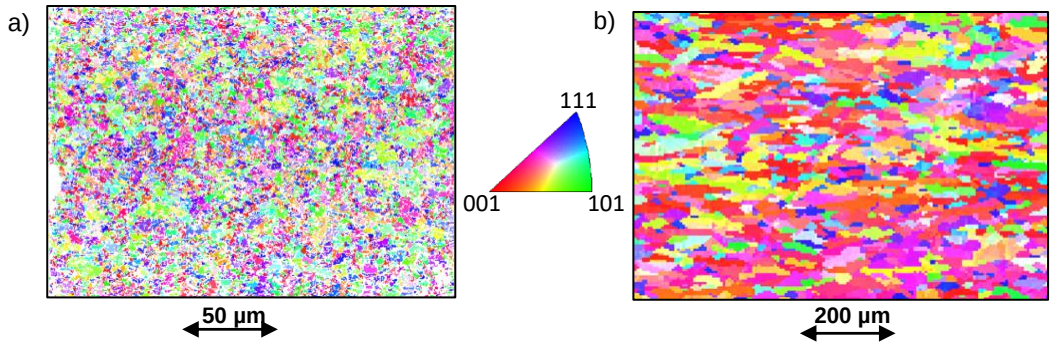

Figure 4.12. EBSD images with the corresponding crystallographic texture distribution. In (a) DC electroformed copper. In (b) pulsed current electroformed copper.

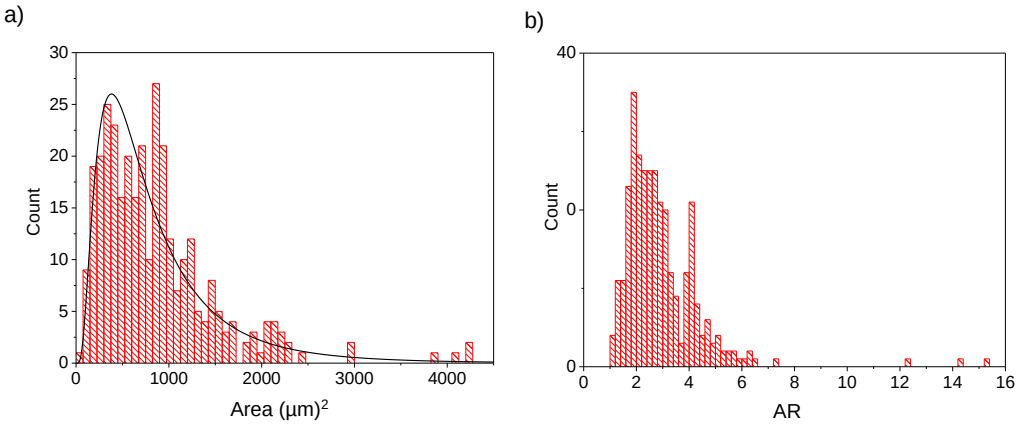

Figure 4.13. In (a) grain area distribution and in (b) grain aspect ratio (AR) for the pulse current electroformed copper. Analysis done over 324 grains.

The hardness was measured with the Vickers method [101] by micro-indentation (method described in section 3.2.2). The unit of hardness given by this test is known as the Vickers Pyramid Number (HV). The number is determined by the load over the surface area of the indentation. The results are shown in Table 4.2.

Table 4.2. Measured hardness values (HV 0.1). YS values from table 4.1 are added for comparison.

Sample	**Cu OFE (CR)**	**Cu OFS (CR)**	**Cu DC plated**	**Cu pulse plated**
Hardness (HV 0.1)	83 ± 1	90 ± 1	103 ± 2	55 ± 2
YS (MPa)*	243 ± 3	237 ± 7	268 ± 16	106 ± 10

*Values from Table 4.1

The DC electroformed copper exhibits a higher hardness than OFE, whereas pulse electroformed copper shows a lower mechanical resistance. This is in accordance with previous mechanical parameters (YS added from Table 4.1).

4.1.3 Young 's modulus by impulse excitation technique

Due high standard deviation of the Young's modulus results, the impulse excitation technique was also used to measure complementary values. The method is explained in section 3.2.3. The specimens were prepared with the two electroformed procedures discussed in Chapter 2. The specimen geometry was a plate of 8 cm x 2 cm, 1 mm thickness (specimen with constant rectangular section). The measurement was performed for a known cross-section following the standard ASTM-E1876-09 [95]. The samples were excited with a singular elastic strike with an impulse tool and the transducer picked the resulting mechanical vibrations and transformed them to electric signals. The vibration frequencies for the two electroformed copper samples are shown in Figure 4.14.

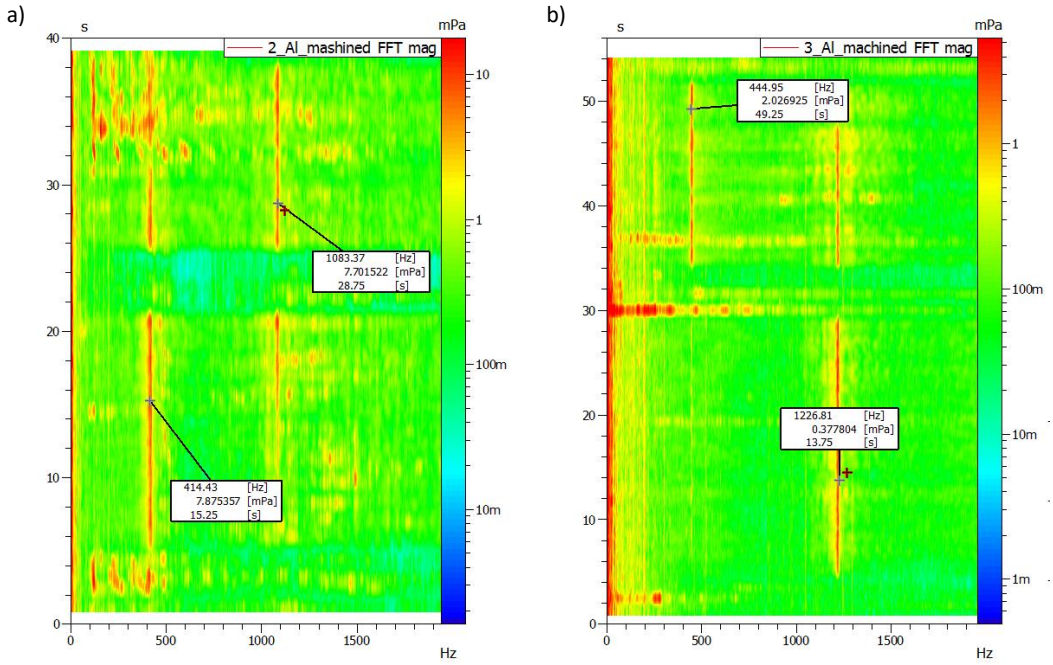

Figure 4.14. Excitation frequencies for the two electroformed copper samples (a) DC plating with brightener (b) pulse plating.

Table 4.3. Measured resonant frequency and calculated Young's modulus.

Sample	Resonant frequency (Hz)	E (GPa)
DC electroformed	414	122 ± 7
Pulse electroformed	444	129 ± 7

The elastic modulus was calculated with the known geometry, mass and resonant frequencies [95] by applying Equation 3.5. The obtained results are summarized in Table 4.3. The Young's modulus calculated for the DC in the presence of Gleam-PC brigthener and pulse electroforming are

122 and 129 GPa respectively, which is close to the measured values for copper OFE and OFS (Table 4.1, 115 GPa).

4.1.4 Intermediate conclusions

The robustness of the copper assembly was validated by tensile and compression tests combined with leak testing. The electroforming process allowed a good joining between the copper tube and stainless steel flanges. The bonding between the stainless steel flanges and the copper is stronger than the bulk copper itself. The assembly is leak-tight until final rupture. Furthermore, the effect of repeated bake-out cycles on the chamber was evaluated. The loss in performance is comparable to annealed copper OFE reference values and the stainless steel joint does not loose its strength.

Hence, the chamber most fragile point, where the rupture occurs, is where the copper wall is the thinnest. Thus, achieving a homogeneous thickness distribution along the length of the chamber is of major importance.

Electroformed copper mechanical properties were evaluated and compared to those of copper OFE and OFS. The differences between the two plating procedures on copper sulphate solution (DC plating in the presence of Gleam-PC brightener and pulsed plating on a bath without additives) were analyzed. The presence of a brightener on the electroforming bath helped to achieve a smaller grain size (1µm) and higher ultimate tensile strength and hardness than in the cold-rolled copper OFE and OFS samples. The pulsed plated copper exhibited a columnar growth with a larger grain size (15 µm width and 30 - 100 µm length), and ultimate tensile strength and hardness values comparable to those of annealed copper.

Measurements of Young's modulus from tensile testing tend to be less accurate due to the problem of reliably determining elastic strains and shows a high scattering of the results. The Young's modulus was investigated with the impulse excitation method. The results show a Elastic modulus similar to the one of copper OFE for the two electroformed copper procedures.

Both electroformed copper layers could withstand the chamber mechanical requirements expected for installation in an accelerator. A big point to take into consideration is the thickness distribution along the chamber. The DC electroformed process, since it has a brightener and a leveler, gives 80% of the nominal plated thickness in the critical area, which is located at the junction of the flange, while the pulse plated gives merely 40% (see Figure 2.9). This can be critical at the moment of selecting a process, as for some very small nominal thicknesses, the pulse electroforming process may not provide a sufficient thickness in this area.

4.2 Characterization of TiZrV coating

As seen in Chapter 1.5, several studies found a relation between the TiZrV coating composition and morphological properties, and the activation of the coating and pumping performance [22–24]. Hence, a detailed characterization of the TiZrV film on electroplated copper after mandrel removal was performed in order to have insights on the pumping performance. Data was gathered on film composition, thickness distribution, topography, adherence and crystallinity.

4.2.1 Coating composition and thickness distribution

X-Ray Fluorescence spectroscopy was used in order to assess the thickness and the bulk composition of the TiZrV thin film coating. During coating, the planar sputtering source provides a uniform thickness distribution along 200 mm due to the target size. In Figure 4.15, the thickness distribution of the coating is presented. Without any translational movement of the mandrel (black line), the maximum uniform thickness length (less than 20% variation) is about 200 mm.

An additional translational movement of the mandrel allows larger coating dimensions. The thickness distribution when the translational movement and coating is applied in two steps (position A and B) is shown in Figure 4.15 (green line). The optimization of the two positions of the mandrel towards the cathode allowed us to coat up to 400 mm length chambers with less than 20% thickness difference.

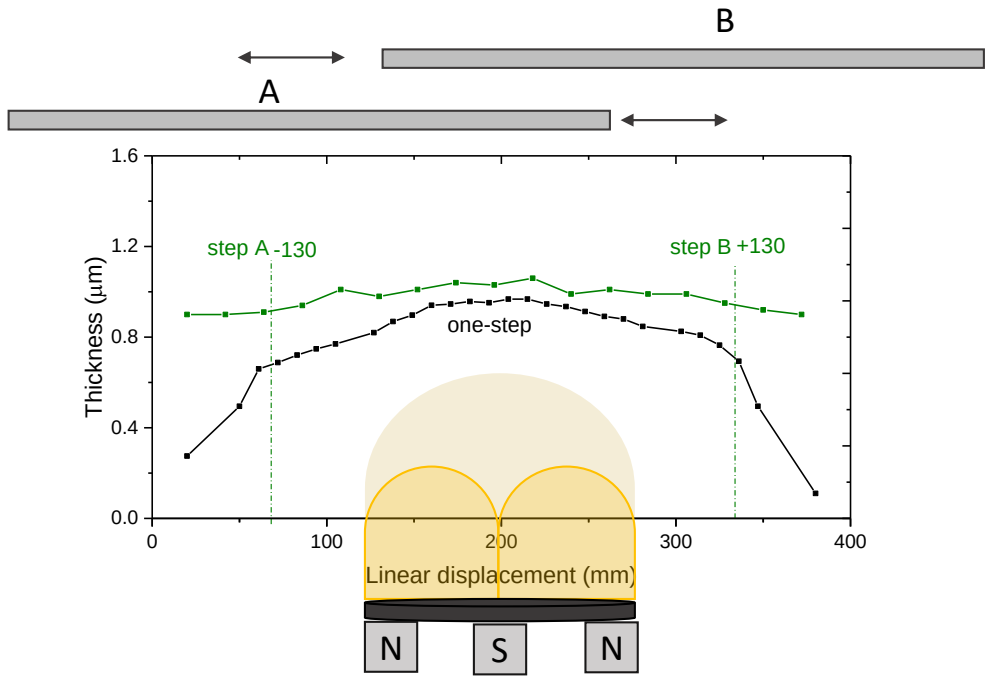

Figure 4.15. TiZrV coating thickness distribution along the length of the mandrel for one step coating (A=B=center of the cathode, in black) and two steps (A= -130, B= +130 mm from the center of the cathode, in green). A and B are the relative positions of the mandrel to the target.

TiZrV composition (at. %) and thickness were measured for different mandrels after coating. A 12 mm diameter mandrel is shown as example in Figure 4.16. The composition is uniform (37.7 at.% Ti, 26 at.% Zr, 36.3 at.% V in average) within the length of the tube and is within the good composition range for fast activation referenced by Prodromides [22, 24] in Chapter 1.5.

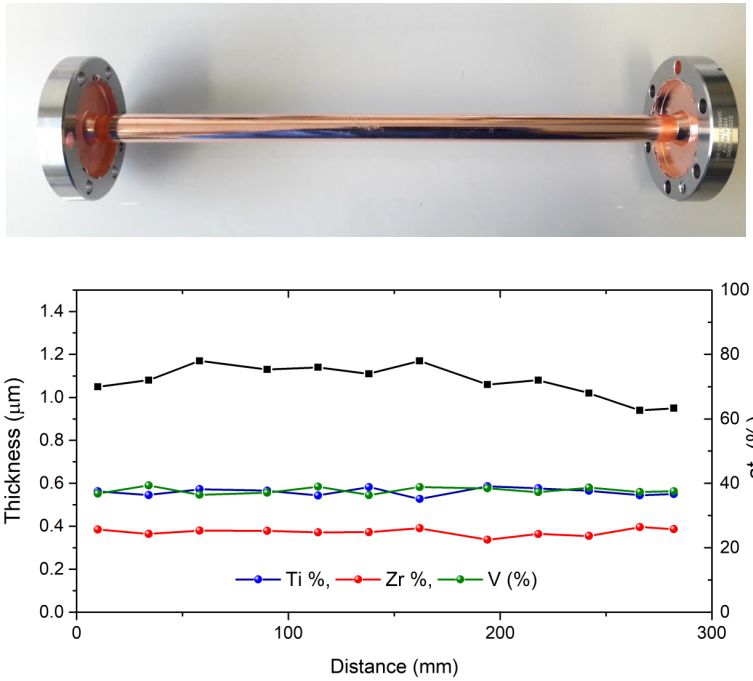

Figure 4.16. TiZrV coating thickness profile and TiZrV composition (at.%) for the 12 mm internal diameter, 300 mm length, chamber.

There was no difference in TiZrV composition by reducing the diameter from 16 mm to 3 mm as seen in Figure 4.17. The thickness is very homogeneous along the length of the chamber with a variation of less than 15%. It is also noticed, that the thickness of the coating increased for the same coating time (4 hours + 4 hours) and power (309 W) when reducing the diameter from 6 to 3 mm of the mandrel.

Assuming a flow of atoms arriving to the surface just from one direction, the resulting coverage on the rotating mandrel would be independent of its radius. If we consider in addition that the cathode has a finite extent, there is a possible range of impact angles to the surface and not only one single direction. A larger radius of the mandrel is reducing the range of impact angles and this results in a lower coverage for a larger mandrel compared to a smaller one. In the pressure conditions used for the experiment, the mean free path of atoms is large compared to the cathode to mandrel distance, thus the majority of the coating is deposited on the surface facing the sputtering target. However, some atoms scattered from the process gas contribute as well to the total thickness and can impact on any part of the surface of the tube. The coating thickness was always kept between 0.5 and 1.5 µm.

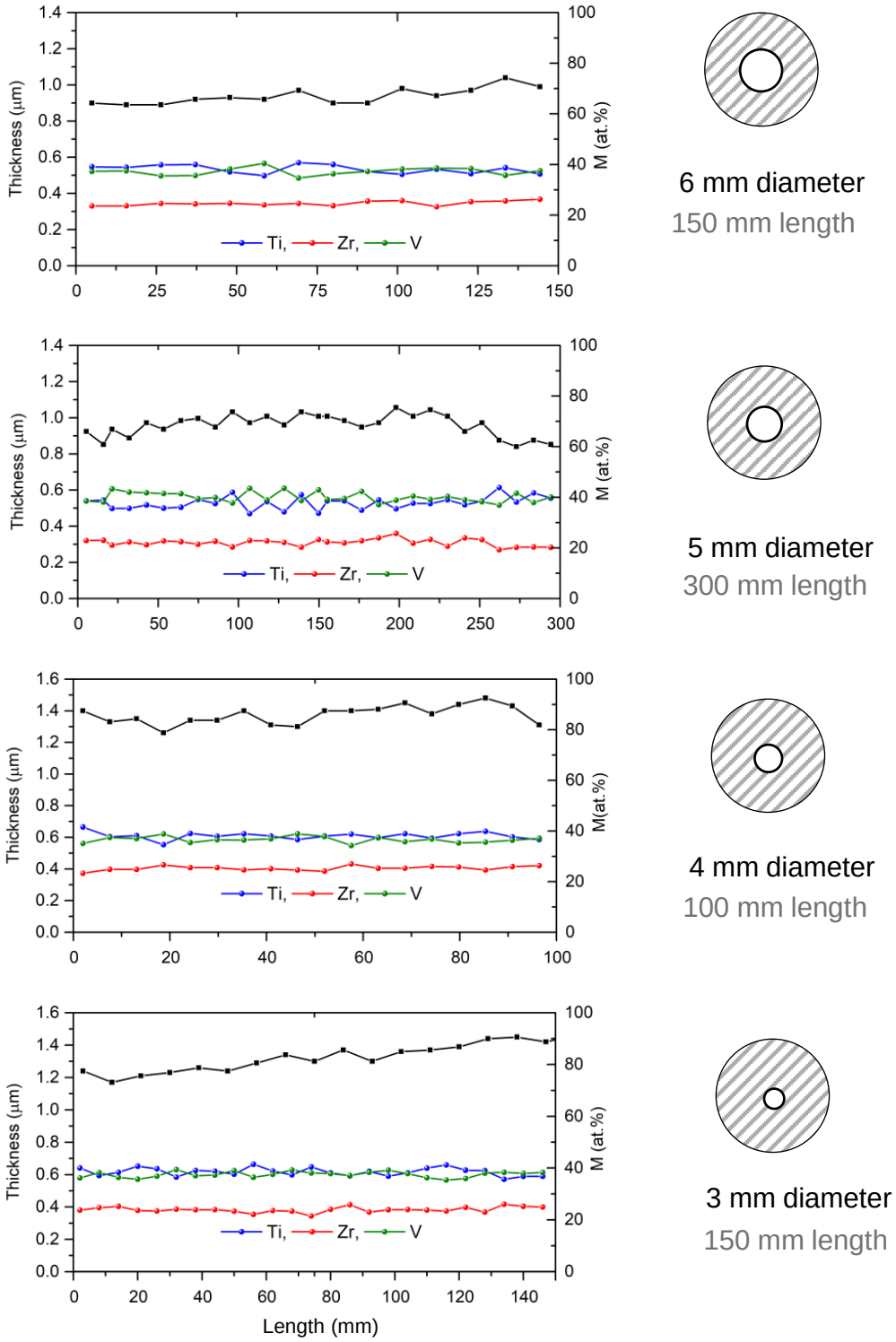

Figure 4.17. TiZrV coating thickness profile and TiZrV composition (at.%) for the 6 mm down to 3 mm internal diameter chambers. The length of each chamber is also given.

4.2.2 Microscopy observation

Coating imaging was carried out using Secondary Electron Microscopy (SEM) and Focused Ion beam (FIB). The methods are described in sections 3.1.2 and 3.1.3, respectively. The images shown hereafter concerns the NEG film surface that was in contact with the mandrel or the copper protective coating.

After mandrel removal, samples were cut from the electroformed chambers and analyzed. In figure 4.18 is shown the NEG surface from the samples from the Cu/NEG/mandrel sequence. Impurity-free surfaces are observed after the aluminium mandrel etching and acidic rinsing steps. The images show that the NEG coating replicates the aluminium mandrel surface features and roughness.

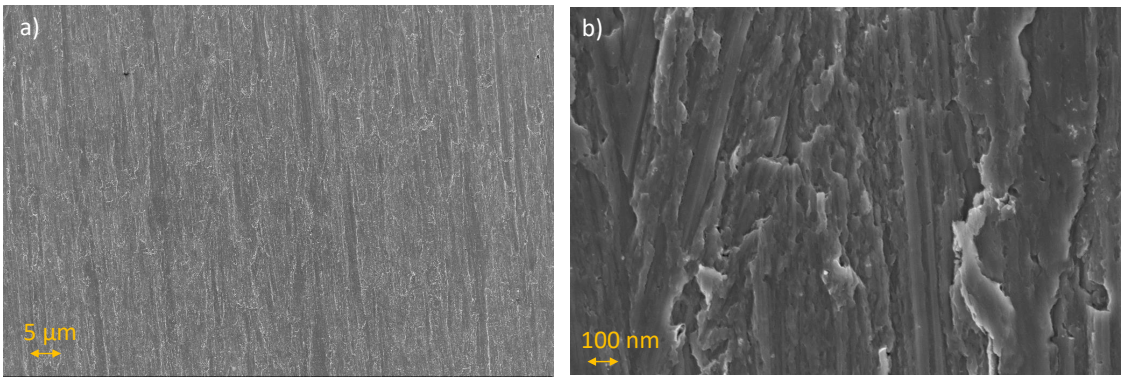

Figure 4.18. SEM pictures of TiZrV thin films prepared with the Cu/NEG/mandrel scheme after aluminum etching with NaOH 5 M and acidic rinsing at (a) lower magnification (b) higher magnification.

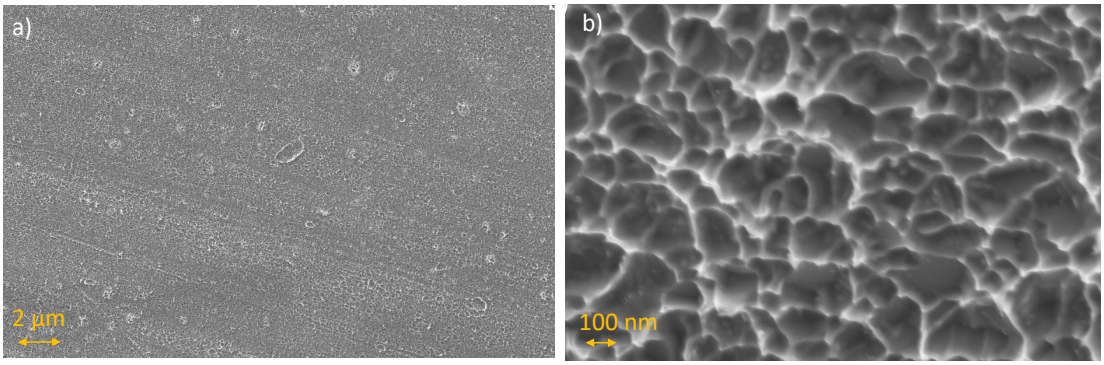

Figure 4.19. SEM pictures of TiZrV thin films prepared with the Cu/NEG/Cu/mandrel scheme after aluminium etching with NaOH 5M and copper interlayer etching with ammonium persulfate at (a) lower magnification (b) higher magnification.

In the case of using sputtered copper as a protective layer on top of the aluminium (Cu/NEG/Cu/ mandrel sequence), the NEG layer topography, after aluminium and copper removal, presents both the aluminium extruded features and the micro roughness derived from the sputtered copper (see Figure 4.19). The origin of the micro-roughness is explained by copper islands which are formed due to the poor wetting of the aluminium substrate. The pattern of the roughness follows an "inverted-dome" shape.

In addition, FIB milling combined with SEM was performed in order to evaluate the coating thickness and adherence to the substrate. The process includes the deposition of a small platinum layer on top of the coating, in order to minimize milling artefacts. The corresponding multilayer diagram is presented in Figure 4.20. Two interfaces were of particular interest: the coating adhesion of TiZrV to the copper sputtered layer and the presence of voids or anomalies between the copper PVD layer and the copper electroformed layer.

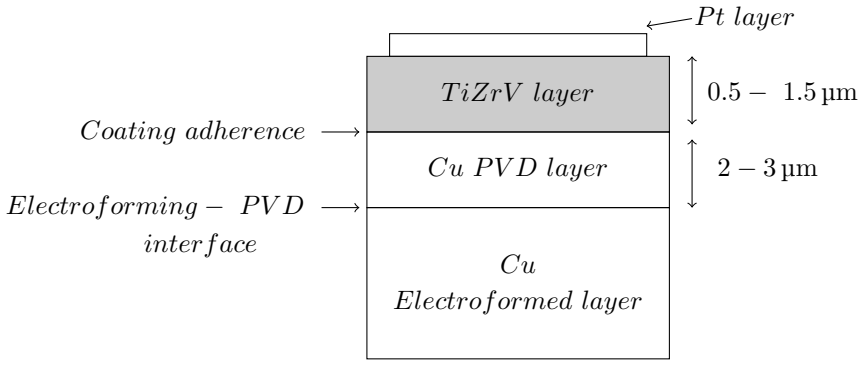

Figure 4.20. Schematic of coating layers analyzed with FIB combined with SEM.

FIB combined with SEM pictures are shown in Figure 4.21. For all the cases, the TiZrV coating is very compact and do not show a particular micro-structure, which can be related to a very small grain morphology. On the contrary, the grain morphology of the sputtered PVD copper and electroformed copper is revealed.

In the case of coating directly on aluminium mandrel (Fig. 4.21a and Fig. 4.21b, Cu/NEG/Al process), the images reveal a good TiZrV adherence to the substrate, which in this case in the copper sputtered layer. The thickness of the coating does not affect its uniformity. In addition, there is no visible transition line in the interface between the sputtered and electroformed copper which suggests that any possible contamination due to handling after PVD was removed during the surface preparation steps preceding the electroplated copper layer.

For the alternative Cu/NEG/Cu/mandrel case, where a protective copper sputtered layer is used on top of the aluminium mandrel, the FIB images are shown in Fig. 4.21c and Fig. 4.21d. Some voids are observed on the interface between the thin TiZrV coating and the PVD copper, which are not observed in the case of thicker coatings. One of the risks of chemical etching the copper protective layer is to etch in addition the copper substrate underneath. The voids could be caused by the bath, which has penetrated the thin film as it is not thick enough to act as a barrier.

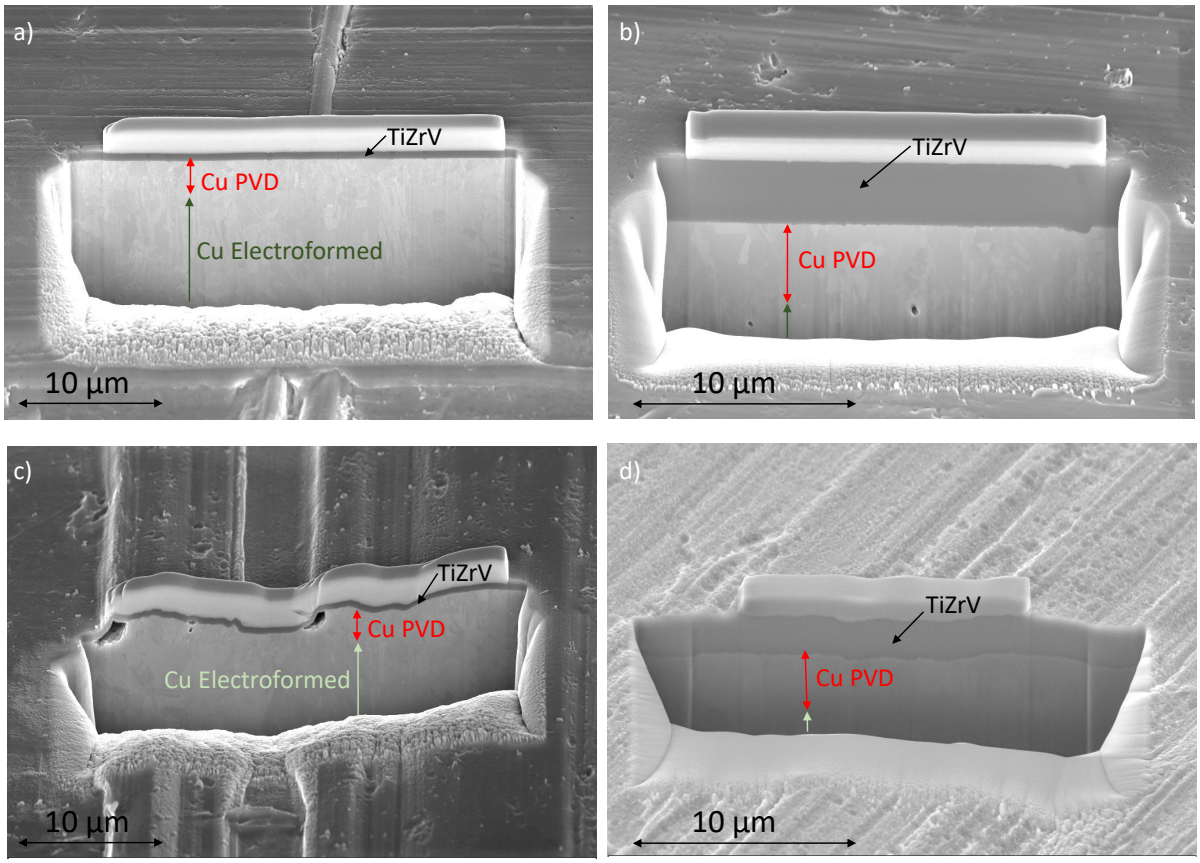

Figure 4.21. FIB combined with SEM pictures of TiZrV thin films on copper electroplated substrate after aluminum etching with NaOH 5 M. In (a) 0.5 µm TiZrV film and in (b) 1.5 µm TiZrV film. FIB pictures of TiZrV thin films on copper electroplated substrate after interlayer copper etching with ammonium persulfate. In (c) 0.5 µm TiZrV film and in (d) 1.5 µm TiZrV film.

In addition to the FIB analysis, NEG coating adhesion after mandrel removal was measured on coatings according to ASTM D3359-B with adhesive tape on a cross-hatched surface. Results showed a 5B classification (no traces of delamination) for both type of coating sequences.

4.2.3 Film crystallinity

The coating morphology and crystalline structure of the TiZrV films after the mandrel etching were studied by X-ray diffraction analysis. The characterization of thin films using the conventional symmetrical Bragg Brentano configuration (θ -2θ) generally produces weak signals from the thin film and intense signal from the substrate. To avoid the latter, a grazing angle is used during the measurement. XRD measurements were carried out using an incidence angle of 5° and Cu Kα radiation (step size was 0.02° and 3 s per step).

In Figure 4.22 the diffractograms of the TiZrV coatings after mandrel removal are shown. An example of the Cu/NEG/mandrel sequence (red line) and a Cu/NEG/Cu/mandrel sequence (blue line) are compared to a standard TiZrV coating on copper OFE (black line). The results show a broad diffraction peak at about 38° which corresponds to a nanocrystalline structure for all the coatings tested. The grain size, according to the Scherrer equation [102] (eq. 1.1), is about 3 nm in all the studied cases. This was expected from Figure 1.5 as the composition range is always kept in the region of the diagram which was found to correspond to nanocrystalline coatings.

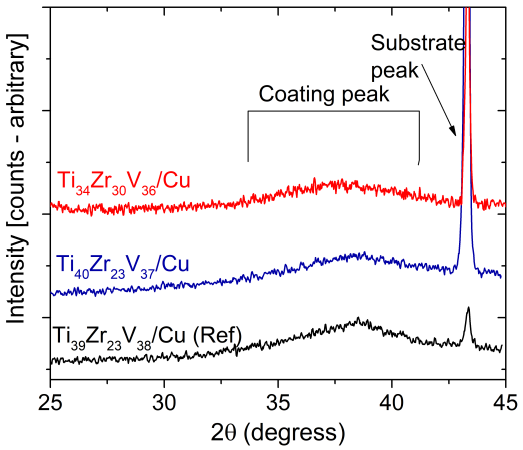

Figure 4.22. X-ray diffractograms for TiZrV films on copper: in black a reference NEG coating, in red Cu/NEG/mandrel sequence and in blue Cu/NEG/Cu/mandrel sequence.

4.2.4 Intermediate conclusions

The TiZrV films after mandrel removal show an almost constant composition along the length of the chamber (atomic composition around 30-39% Ti, 21-30% Zr, 30-39% V) and a nanocrystalline structure (grain size <3 nm). In addition, the coatings are adherent and they reproduce the mandrel surface topography. This means that the coating can be very smooth if a very smooth mandrel is used in the process.

The measured properties of the film produced in this study are in accordance with the properties

reported for standard TiZrV coatings [24], which activate and exhibit the maximum pumping speed at low temperatures (180 - 230 °C) as it was seen in Section 1.5.

4.3 Pumping properties of processed chambers

The mechanical robustness and NEG coating characterization studies have confirmed the feasibility of construction of such an assembly. The last important point to validate is the pumping performance of the NEG coating. In this section, the H_2 sticking factor and the CO capacity of the TiZrV coating are measured. In addition, the activation temperature (Ta) which enables the best pumping properties of the getter film is going to be evaluated and compared with NEG coatings performed with the conventional process (see section 2.3).

To evaluate the sticking coefficient and the surface capacity of the coated prototypes, it is necessary to use a specific method and set-up (as seen in Figure 4.23, called transmission method). Each chamber is installed on a vacuum system equipped with gas injection of H_2 and CO, two Bayard-Alpert gauges (P_1 and P_2) mounted on both extremeties of the sample and a pumping group composed by a turbo molecular pump (TMP) and a primary pump. The measurement records the pressure ratio of a gas after injection on an activated NEG coated surface following equation 4.2.

$$Pressure\,ratio = \frac{P_1}{P_2} \tag{4.2}$$

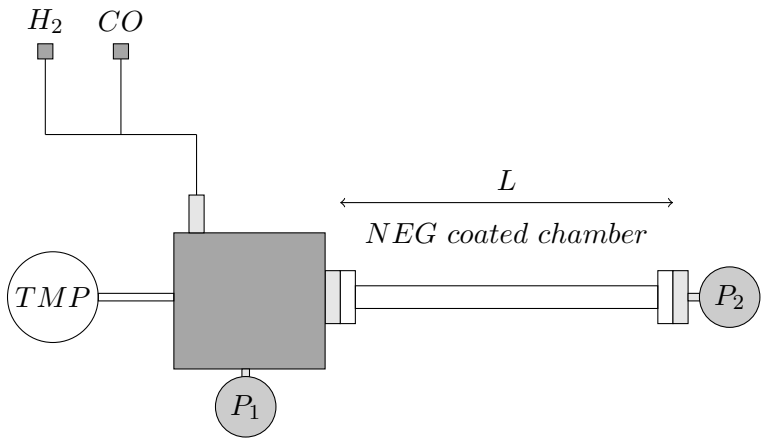

Figure 4.23. Transmission measurement set-up of a getter coated chamber. The system is provided by two Bayard-Alpert gauges (P_1 and P_2), and a pumping group composed by a turbo molecular pump (TMP) and a primary pump.

The measurement procedure is described in detail hereafter. The system is pumped down to less than 1×10^{-8} mbar and a leak detection is carried out (the acceptance threshold is 1×10^{-10} mbar l s^{-1}). Then the system is baked out at 250°C for 24 hours while the NEG chamber is kept at 80 °C in order to remove the water from the system while keeping the NEG coating

not-activated and avoid pumping the gas released during the bake-out. During bake-out, the total pressure of the system is monitored by a standard Penning ionization gauge. Afterwards, the system is kept at 150°C while the NEG chamber is activated at the desired temperature. At this point, the gauges are outgassed and after 24 hours the system is left cool down to room temperature. The pressure difference between the inlet and outlet of the chamber is then measured for different injection rates. A post-treatment of the transmission results with simulations finally allows the determination of the sticking factor of the coating for a given gas.

4.3.1 Simulation of the vacuum system using Molflow +

A simulation of the transmission measurement is necessary to translate the experimental results into the characteristic sticking NEG values [103]. Molflow + is a Montecarlo simulator intended to calculate pressure profiles and conductances in ultra-high vacuum [31, 104]. This method performs vacuum simulations using molecules that are traced until they are pumped away. It does not include collisions between molecules as the mean free path of the molecules in the accelerators pressure ranges is above the characteristic size of the vacuum chambers. In this case, steady state simulation are required, where a defined conductance, sticking factors and geometries are entered as input parameters. Pressure and particle density are given as a result of the calculations [105].

The steady-state mode fixes the outgassing rate to a constant value and gas could come due to thermal desorption from the chamber walls or from injection points. Some assumptions enable to simplify the calculations: the gravitation is assumed negligible and molecular trajectories are assumed to be rectilinear. Then, a large number of typical particle trajectories is estimated and the probabilities of different events are considered. The distribution of the emission of particles from the walls is simulated as a cosine law and for each individual collision, the probability of a particle to be absorbed by the wall is called sticking factor. A randon number is calculated upon collision with the wall, and is compared to an assigned value for sticking. Then if the value overcomes the latter the particle will be reflected from the wall, and otherwise, the particle will be considered to be pumped and the calculation of trajectory is terminated.

Our system composed of two ionization gauges, one pumping port, one injection line and one NEG coated chamber of 300 mm length and 12 mm diameter (aspect ratio 50) is drawn in CAD and imported to Molflow + (see Figures 4.24 and 4.25). The simulation counts the number of particle hits in each wall of the chamber, which is interpreted in the software as a facet. Different properties can be assigned to the facets. In our simulation, the injection site will be implemented as a facet with desorption and the pumping will correspond to the sticking probability of a facet. Afterwards, the simulation is run (see Figure 4.26), assuming different sticking factors on the chamber facets. Thus, the relation between pressure ratio and sticking factor is determined for the given geometry.

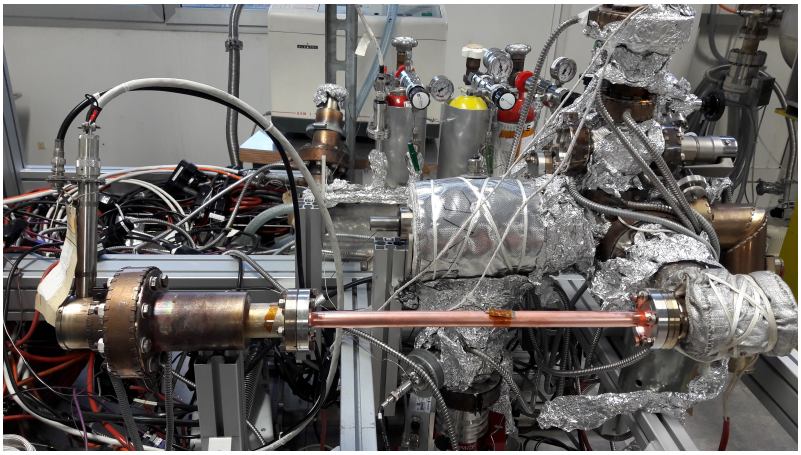

Figure 4.24. Chamber installed in transmission system.

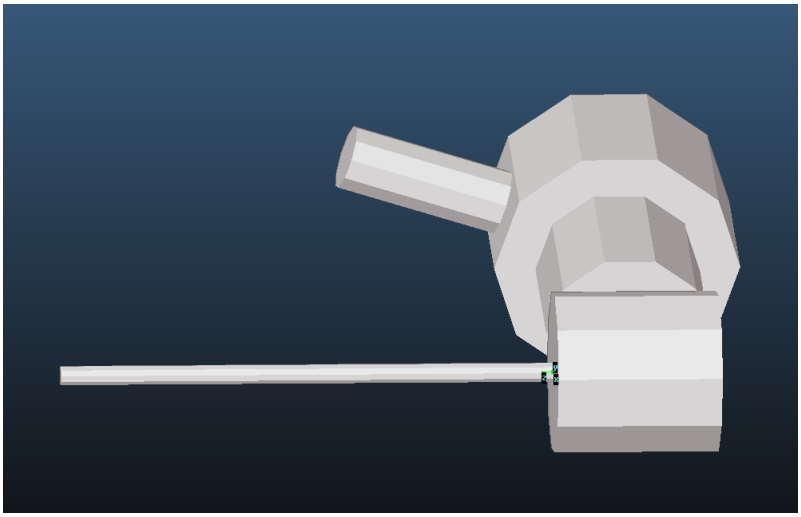

Figure 4.25. CAD of transmission system imported in Molflow +.

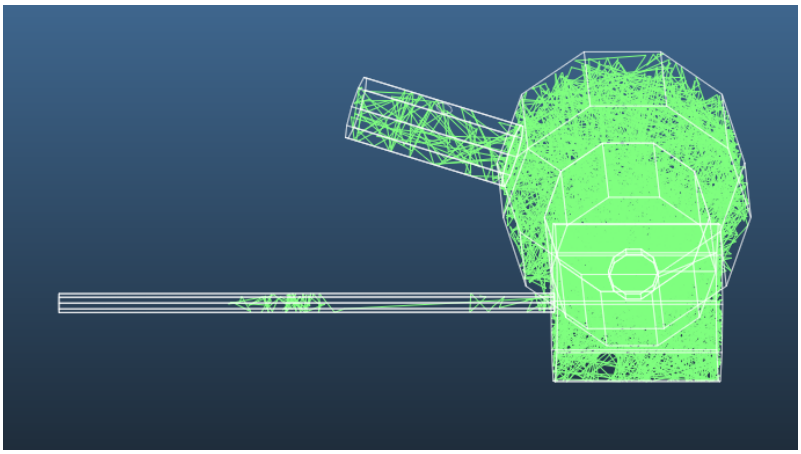

Figure 4.26. Measurement in Molflow +.

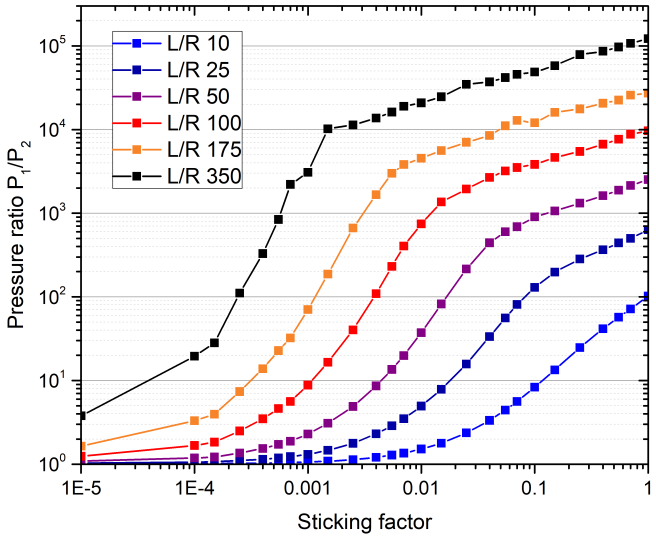

Figure 4.27. Sticking factor versus the pressure ratio (P_1/P_2), simulated in Molflow + for all aspect ratios (Length/Radius).

Results from the transmission model obtained by simulation in Molflow + are shown in Figure 4.27 for different chamber geometries. The relation between sticking factor and pressure ratio can be evaluated by using this relationship. It is important to select an appropriate aspect ratio (length/radius) for the measurements, as is seen in Figure 4.27. If the aspect ratio is too low (i.e. 10) the pressure ratio for the H_2 sticking measurement will vary between 1-2 (as its sticking coefficient is on the 10^{-3} - 10^{-2} range) and the measurement would not be accurate. On the contrary, if the aspect ratio is too high (i.e. 350) the pressure ratio will take values on the range of 10^4 to 10^5. Hence, it will be necessary to inject 10^6 times the base pressure, with pressures above the molecular gas regime and that could in addition damage the TMP. Furthermore, the pressure ratio for H_2 and CO measurement sits in the plateau of the curve, meaning that pressure lecture errors could modify strongly the results. For this reason, the aspect ratio was fixed to 50 for the measurements in order to have a good sensitivity to H_2 sticking factor measurements.

4.3.2 Hydrogen pumping performance

Several chambers with aspect ratio (L/R=50) were installed in the transmission system (see Figure 4.24) and H_2 sticking was evaluated after 24 hours heating at increasing temperature steps from 180°C to 280°C. The H_2 pumping measurement is the most critical evaluation of the coating performance, as H_2 is very sensitive to impurities in the bulk or surface of the coating. The different parameters used in the chamber elaboration process are going to be evaluated with respect to the hydrogen sticking factor: the electroforming procedure used, the coating layer arrangement and the nature of the aluminium mandrel (alloy or thickness).

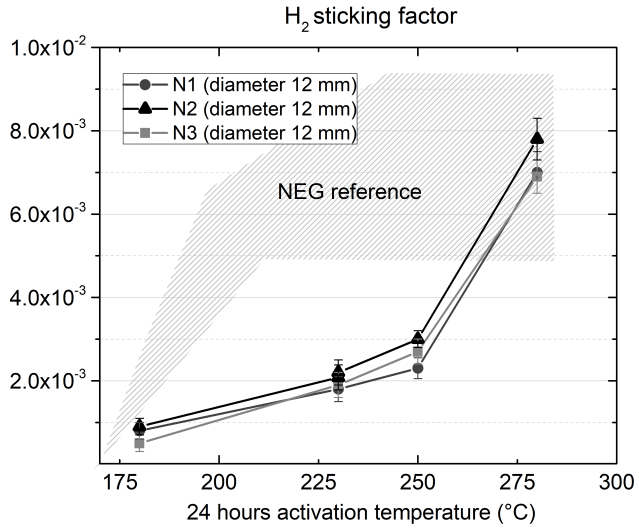

Figure 4.28. H_2 sticking factor versus 24 hours of activation temperature for a 12 mm diameter, 300 mm length, NEG coated chamber (aluminium AW-1050, 0.5mm thickness) following the Cu/NEG/mandrel sequence with DC electroforming plating. Three chambers (N1, N2 and N3) are measured. NEG reference values are represented in a darker area.

The reproducibility of the results was assessed on several 12 mm diameter chambers which followed the coating procedure (Cu/NEG/mandrel), on a mandrel of AW-1050 alloy and 0.5 mm thickness, and were plated using DC current in the bath that contains a brightener (process described in Chapter 2). The results are plotted in Figure 4.28. The first observation of the results is a great reproducibility between the different chambers. Compared with NEG reference values (Table 1.1 and darker area in Figure 4.28), the chambers exhibit a delay in activation temperature, with the maximum sticking found at 280 °C, which differs from reference values of TiZrV coatings where the maximum sticking is achieved between 200 - 230 °C [13].

The effect of different process parameters was also evaluated. Especially those concerning the coating and electroforming steps (Figure 4.29).

The effect of the electroforming method on the pumping performance was evaluated for the same mandrel of 12 mm diameter (AW-1050, 0.5mm thickness). The results are shown in Fig. 4.29a. The difference between the two electroforming procedures is not evident from the results. The best sticking factor was obtained with the pulsed electroforming after 280 °C activation. Nevertheless, this minor difference does not justify the use of pulse plating instead of DC plating with Gleam-PC additive. The latter was found to provide a better thickness distribution on the critical section close to the stainless steel flange and in addition, better mechanical performance at room temperature.

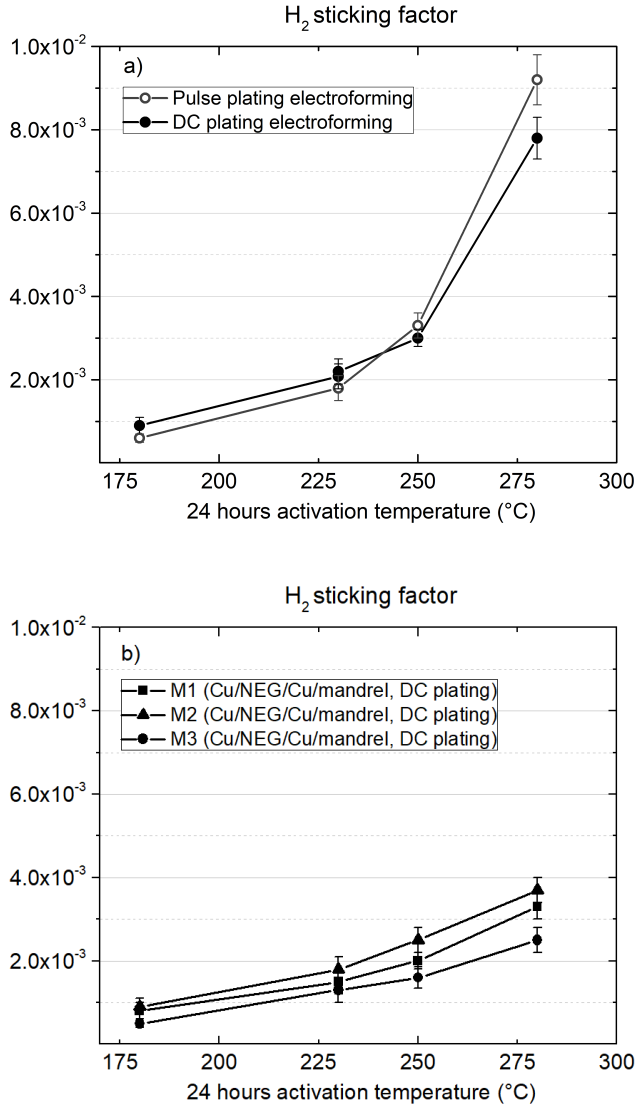

Figure 4.29. H_2 sticking factor versus 24 hours of activation temperature for a 12 mm diameter, 300 mm length, NEG coated chamber; In (a) for the two different electroforming processes DC electroforming or PC electroforming with the Cu/NEG/mandrel sequence; In (b) For the situation where a copper layer is sandwiched between the NEG and the mandrel (Cu/NEG/Cu/mandrel sequence) using DC electroforming. Three chambers (M1, M2 and M3) are measured.

Furthermore, the effect of adding a sandwiched copper layer between the aluminium mandrel and the NEG coated surface is also evaluated (Cu/NEG/Cu/mandrel sequence). The results are shown in Fig. 4.29b. It is interesting to observe that lower values of sticking factor are obtained using this coating sequence. At the beginning of the study [41], this technique showed promising results due to absence of impurities on the TiZrV surface. Afterwards, it was discovered that impurity free deposits were also obtained for the Cu/NEG/mandrel sequence by rinsing with ammonium persulfate. When both are compared, at the same level of surface impurities, the conclusions of the sticking coefficient lead to a re-evaluation. The sequence without the copper

sandwiched layer showed more reproducible results, and a higher maximum sticking factor. The reason of a lower sticking in the latter could be related to two factors. On one hand, the micro-roughness generated ("inverted-dome" shape, Figure 4.19) could hinder the oxygen diffusion across the bulk. On the other hand, FIB images revealed the occasional appearance of voids due to the copper protective layer etching procedure (Figure 4.21c). These voids could accumulate residues of etching solution that could provoke outgassing during the activation of the NEG and therefore, lower its performance.

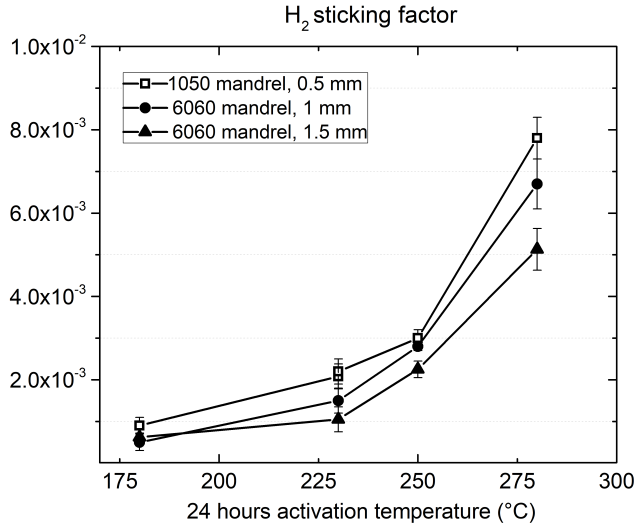

Figure 4.30. H_2 sticking factor after 24 hours of activation vs. activation temperature for three different mandrels (alloy and thickness) following the Cu/NEG/mandrel sequence and DC electroforming.

The consistency of the method for different aluminium mandrels (aluminium alloy and thickness) was tested. The effect of the mandrel aluminium alloy and thickness was studied in mandrels which were mainly made by extrusion. Two different aluminium alloys were studied (1050 and 6060 AW-series) and the different thickness tested ranged from 0.5mm to 1.5mm. The results are shown in Figure 4.30. The delay in activation temperature with respect to the standard NEG is observed in all the situations, but it is possible to notice a faster activation in the case of decreasing the thickness of the alloy. A more detailed evaluation of the effect of the mandrel characteristics (alloy and thickness) on the reverse coating process will take place in chapter 5.

4.3.3 CO saturation measurements

In addition to H_2, CO is pumped on the surface of the getter. The mechanism of pumping is explained as a chemisorption to the surface up to the formation of one monolayer. The evaluation of the maximum saturation helps to understand the state of the getter surface (surface activation or roughness). This was already documented in sections 1.5 and 1.6.

The CO measurement is always performed after H_2 injection because H_2 diffuses inside the bulk and leaves available the surface adsorption sites. On the contrary after CO injection, the sticking factor measured for H_2 is reduced, as the surface is already blocked with CO to the detriment of H_2 pumping [24]. The standard CO saturation measurement is done in a Fisher-Mommsen system [106] provided with a calibrated conductance, which is used to calculate the pumping speed at the aperture. When the transmission method is used, the CO pumping speed at the aperture is calculated with the sticking factor for every interval of time. The comparison between the two measurements is detailed in Appendix II.

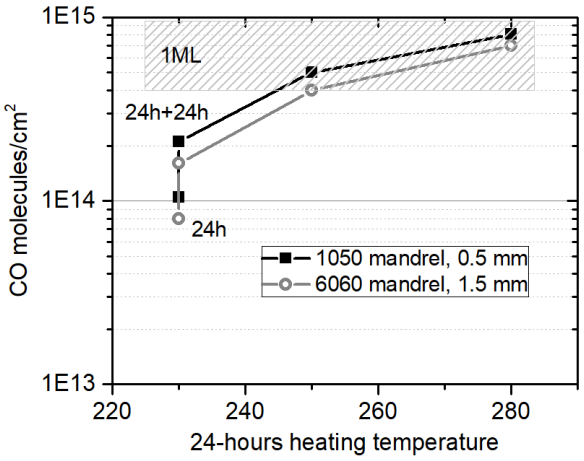

Figure 4.31. Maximum number of CO molecules absorbed per cm^2 versus 24 hours of activation temperature for NEG coated chamber produced with two different mandrels (alloy and thickness) following the Cu/NEG/mandrel sequence and DC electroforming. The heating steps are made for 24 hours, unless otherwise indicated. One monolayer (ML) corresponds to 5×10^{14} - 1×10^{15} CO molecules/cm^2 [10].

The maximum number of CO molecules absorbed per cm^2 after in-situ 24 hours activation for NEG coated chambers produced with two different mandrels (alloy and thickness) following the Cu/NEG/mandrel sequence and DC electroforming process is displayed in Figure 4.31. The results show a completely activated surface (capacity of 5×10^{14} molec cm^{-2}) when the chamber is heated for 24 hours at 250 °C. For the thin mandrel, the capacity at 230 °C is around 1×10^{14} to 2×10^{14} molec cm^{-2} if heated for 24 or 48 hours respectively. The 0.5mm thick mandrel showed a slightly faster activation at lower temperatures than the 6060 1.5mm mandrel, which is in agreement with the trend of observed H_2 sticking values in Figure 4.30. Even-though the surface is completely activated at 250 °C, the H_2 sticking coefficient is still lower than standard NEG values 5×10^{-3} to 1×10^{-2} [29]. This suggests that the presence of a completely activated surface is not the only requirement for a full H_2 pumping performance. As described in section 1.6, H_2 is affected by bulk impurities, and the presence of a slightly contaminated bulk would lead to higher temperatures or activation times in order to dilute the impurities.

4.4 Conclusions

The electroformed vacuum chambers were successfully assembled and the overall process was validated in terms of mechanical performance, leak-tightness and pumping performance. The aluminium mandrel is very easy to procure and to machine. It is compatible with PVD systems, is stiff during all the steps of the process and is very easy to remove by chemical etching. The lowest diameter produced was 3 mm, which is the lowest at present NEG coated diameter produced, as no other method exists to integrate the NEG coating in such a geometry.

The chambers were leak tight and showed good mechanical resistance. A good joining between the copper tube and the stainless steel flanges was achieved by electroforming. Electroformed copper mechanical parameters were compared to those of copper OFE and OFS. There are two different electroforming processes on copper sulphate solution that were studied: DC plating in the presence of a brightener and pulse plating on a bath without additives. The particular micro-structure governs the mechanical response of each plating procedure. Very small grains are produced when DC plating with brightener is applied. This helps to achieve a higher ultimate tensile strength and hardness than cold-rolled copper OFE. On the other hand, big grains and columnar growth is observed in the pulse plated copper. This translates into lower ultimate tensile strength and hardness values which are comparable to annealed copper.

The elemental composition, the morphology and crystallinity of the produced TiZrV films were discussed. The TiZrV coating exhibits a constant thickness distribution along the length of the chamber and an homogeneous TiZrV composition. SEM pictures reveal TiZrV films free of surface impurities, and reproducing the mandrel topography. The FIB milling analysis shows a good coating adhesion and confirms a clean interface between the PVD and electroformed copper. Although in some situations, it puts into evidence the presence of voids when a copper sandwiched layer is used between the aluminium mandrel and the TiZrV coating. In addition, XRD analysis reveals a nanocrystalline structure for all TiZrV coatings tested, with a grain size lower than 3 nm.

The performance of the coatings was evaluated by H_2 and CO sticking factor measurements. Pumping speeds of the produced vacuum chambers were measured after 24 hours heating at increasing temperature steps from 180 °C to 280 °C. The chambers show a good H_2 and CO pumping performance with slightly delayed activation temperature if compared to reference NEG coating values. The chambers exhibit a H_2 sticking factor greater than 5×10^{-3} when activated at 280 °C ±10 °C for 24 hours. CO saturation values indicate a complete functional activated surface already after heating at 250 °C.

The pumping performance was almost independent of the applied copper electroforming procedure. Hence, the most suitable electroforming procedure tested at the present stage is the DC electroforming with the presence of brightener. It provides a better thickness distribution in

critical areas of the electroformed shape and a stronger mechanical resistance at room temperature.

The origin of the activation delay should be evaluated in detail. This delay could be explained by assuming a slightly contaminated TiZrV bulk, since hydrogen, after dissociation, diffuses into the bulk of NEG materials. Contaminants in the bulk could reduce H diffusivity and slow the pumping of hydrogen. These contaminants could be introduced either by the chemical etching to reveal the NEG surface or by diffusion from the electroformed copper. This will be evaluated in detail in the next chapter.

5 Evaluation of impurities related to the process

In the previous chapter, it became evident that the pumping performance of the inverse NEG coated chambers for low activation temperatures is below the expected performance of a TiZrV film. This can be explained if considering a TiZrV film slightly contaminated. Possible contamination sources are explained in detail in this chapter. The impurities could be introduced during the PVD coating of the mandrel, or during the copper electroforming and later diffused into the NEG layer or could be originated by the aluminum mandrel etching. Thermal desorption analysis was used to measure the impurities in the electroformed copper. XPS surface and bulk analysis helped to identify the impurities in the getter thin film.

5.1 Introduction

As seen in Chapter 4, the coated chambers exhibit a delay in activation temperature when compared to the reference NEG coatings reported values [29] (see Chapter 1.6). A decrease of pumping performance could be explained if we consider that the NEG thin film has been slightly contaminated during the manufacturing process or the activation step. Therefore, an identification and quantification of possible impurities in each step of the process is crucial in order to understand whether they could explain the delay.

The copper electroformed substrate could act as a source of impurities. The contaminants could leave the copper bulk and diffuse into the thin film during the activation procedure. On the other hand, the source of impurities could also be the thin film itself which is polluted in the step of coating or etching.

A first study was done by copper electroforming a vacuum chamber without the NEG getter thin film and applying the conventional TiZrV magnetron sputtering on the produced copper

substrate. The results showed that the pumping performance of the electroformed chambers after (230 °C, 24 hours) activation was unlike the one for the copper OFE reference chamber, which was coated at the same time in the same magnetron sputtering system. The NEG on OFE copper exhibited a H_2 sticking factor of 8×10^{-3} whereas the one for NEG on electroformed copper substrates was around 2-3 $\times 10^{-3}$. On the other hand, if the electroformed substrate was annealed at 350 °C for two hours before coating, the sticking factor was enhanced to 5×10^{-3}. The mentioned study brought the attention to the electroformed copper impurities. Nevertheless, each step of the process has been revised in this chapter.

In Figure 5.1, the most probable sources of contamination and type of impurities are presented. The impurities were classified in two main groups: gas and solid (metal). The diagram exhibits the complexity of the study. Each point also mentions the various methods which were applied for impurity detection. In this chapter, every step is going to be presented.

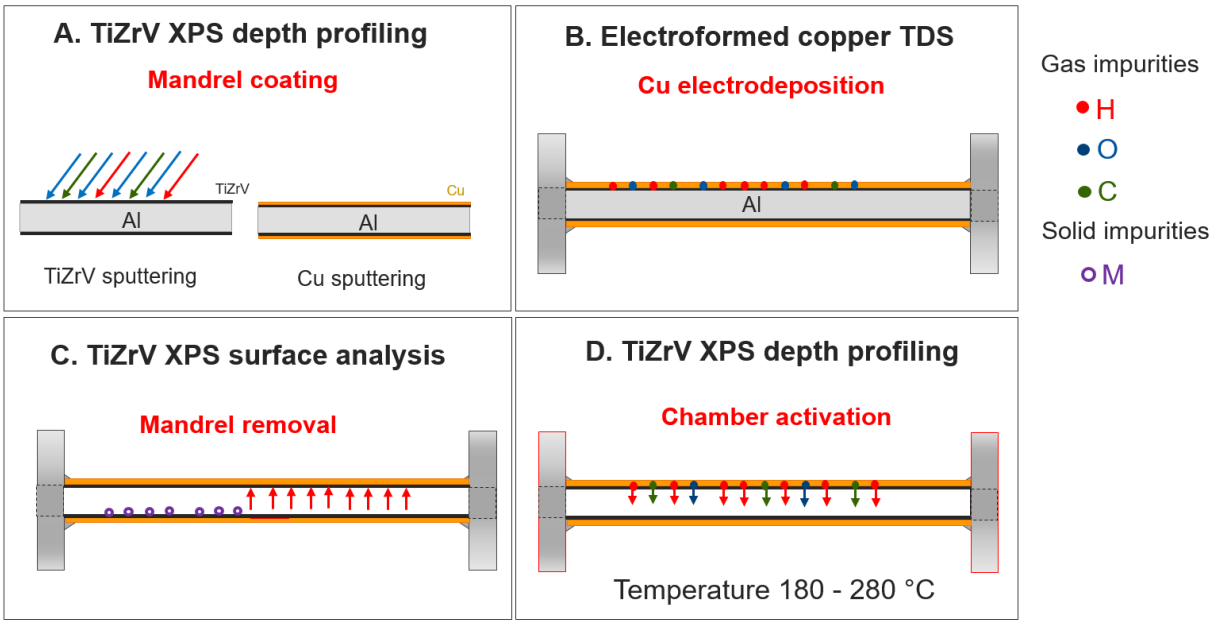

Figure 5.1. Diagram of the possible sources of impurities. Gas impurities (C, O and H) and solid impurities (M) are represented in each respective color. The different methods used for the characterization are highlighted for each step of the process (A: Coating of the mandrel, B: Electrofoming step, C: Mandrel etching, D: Chamber activation).

Samples for the NEG layer analysis were produced as flat platelets according to the reverse NEG process (Cu/NEG/Al) explained in Chapter 2. For the electroformed copper analysis, the samples were produced in DC and pulsed mode without the NEG thin layer in order to separate the NEG outgassing and pumping contributions from the electroformed copper one.

5.2 Specific methods for impurities detection

5.2.1 Thermal desorption spectroscopy

Thermal desorption spectroscopy (TDS) is a technique that allows us to measure the desorption of gases as a function of the heating temperature [107–110]. The TDS system used for the analysis is described in Appendix III. A residual gas analyser (RGA) is placed above the sample and measures the pressure of the different gases, which are outgassed, as a function of time and temperature. The mass spectrometer is calibrated for the different gases of interest. The absolute amounts are within a factor of 2 in accuracy. The relative errors are given by bars in the different plots.

All TDS measurements follow the same standard procedure. The samples (1cm x 1cm) are positioned in the sample holder and inserted in the measurement system. The measurement follows a $10\,^{\circ}\mathrm{C\,min^{-1}}$ heating ramp from room temperature to $700\,^{\circ}\mathrm{C}$ and the different gases are analyzed by the RGA. The peaks that are followed are:

- (m/z = 2) for hydrogen H_2
- (m/z = 14) for nitrogen N_2
- (m/z = 15) for methane CH_4
- (m/z = 18) for water H_2O
- (m/z = 28) for carbon monoxide CO and N_2
- (m/z = 32) for oxygen O_2
- (m/z = 40) for argon Ar
- (m/z = 44) for carbon dioxide CO_2

5.2.2 XPS surface analysis and activation monitoring

X-ray photoelectron spectroscopy was used in order to detect surface impurities on the TiZrV film. The spectra were acquired with the monochromatic excitation photon source of 1486.7 eV (Al Kα), with an energy resolution of 0.1 eV and a normal emission angle from the sample in an ultra-high vacuum (base pressure 2×10^{-10} mbar) system from SPECS Surface Nano Analysis GmbH (Berlin, Germany).

In addition, the getter samples are activated in the XPS system thanks to a heater mounted on the sample manipulator. Heating of the sample in the XPS set-up is achieved by radiation from a filament. During activation the NEGs surface oxide is progressively reduced. This is achieved

by heating to a temperature high enough to diffuse the oxygen from the surface oxide into the bulk of the getter. This process is performed through four stages and the sequence is called in the following standard cycle of activation:

- 1st room temperature (RT)
- 2nd heating to 160 °C for one hour
- 3rd heating to 200 °C for one hour
- 4th heating to 250 °C for one hour

After each heating stage a new spectrum is taken. These temperatures were selected because they correspond to different levels of NEG activation, which for the standard NEG occurs at 200 °C for 24 hours heating. Two samples were simultaneously heated and measured [28].

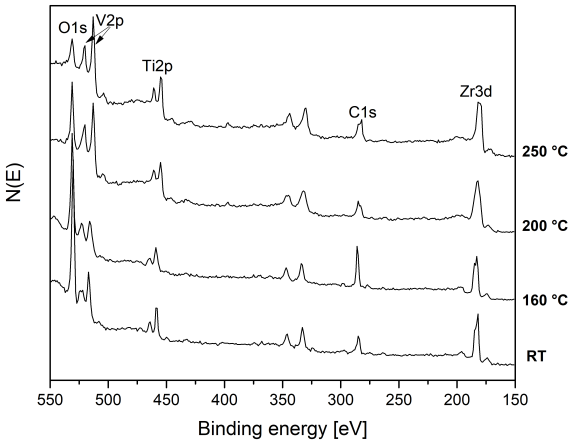

Figure 5.2. Survey XPS spectra of a $Ti_{32}Zr_{37}V_{30}$ (at %, EDX measured) film on copper substrate, as received (RT), and after heating for one hour at various temperatures. The measurement was performed at the end of the heating plateau.

Figure 5.2 shows a typical NEG spectrum sequence, going from room temperature to full activation. These are charts for standard NEG, and will be later used as reference for the reverse NEG samples. After the survey, the spectra of the interesting elements (usually O, C, Ti, Zr, V) which give specific information about the activation process are taken in detail. Fig. 5.3 schematizes in close-up the chemical shift of each element during the process [111]. As delivered, the metals lines show the characteristic peak (in red) of the oxidized state and after reaching 250 °C they shift to the metallic state (in blue). The activation performance is evaluated by the reduction of the area of the O1s peak during the heating cycle. For the evaluation of the oxygen reduction content, the equation 5.1 is used:

$$\Delta O_{1s}\ peak\ area\% = 100 \times \frac{O_{1s}(RT) - O_{1s}(250\,^{\circ}\mathrm{C})}{O_{1s}(RT)} \tag{5.1}$$

The activation is considered complete when the oxygen peak area reduction is greater than 67% at 250 °C after the standard cycle of activation [41]. Any reduction below this value is considered to represent a delayed activation.

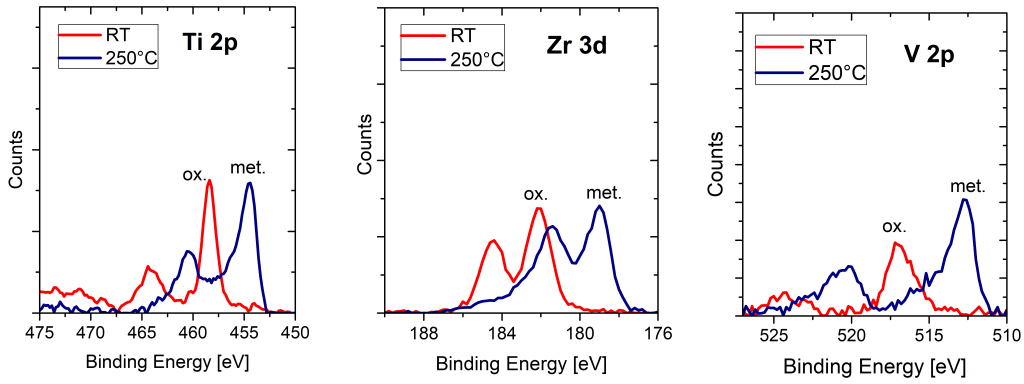

Figure 5.3. Ti2p, Zr3d and V2p multiplex spectra showing the chemical shift from the oxidized state (ox.) to the metallic state (met.) after the XPS activation cycle.

5.2.3 XPS bulk composition depth profile

The chemical composition of the TiZrV films was investigated at room temperature by X-ray photoelectron spectroscopy depth profiling in normal emission geometry in the same XPS system. Sequential XPS depth profiling was performed utilizing a differentially pumped IQE 12/38 ion source operated with Argon (ion source Ar pressure 2×10^{-4} mbar, ion energy 3 keV, emission current 10 mA, ion current 1.5 A) and laterally scanning the Ar^{+} ions across the sample surface (scan area 5 x 5 mm^2). These setting enable a sputtering rate of 1.5 nm/min as determined based on the NEG layer thickness determined by XRF.

Initially, glow discharge optical emission spectrometry (GDOES) was also applied to analyze the bulk profile of the TiZrV coating. The problem to analyze a reactive material with the GDOES, as it is the getter, is that it requires of a UHV chamber for the measurement. If the UHV conditions are not achieved, the sample will react with the residual gas and the profile will be contaminated. The GDOES principle and some examples of analysis are presented in Appendix V.

5.3 Mandrel coating evaluation (step A)

The method to identify the impurities derived from the mandrel coating process was XPS depth profiling. The measurements were used to quantify the TiZrV composition along the depth and evaluate the presence of O and C in the NEG thin film. First, a reference sample of a standard coating from a cylindrical sputtering system is compared to a sample coated with the planar sputtering system, which is also used for the reverse NEG process in this work.

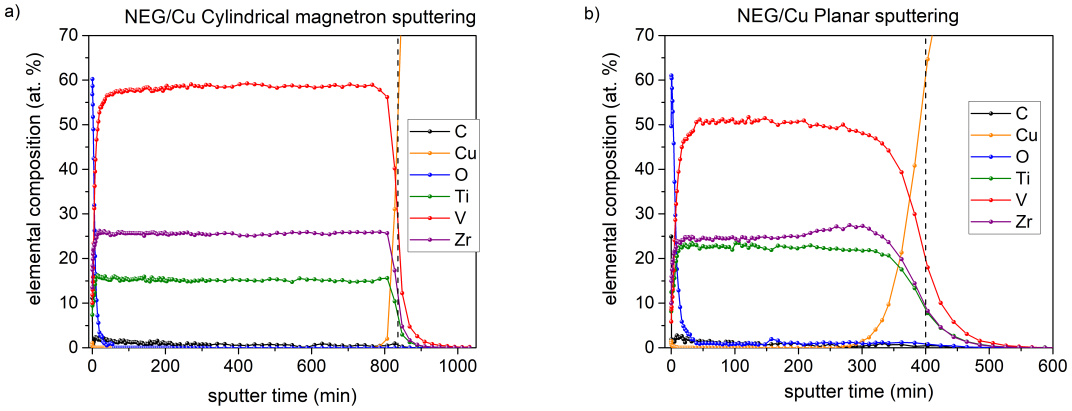

Figure 5.4. Elemental composition as a function of sputtering time, for the reference coatings: NEG on Cu OFE. In (a) from a standard cylindrical coating and in (b) from our planar sputtering coating (system used in the reverse NEG process).

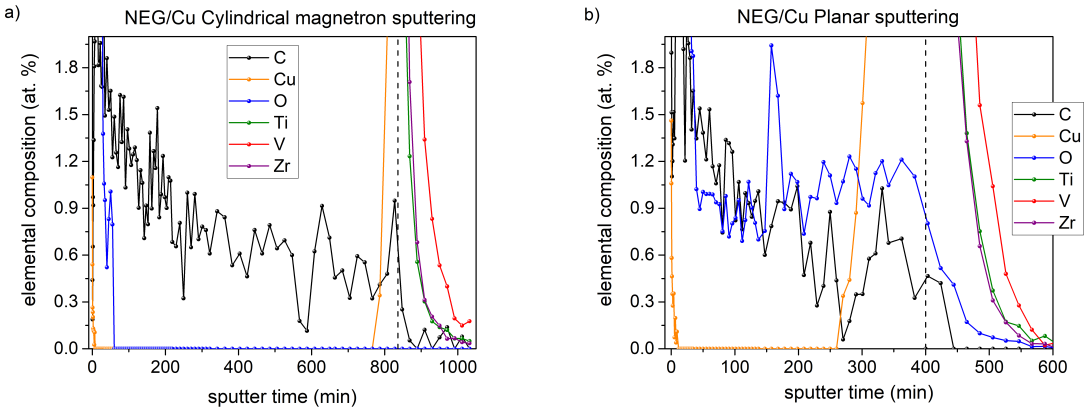

Figure 5.5. Zoom in Figure 5.4, for the reference coatings: NEG on Cu OFE. In (a) from a standard cylindrical coating and in (b) from our planar sputtering coating (used in the reverse NEG process).

Reference TiZrV samples were deposited on degreased OFE copper by DC magnetron sputtering [110] in a cylindrical or planar magnetron system. For the cylindrical system, inter-twisted 3mm diameter wires of Ti, Zr and V were used as cathode and sputtered with a Kr working gas at a pressure around 2.1×10^{-2} mbar. Samples were located at 46 mm from the cathode. For the planar sputtering system, a TiZrV cathode alloy was used in order to deposit the TiZrV

thin film by using Kr as sputtering gas at a pressure of 6.1×10^{-4} mbar and a cathode-substrate distance of 200 mm. The planar magnetron system is not baked out before coating, whereas the cylindrical system follows a step of baking at 200 °C for 24 hours before coating.

The XPS profiling of C, O, Ti, Zr, V and Cu are shown in Figure 5.4. The Ti, Zr and V compositions remain constant through the coating. The thickness of the samples from the cylindrical and planar sputtering are 1.1 and 0.6 µm, respectively. In order to visualize C or O in the bulk, the scale was enlarged (see Figure 5.5). Carbon is about 1% for the two coating systems. Oxygen is below the detection limit (0.2%) for the standard cylindrical coating and is around 1% in the case of the coating performed by planar magnetron sputtering. The latter is attributed to residual H_2O on the gas composition during the coating as the planar system can not be baked.

Samples from the reverse NEG were produced from aluminium platelets (AW-1050, 0.5 mm thickness) following the procedure Cu/NEG/Al described in Chapter 2 and using the electroforming bath procedure with the brightener. After mandrel etching and acidic rinsing, the sample was analyzed in XPS depth profile (thickness 1.2 µm) . The results are plotted in Figure 5.6. In this case, Ti, Zr, V compositions are not constant along the depth of the coating. V composition decreases when approaching the surface. However the composition is still within the good composition range evidenced by Prodromides [24]. Oxygen profile resembles the profile of the NEG on copper reference sample from the planar sputtering system, with a 1.5% of oxygen content in the bulk, which comes from the residual H_2O in the coating system. Carbon bulk content is similar than the one from the reference samples and possible comes from the XPS system itself.

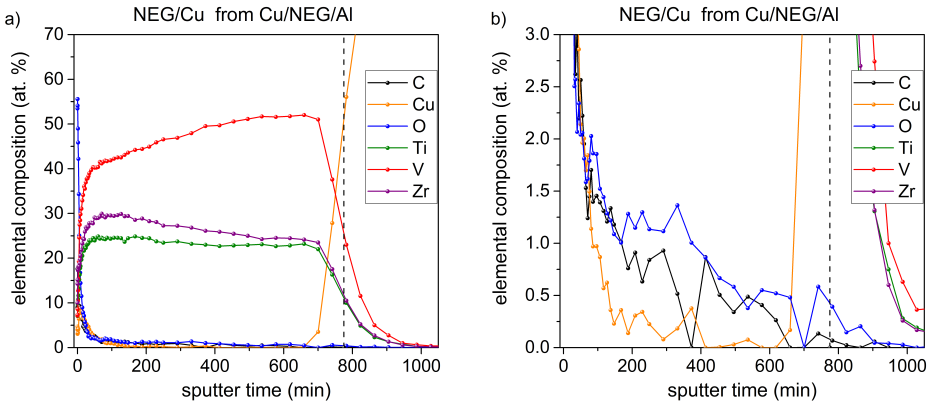

Figure 5.6. Elemental composition as a function of sputtering time, for the reverse NEG sample after mandrel removal. In (a) full scale is represented and in (b) the scale is enlarged for the comparison of impurities.

The three samples were fully activated in the XPS under the standard activation procedure. The single contamination of oxygen does not explain the delay observed in the real vacuum chambers.

5.4 Electroformed copper impurities (step B)

5.4.1 Copper electroforming sample preparation

The copper samples are produced on aluminium platelets of AW-1050 alloy, 0.5 mm thickness. These are copper coated at room temperature via magnetron sputtering using a cathode-substrate distance of 200 mm and using Kr as the sputtering process gas at a working pressure about 7×10^{-4} mbar for depositing 3 µm of copper layer before the electroforming begins (Figure 5.7). The two electroforming processes described in Chapter 2 were performed, DC plating in the presence of Gleam-PC brightener and pulse plating in the bath without additives.

Electroforming various thicknesses helped us to asses the concentration of different impurities as a function of the thickness of the deposit. In addition, the effect of applied current densities on the outgassing was also considered. The samples peeled off from the aluminium mandrel due to the stresses generated during the plating. This feature was encountered only in small flat samples, not in the chambers. Nevertheless, several tests proved that the aluminum etching step does not affect the content of impurities in electroformed copper. Sample size of 1cm x 1cm was required for the TDS measurements.

Figure 5.7. Platelets after copper PVD coating, before electroforming.

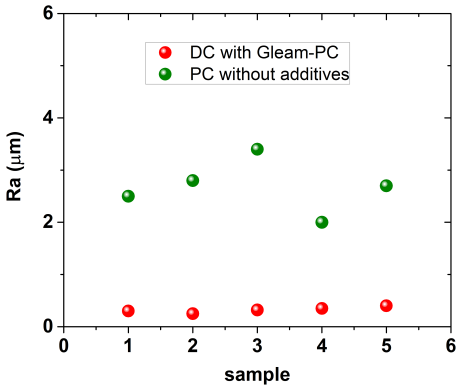

Figure 5.8. Surface roughness comparison between samples electroformed with the brightener (DC) and samples without additives (pulsed current).

Prior to the outgassing measurement, the roughness of several samples was measured using a non-contact optical profiler (Veeco Wyko - NT 3300). The roughness (Ra) values are indicated in Figure 5.8. The roughness of the plating layer without additives is one order of magnitude higher than when the brightener is used in the deposition. This will affect the total amount of adsorbed molecules on the sample surface.

5.4.2 Electroformed copper outgassing

An example of the overview of the outgassing from both electroformed copper samples is presented in Figure 5.9. For both cases, H_2 is the mayor impurity in the samples, and it outgasses between 400 °C - 700 °C. Water is the second most abundant specie and is outgassed in three defined regions: The first region is located at 100 °C and is ascribed to water desorbed from the surface, the second region is located in the 200 °C - 400 °C range and is attributed to water that is formed by the reaction of the H atoms which react in their diffusion path toward the surface with the oxygen from the surface oxide. Previous experiments in copper OFE [112] studied the nature of the peak and they discovered that the sample surface oxide thickness was directly related to the amount of water desorbed on the second peak. They concluded that the peak is the result of the reduction of the oxide layer by the hydrogen outgassing by the bulk. The third region over 600 °C is only observed for the pulse plating case and is ascribed to water stored in voids in the bulk. It desorbs with strong instabilities in the measurement signal.

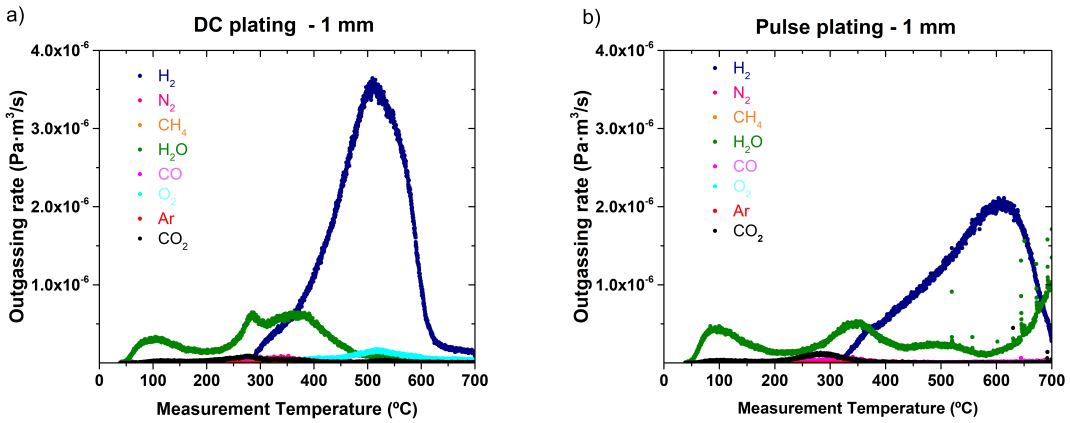

Figure 5.9. H_2, H_2O, O_2, CO_2, CH_4, N_2 outgassing for the DC (a) and PC (b) electroformed copper, 1 mm thickness, 4 A dm^{-2} cathodic current (for the pulse plated with t_{on}=7ms, t_{off}=8ms, $J_{average}$ of 1.86 A dm^{-2}).

Other species measured in the electroformed copper are CO_2 and O_2, which can be seen in the detailed logarithmic scale plot Figure 5.10. CO_2 is outgassed mainly at 120 °C and 300 °C. Additionally DC plated samples in the presence of a brightener exhibit an extra peak for CO_2 at 550 °C, which is not present in the pulse plated case. Carbon incorporation in copper deposits

when complex organic additives are used in the electrodeposition baths was reported by many authors [65,66]. The 550 °C peak could be attributed to the incorporation of the brightener into the layer. This is additionally supported by the release of O_2 at the same temperature 550 °C.

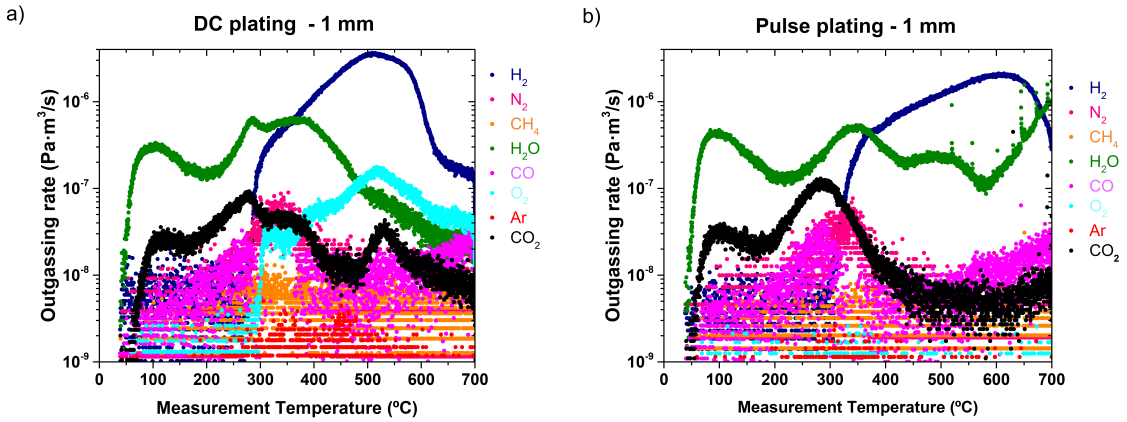

Figure 5.10. H_2, H_2O, O_2, CO_2, CH_4, N_2 outgassing for the DC (a) and PC (b) electroformed copper, 1 mm thickness, 4 A dm^{-2} cathodic current (for the pulse plated with t_{on}=7ms, t_{off}=8ms, $J_{average}$ of 1.86 A dm^{-2}) in log. scale.

The concentration corresponding to the desorbed impurities was measured by integrating the amount degassed up to 700 °C and then following Eq. 5.2 for the most important outgassed species: H_2, H_2O, O_2 and CO_2.

$$compound(atomic\ ppm) = \frac{mol\ compound\ outgassed}{10^{-6}\ mol\ Cu\ total} \tag{5.2}$$

All the concentrations in the following, labeled as atomic concentration, are given as molecules per atoms of Cu (i.e. H_2 molecules per Cu atoms).

In Figure 5.11 the H_2 content is evaluated for the different cases. For both electroforming baths, H_2 concentration increases with increasing the thickness of the deposit for all current densities of the present study. This is related to a drop of plating efficiency with prolonged plating time. The yield in average decreased from 97.5 % to 93.5 % for the DC electroforming and 91.7 % to 87.5 % for the pulse electroforming, both after 24 and 72 hours of plating respectively. This decrease can be attributed to different factors: deterioration of the anodes, uncontrolled temperature of plating or increase of derived products of the additives. In addition, higher currents could lead to a higher H_2 incorporation due to a slight shift towards the copper limited diffusion regime, but they also provide a lower plating time. Therefore there is a competition between the increased voltage and the decreased time of plating. For the DC plating with the brightener, the optimum with the lowest amount of H_2 was found at 2 A dm^{-2}.

In Figure 5.12 the H_2O outgassed concentration is shown for the different cases. The concentration decreases with thickness as the majority of the water is outgassed from the surface. The amount of degassed water in the pulsed electroformed copper is larger than in DC electroformed one, due to the surface roughness of the plating as seen in Figure 5.8. Additionally in some cases for the pulsed electroformed copper, water is desorbed from voids.

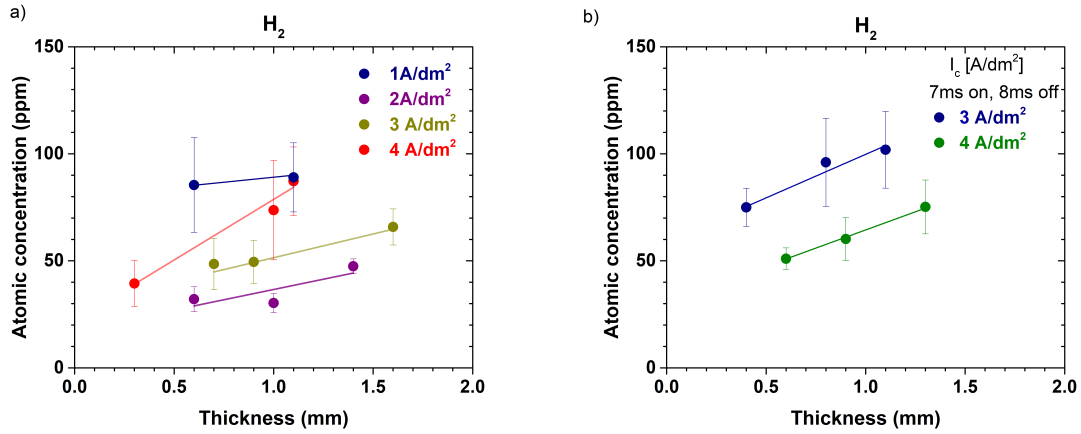

Figure 5.11. H_2 concentration (at. ppm) versus electroplated thickness for the (a) DC electroformed copper and (b) PC electroformed copper, at different current densities (for the pulse plated with t_{on}=7ms, t_{off}=8ms and given peak current density J_c).

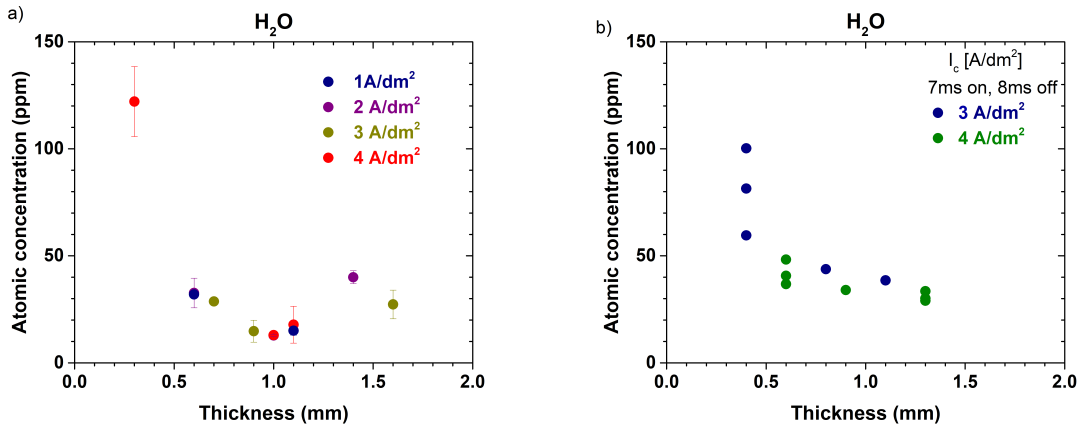

Figure 5.12. H_2O concentration (at. ppm) versus electroplated thickness for the (a) DC electroformed copper and (b) PC electroformed copper, at different current densities (for the pulse plated with t_{on}=7ms, t_{off}=8ms and given peak current density J_c).

The CO_2 concentration for the different scenarios can be seen in Figure 5.13. The concentration of CO_2 reduces with the plating thickness. The CO_2 outgasses mainly from the surface, but in some cases it is incorporated in the bulk of the sample (outgassed at high temperatures, as seen in Figure 5.10). The quantity of CO_2 (at.ppm) which is desorbed between (350 °C and 700 °C) is represented in Figure 5.14. The values are higher in the case of DC electroformed copper when compared to the pulse electroformed copper without additives. This can be attributed to CO_2, which is incorporated in addition by the bulk due to decomposition of adsorbed species from the brightener. In literature [50, 66, 67, 113], the incorporation of brightener derived species (C, S, Cl, O) into the deposit is observed.

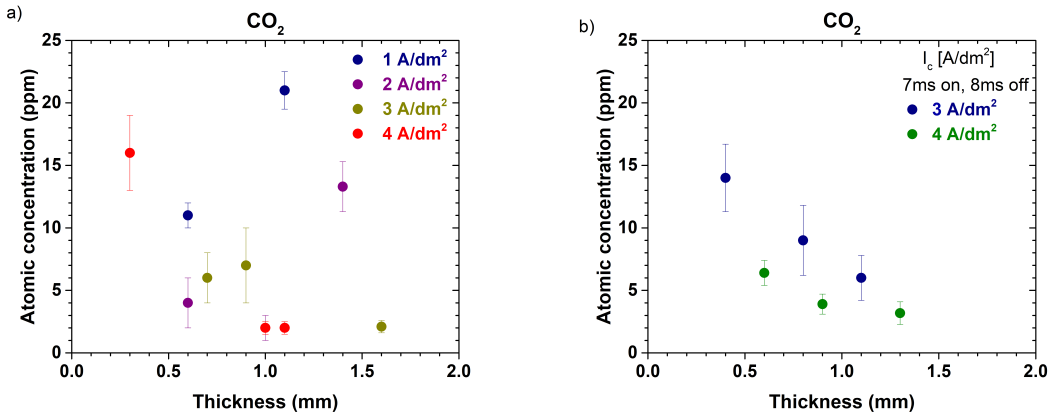

Figure 5.13. CO_2 concentration (at. ppm) versus electroplated thickness for the (a) DC electroformed copper and (b) PC electroformed copper, at different current densities (for the pulse plated with t_{on}=7ms, t_{off}=8ms and given peak current density J_c).

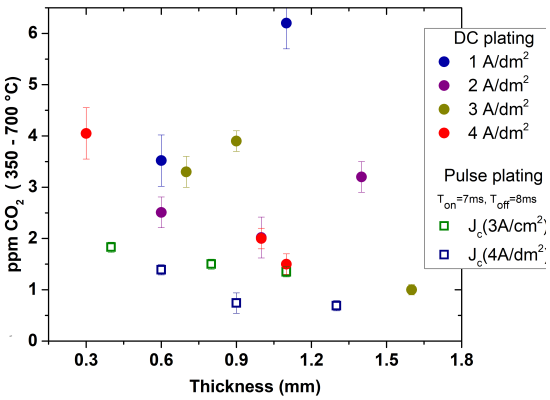

Figure 5.14. Concentration of CO_2 (at. ppm) which are outgassed between (350 - 700 °C) versus electroplated thickness for the DC electroformed copper (represented as a circle) and PC electroformed copper (represented as a square), at different current densities (for the pulse plated with t_{on}=7ms, t_{off}=8ms and given peak current density J_c).

In Figure 5.15, O_2 concentration is plotted (in logarithmic scale) for the different scenarios. The DC electroformed outgasses between 2-6 ppm of O_2 whereas the pulse plating without additives shows a very low amount, close to the background signal. The concentration remains constant for the different thicknesses. As seen before, there is evidence of incorporation of breakdown/oxidized species of the brightener during the plating. These are outgassed from the deposit in form of CO_2 and O_2.

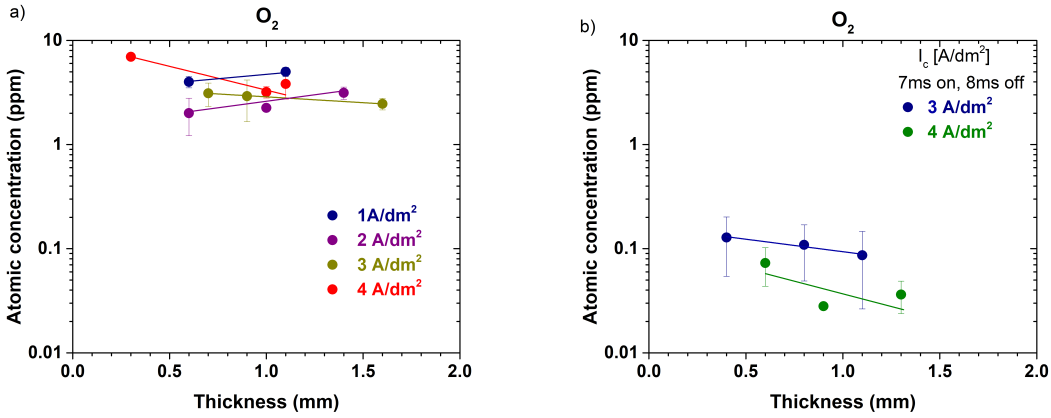

Figure 5.15. O_2 concentration (at. ppm, logarithmic scale) versus electroplated thickness for the (a) DC electroformed copper and (b) PC electroformed copper, at different current densities (for the pulse plated with t_{on}=7ms, t_{off}=8ms and given peak current density J_c).

5.4.3 Discussion and comparison with copper OFE

Both electroformed copper (DC plating in the presence of Gleam-PC brightener and pulse plating without additives) are compared with copper OFE. The impurity concentrations for a 1 mm thick sample are reported in Table 5.1. The values of H_2 and H_2O outgassing (converted in concentration) are much higher for both electroplated cases than for OFE copper. In addition for the DC electroformed copper, O_2 and more CO_2 are outgassed due to the brightener incorporation in the deposit.

The addition of brightener derived compounds to the plated layer is reported widely in literature [62, 64, 67, 113]. During plating, it is known that PEG and Cl^- ions bind to the copper surface and act as an inhibitor but it is suggested in previous publications that PEG is not incorporated in the plated film [67]. Carbon impurities may come from the organo-sulfide compounds used as accelerator or from the adsorption of the residual products of the brightener. Liu et al. [113] studied the effect of thermal annealing on the impurities incorporated in the deposit. They reported that C and O could be released during the annealing process but on the contrary, S and Cl were still strongly bound to the copper lattice. They additionally proposed that during annealing the O atoms bounded to C atoms could co-evaporate with C in the form of CO_x, reducing the oxygen incorporation in the film and oxygen could be released as free

oxygen O_2. Our results evidenced this desorption mechanism.

On the other hand, H_2 is produced by solvent reduction and depends on the plating yield of the electrolyte. The latter was shown to worsen with increasing plating time. A more detailed study is needed in order to understand the effect of other pulse parameters or other additives in the H_2 incorporation in the deposit. This will be covered in the next Chapter 6.

This study has confirmed that the electroforming process incorporates some impurities that are not present in such an extent in the bulk OFE. It is therefore plausible, that the difference between OFE and electroplated copper substrates has an influence on the activation and performance of the NEG layer. This will be studied in the step D.

The impurities can diffuse during the process of NEG activation and contaminate the thin film (see Figure 5.16). The activation of the getter occurs normally below 300 °C, thus the main impurities diffusing and desorbing in that temperature range are H_2O and CO_2 from pictures 5.9 and 5.10. The first peak of H_2O and CO_2 should not be considered because it is the surface coverage on the sample and in the case of the reverse NEG, it will not be present at the NEG/copper interface. In the absence of an oxide layer between the NEG thin film and the electroplated copper, as it is in our case, the second H_2O peak around 200 °C will also not occur. Atomic hydrogen will not react with the oxygen, but will diffuse towards the NEG. Therefore, the main impurities which could outgas between 200 and 300 °C are H_2 and CO_2.

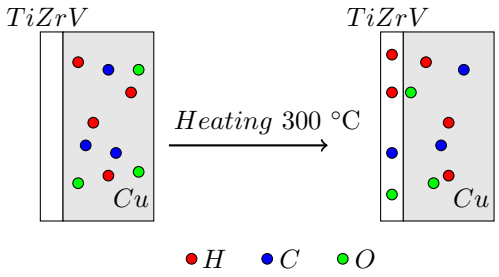

Figure 5.16. Possible difusion of impurities during the NEG activation process.

Table 5.1. Impurity concentrations for a 1mm thickness copper OFE and electroformed copper samples (the range of values on the electroformed samples include several current densities from Figures 5.11, 5.13, 5.12 and 5.15).

Concentration (at.ppm)	H_2	N_2	CH_4	H_2O	CO	O_2	Ar	CO_2
Cu OFE 1mm	4	0.4	0.7	3.8	0.6	0.03	0.02	1
Cu DC electroformed 1mm	30-90	1	0.5	10-15	0.3	2-6	0.2	2-10
Cu PC electroformed 1mm	40-80	0.8	0.8	30-50	0.5-1	0.02-0.1	0.2	2-6

5.5 Impurities on the getter film caused by mandrel etching (step C)

The impurities which could be trapped by the getter thin film during the wet chemical etching can be divided into two groups: surface and bulk impurities. Surface impurities come from the remaining traces of the aluminium after the etching, impurities in the aluminium alloy itself, or are residues from the etching solution [41]. They are detectable by XPS surface analysis and SEM inspection. Different rinsing steps were performed in order to eliminate these impurities from the surface of the getter thin film.

The effect of increasing the mandrel thickness on the transfer of impurities to the NEG layer was studied. Different XPS activation measurements were performed for samples coming from different aluminium mandrel thicknesses. Hydrogen is produced during the etching and could contaminate the getter thin film as a bulk impurity. In principle, the greater the thickness, the bigger is the amount of H_2 produced and the time of exposure of the thin getter film to the etching bath.

5.5.1 Surface impurities from aluminium mandrel etching residues

The main impurities for the two different aluminium alloys tested (AW-1050 and AW-6060) are given in Table 5.2. Fe, Mg and Si traces are the most prominant ones. Aluminium is efficiently removed by the etching bath of NaOH, but some of the impurities have a low solubility in the basic solution (see Figure 5.17). Therefore, a rinsing method was developed in order to remove these impurities.

Table 5.2. Aluminium AW-1050 and AW-6060 main impurities (maximum concentration w.%).

Al type	Cu	**Fe**	**Mg**	Mn	**Si**	Ti	Zn
AW-1050	0.05%	**0.4%**	**0.05%**	0.05%	**0.25%**	0.03%	0.05%
AW-6060	0.1%	**0.3%**	**0.6%**	0.1%	**0.5%**	0.1%	0.15%

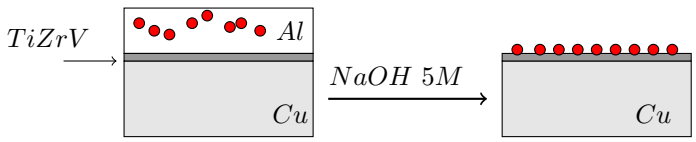

Figure 5.17. Surface impurities from aluminium mandrel etching in NaOH 5M.

First studies on flat samples confirmed the presence of surface impurities [41]. Aluminum flat platelets (AW-1050 alloy, 0.5 mm thickness) were TiZrV and copper coated, and then copper electroformed as described in the procedure in Chapter 2 (Cu/NEG/Al). After aluminium mandrel dissolution, Fe remaining traces were visible by SEM and XPS (concentration between 6-12 at%). If ammonium persulfate (200 g/l, 30 sec) acidic rinsing is added to the procedure, the impurities are removed from the TiZrV surface (see Figure 5.18).

The samples with and without acidic rinsing followed an activation in the XPS following the standard cycle described in Section 5.2.2. The samples with Fe residues on the surface [41] showed a high oxygen concentration after the last heating step at 250 °C. With the addition of ammonium persulfate (AP) rinsing to the cleaning procedure, Fe traces are removed from the surface and the oxygen in the surface decreases to reach a full activation (greater than 67%) as seen in Figure 5.19.

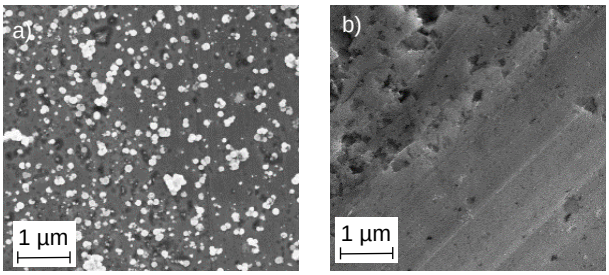

Figure 5.18. SEM images from TiZrV surface after aluminium dissolution with NaOH 5M, without acidic Ammonium persulfate (AP) rinsing, with Fe residues on the surface (a) and with rinsing (b).

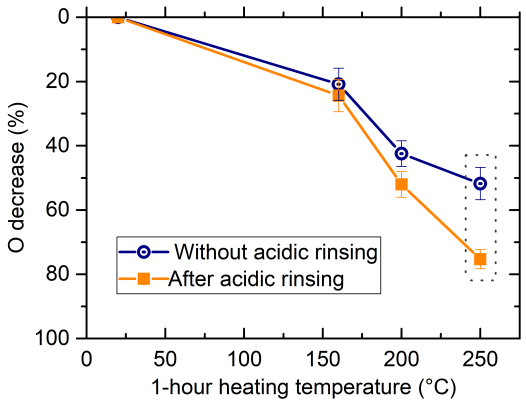

Figure 5.19. O1s peak area decrease as a function of the activation time and temperature for the TiZrV coated samples after aluminium mandrel (AW-1050, 0.5 mm thickness) dissolution with NaOH 5M, with/out acidic Ammonium persulfate (AP) rinsing.

The metallic line shift was also investigated for both cases. After the heating steps for activation, the peaks of Ti, Zr and V shift from oxidized state to metallic state [41] (detailed in Figure 5.20). It is observed that at 250 °C both cases with or without AP rinsing exhibited completely TiZrV metallic lines. On the contrary, if we follow the shift for the iron impurities, in the case without AP rinsing, another situation is found. The traces, which at room temperature are oxidized Fe_2O_3 particles, are reduced to FeO during heating, but do not reduce further to the metallic state. The surface impurities do not prevent the Ti, Zr and V peaks to reduce to the metallic state. However, the particle coverage will prevent pumping of gases, hence the acidic rinsing was added to the procedure.

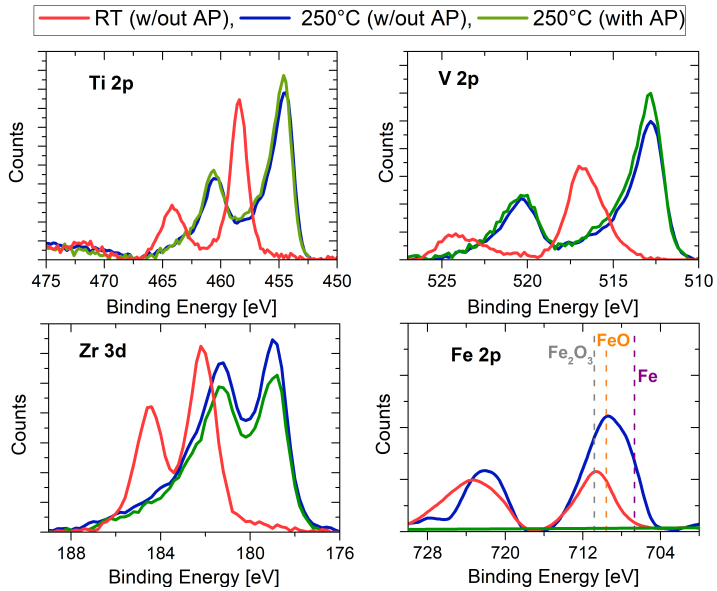

Figure 5.20. Ti2p, Zr3d, V2p and Fe2p peaks of TiZrV after aluminium mandrel (AW-1050, 0.5 mm thickness) dissolution, at room temperature (in red) and after activation at 250 °C following the standard cycle of activation.

5.5.2 Bulk impurities from etching bath

During aluminium etching, hydrogen is produced. The getter is then exposed to it and part of it could be incorporated as a bulk impurity (or pumped). The thicker the aluminium mandrel, the bigger the quantity of hydrogen that it is produced and also the bigger the time of etching. Different aluminium thicknesses were evaluated within the work: from 0.5mm to 1.5mm, which require etching times from 7 to 30 hours, respectively. Furthermore, two different alloys: AW-6060 and AW-1050 were evaluated. Different aluminium flat mandrels were prepared following the procedure Cu/NEG/Al described in Chapter 2. After the aluminium NaOH etching, an acidic AP rinsing was performed in all cases.

Table 5.3. XPS surface analysis of TiZrV surface after different aluminium mandrel (alloy and thickness) dissolution with NaOH 5M, with acidic Ammonium persulfate (AP) rinsing.

Sample ID	Mandrel alloy	Mandrel thickness	XPS Surface concentration (at %)						Relative metallic composition (TiZrV %)		
			C	O	Na	Fe	Mg	Si	Ti	V	Zr
NEG/Cu	AW-1050	0.5 mm	28.7	52.2	-	-	-	-	37.6	37.1	25.3
NEG/Cu	AW-1050	1 mm	28.7	51.6	-	-	-	-	34.7	44.1	21.2
NEG/Cu	AW-1050	1.5 mm	25.5	54.1	0.4	-	-	-	37.0	38.1	24.9
NEG/Cu	AW-6060	0.5 mm	39.0	43.3	-	-	-	-	35.1	35.8	29.1
NEG/Cu	AW-6060	1.5 mm	24.0	53.9	1.3	-	-	-	46.1	33.4	20.3

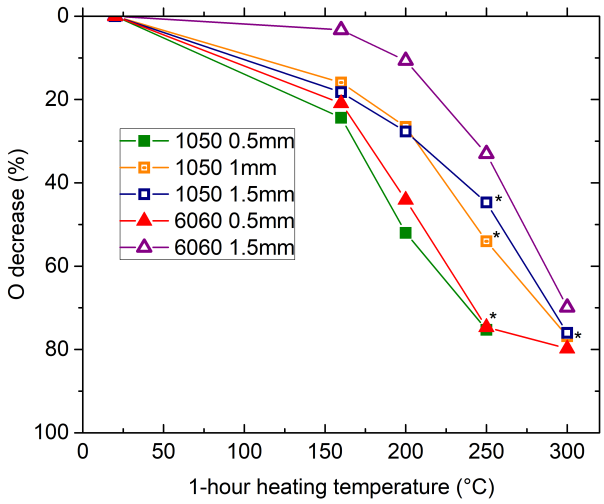

Figure 5.21. O1s peak area decrease as a function of the activation time and temperature for the TiZrV coated samples after aluminium mandrel etching. The mandrels vary from AW-1050 to AW-6060 aluminium alloys and 0.5 -1.5 mm thickness.

XPS surface analysis and activation was performed for the different mandrels (as seen in Table 5.3 and Figure 5.21). No aluminium impurities were observed on the surface of the TiZrV. Although, Na traces were sometimes observed. All the samples followed the activation procedure, in this case extended to 300 °C in order to achieve a full activation. The thinnest aluminum samples (0.5 mm) activated at 250 °C. The thicker the aluminium, the more is delayed the activation i.e. the decrease of the surface oxygen signal. All samples activated after the full cycle up to 300 °C.

The second evaluation parameter is the shift of the metals from oxidized to metallic state. In this case the peaks can be followed in the case of AW-1050 alloy for the thickness of 0.5 to 1.5 mm. The collected signals form Ti, Zr and V after (a) 250 °C and (b) 300 °C are shown in Figure 5.22.

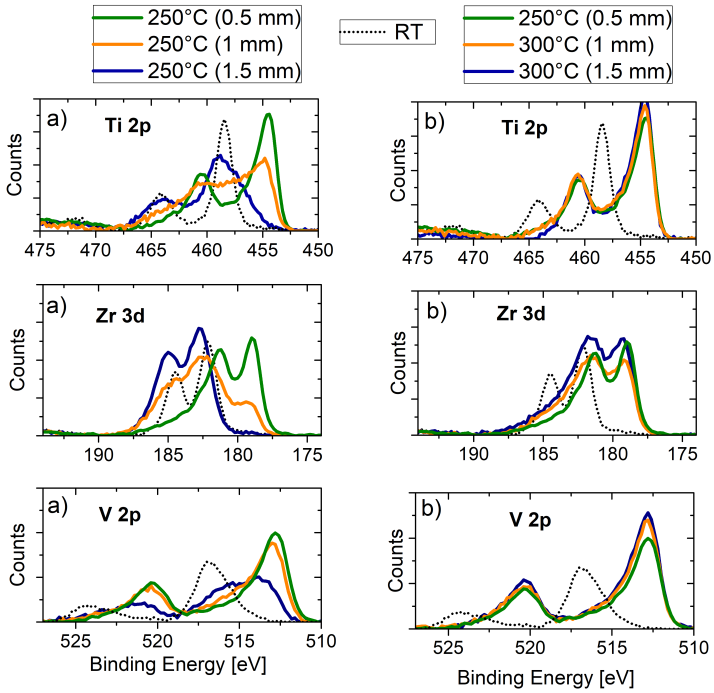

Figure 5.22. Ti2p, Zr3d, V2p peaks of TiZrV after aluminium AW-1050 mandrel (0.5 mm to 1.5 mm thick) dissolution. The lines are given at room temperature, and after activation at (a) 250 °C and (b) 300 °C. The equivalent sample is marked with * in Figure 5.21.

After activation at 250 °C, the analysis of the peaks reveals the presence of mainly metallic components of Ti and V for the 0.5 and 1 mm thickness mandrels while the Zr signal, which is the most sensitive in terms of activation due to its higher binding energy with oxygen, shows still a strong oxide component for the 1 and 1.5 mm thickness mandrel. Instead, the 0.5 mm mandrel shows a complete shift of the peaks to metallic state. In case (b), the samples are activated for one more hour at 300 °C and the three elements are completely reduced to the metallic state for all thicknesses.

From the results, the only plausible explanation is that the bulk impurities from the thin mandrel etching can be diluted in the NEG coating whereas for the thickest mandrel, the impurities are not completely diluted and the diffusion of the oxygen is therefore delayed. By increasing the time or temperature of the activation process, samples from the thicker mandrel also activate. These results also confirm that both aluminium alloys can be used as mandrel, which is very positive in the point of view of scaling up the process and using cheaper materials to build the mandrel.

In Chapter 4, different chambers were built by employing different aluminium mandrel alloys and thicknesses (Figure 4.30). The H_2 sticking factor at 230 °C was smaller when a thicker mandrel was selected in comparison to a thin mandrel. Although, the differences are small. From the XPS results, the 0.5 mm mandrel coating activates at low temperatures and does not contain surface impurities.

5.6 Diffusion of impurities during the chamber activation process (step D)

XPS bulk depth profile analysis was used in order to investigate the diffusion of impurities from the electroformed copper to the thin film during the sample activation procedure. A reverse NEG sample produced from aluminium platelets (AW-1050, 0.5 mm thickness) following the procedure Cu/NEG/Al described in Chapter 2 (thickness 1.2 µm) follows one activation step, according to the standard activation cycle, which reduces the TiZrV surface oxide to the metallic state. This will emulate the activation procedure of a real NEG chamber.

The oxygen concentration profiles are plotted together with those of a standard NEG which has been produced in the cylindrical magnetron sputtering system (the standard reference for NEG coated chambers) in Figure 5.23a. The standard NEG is measured after deposition (green line, also presented in Figure 5.5a) and after 4 cycles of activation (in black) with venting steps in between (aged). After activation, the O1s profile exhibits the concentration which is caused by the diffusion of the oxygen from the surface oxide to the bulk, although this only happens within the first 1/3 of coating thickness. This is explained because the activation procedure, 250 °C in the standard activation cycle, does not allow to the oxygen to be completely diffused through the bulk. Thus, the equilibrium is not reached and as a consequence, oxygen atoms settle in the film with a higher concentration close to the surface.

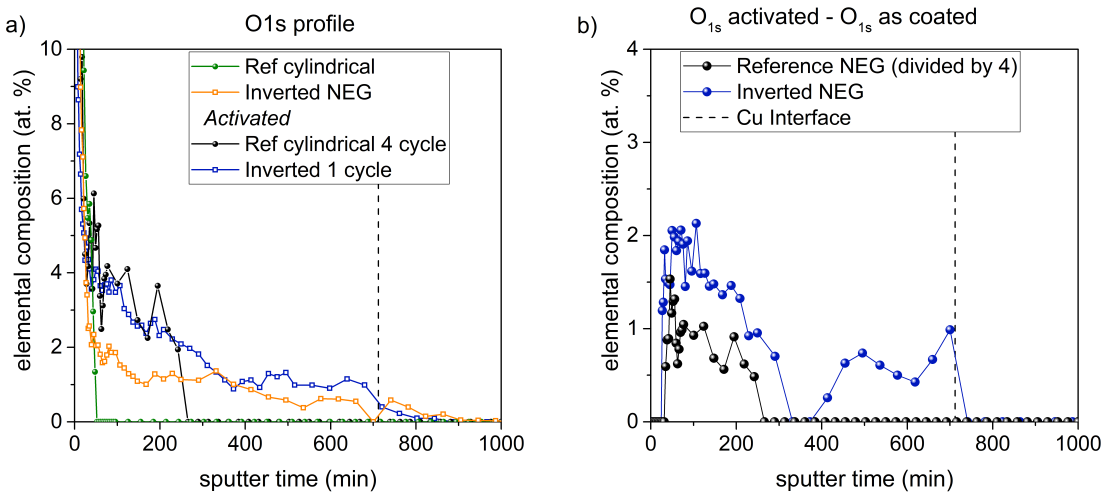

Figure 5.23. In (a) O1s composition depth profile for the different situations. In (b) subtracted O1s composition profile (activated against fresh sample). The reference sample is divided by 4 to represent just one activation cycle.

The second analysis is done on the inverted NEG samples. The oxygen profile after mandrel etching is represented in orange in Figure 5.23a. For this sample, oxygen is found to be a bulk impurity after the coating (step A). In addition, the oxygen profile (blue line) after one activation step (standard cycle) shows the effect of the surface oxygen diffusion in the bulk. However

in the inverse sample, the oxygen concentration also increased very deep in the bulk, a fact which could be originated from diffusion of impurities from the electroformed copper (as it can be seen in the subtracted profile of Figure 5.23b).

A proposed oxygen diffusion mechanism is exposed on Figure 5.24b.

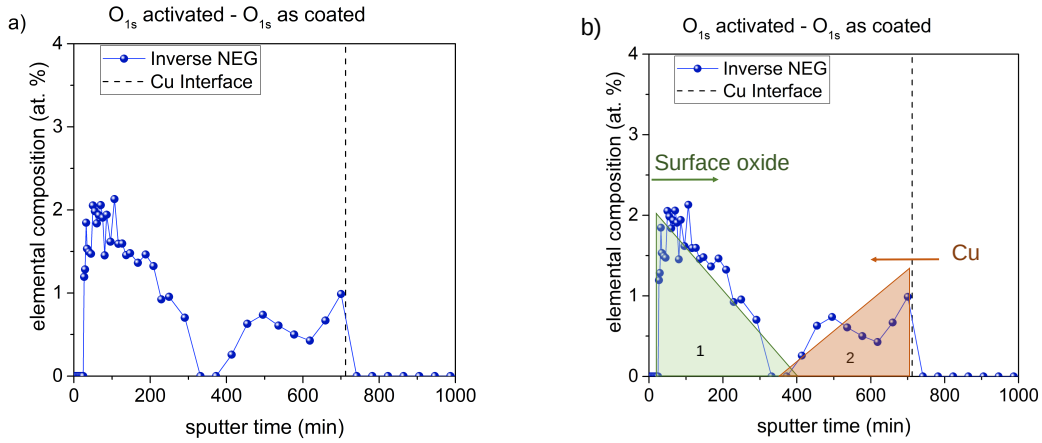

Figure 5.24. In (a) subtracted O1s composition profile (activated against fresh sample) for the Inverted NEG sample. In (b) proposed oxygen diffusion mechanism.

As observed in Figure 5.24, an increase of the concentration in the bulk without an increase in the middle of the coating can not be explained as simple diffusion from the surface side. Therefore, the area represented in green, is attributed to the accumulated oxygen due to the diffusion of the oxygen from the surface oxide into the bulk, and the area represented in red, is attributed to the oxygen incorporation due to the diffusion from the copper electroformed bulk.

5.7 Discussion of the results

A table which summarizes the impurities in each of the production steps is displayed in Table 5.4. For the electroformed copper calculation, only H_2, O_2 and CO_2 gases were taken into account. The H content was only measured in the step B of the process.

Table 5.4. Calculated impurities for each step of the process. Unknown values are represented with a question mark.

Atoms impurity* in NEG/Cu	H	C	O	M
A: Coating (from XPS)	?	-	4-6 $\times 10^{16}$	-
B: Electroformed copper (from TDS)	4 -9 $\times 10^{17}$	5 $\times 10^{15}$ - 3 $\times 10^{16}$	3 $\times 10^{16}$ - 1 $\times 10^{17}$	-
C: Etching	?	-	-	-

*Number of atoms for a 1 mm thick copper sample of $1cm^2$ area with a NEG coating of 1 µm.

To understand the effect of a contaminated bulk on the pumping performance, a simple model can be taken into consideration. If we assume that after each activation temperature the oxide layer is completely diluted in the bulk, we can propose a relationship between the H_2 sticking factor and the oxygen in the bulk assuming that: i) only the surface sites not occupied by oxygen are able to chemisorb hydrogen, ii) the adsorption of hydrogen is dissociative [32].

Assuming that the oxygen concentration in the surface (c) is proportional to that in the film, the fraction of surface sites occupied by oxygen Θ is:

$$\Theta = \frac{c}{c_{sat}} \tag{5.3}$$

Where C_{sat} is the saturation concentration (1×10^{22} atom cm^{-3}). The sticking factor of H_2 is calculated assuming a Langmuir adsorption model, following equation 5.4. The data is represented in Figure 5.25.

$$\alpha_{H_2} = \alpha_0(1-\Theta)^2 = \alpha_0(1 - \frac{n \cdot N_{ox}}{L_{film} \cdot c_{sat}})^2 \tag{5.4}$$

Where α_0 is the initial sticking factor (1×10^{-2}), N_{ox} is the number of oxygen atoms in the oxide layer (1×10^{16} atom cm^{-2}), n is the number of venting cycles, and L_{film} is the thickness of the coating since we assume that the oxygen will diffuse completely in it (in this case is set to 1 µm).

The Langmuir model involves the following assumptions:

- The adsorption energy for all sites is the same and it is unaffected by adsorption in neighboring sites
- Each site accommodates only one adsorbed particle
- Adsorbed atoms do not interact with each other

In reality, this estimation turns to be too optimistic, since the oxygen during the activation procedure does not diffuse homogeneously in the bulk and generates a gradient profile close to the surface.

In addition, the presence of hydrogen in the NEG bulk will also decrease the number of available pumping sites. It is important to remember, that O and H impurities are bonded to the NEG

differently. H would be released during the activation process and thus the amount will decrease in the getter. On the other hand, oxygen will remain in the bulk and will always disturb the pumping performance.

Measurements done at CERN, studied the recovery of a TiZrV film saturated with H_2. Firstly, a stainless steel chamber was NEG coated following the standard cylindrical technique. After the NEG activation at 250 °C for 24 hours, 1.4×10^{17} molecules cm^{-2} of H_2 were injected and pumped by the NEG film, causing a decrease in the pumping speed to 2% of its starting value. Afterwards, another activation followed without venting step in between, for 24 hours at 250 °C in which the getter recovered 50% of its original H_2 pumping speed and the full CO saturation capacity. During the activation, only 10% of the hydrogen was released and the rest remained in the coating. The decrease in pumping speed was caused by the saturated TiZrV bulk.

As a conclusion, the delayed activation and lower pumping speed at low temperatures can be explained as result of the effect of the process impurities (H and O). Higher activation temperatures or times are needed in order to dilute the impurities into the bulk and achieve a low concentration close to the surface.

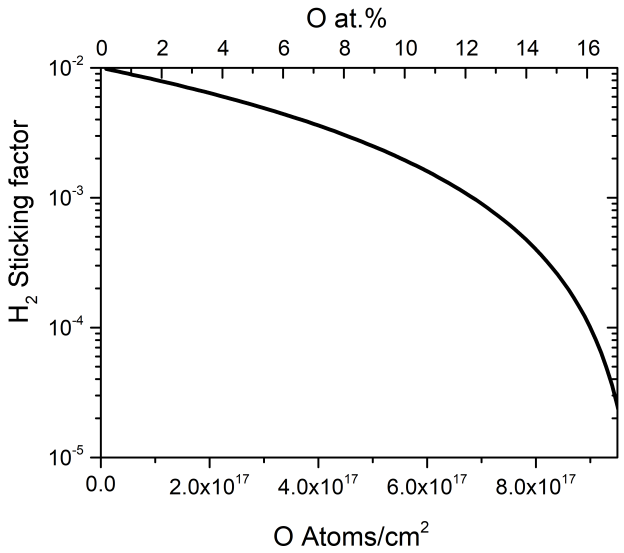

Figure 5.25. Estimated sticking coefficient against the number of O atoms in the bulk or the atomic percentage (at.%) following equation 5.4.

6 Hydrogen trapping and desorption in electroformed copper

The presence of hydrogen on electroformed copper from two different acidic copper sulphate solutions was evaluated in pulsed current mode: an additive-free solution and a solution including a sugar. D-xylose addition is found to inhibit the H incorporation and allows higher cathodic pulse currents before reaching the copper diffusion limited range. TDS experiments show the release of hydrogen trapped into the copper under two different forms. Hydrogen from copper vacancies was found on all samples at an outgassing temperature around 450 °C. For samples with long pulse on-time, an additional H_2 outgassing peak was found around 600 °C. XRD measurements allowed us to determine the preferential orientation of the plated samples and to monitor the lattice parameter evolution with increasing temperature.

6.1 Introduction

From the results of chapter 5, hydrogen is found to be the major impurity in the electroformed copper, which is generated by solvent reduction and thus trapped in the coating. Up to this point, the electrolytes as well as the process parameters (pulse current, temperature) used for vacuum chambers production came from well-known workshop processes at CERN (described in chapter 2). Therefore, it is desirable to test different electrolytes and pulse parameters in order to understand possible optimization routes.

The overall reaction of hydrogen evolution in an acid solution medium is [114]:

$$2\,H^+ + 2\,e \longrightarrow H_2 \tag{6.1}$$

If we assume that the diffusion of the protons from the bulk of the solution to the electrode and the hydrogen molecule evolution to the atmosphere are fast processes, we can describe the mechanism of the cathodic reduction of hydrogen in two steps:

- Charge transfer : $H^+(\text{electrode}) + e \longrightarrow MH$ (1)
- Hydrogen combination: $2\,MH \longrightarrow 2\,M + H_2(\text{electrode})$ (2)

Where MH is the hydrogen adsorbed at the electrode M (H_{ads}). This mechanism is further complicated by the fact that the combination step (2) can proceed in either two ways:

2a. Chemical desorption in which the adsorbed atoms combine to form molecular hydrogen:

$$H_{ads} + H_{ads} \longrightarrow H_2(\text{electrode}) \tag{6.2}$$

2b. Electrochemical desorption or ion-atom combination:

$$H_{ads} + H^+ + e \longrightarrow H_2(\text{electrode}) \tag{6.3}$$

Hence, there are two kinetic paths for hydrogen evolution, each consisting in two steps. The first path consists of charge transfer followed by chemical desorption and the second path is charge transfer followed by electrochemical desorption. One of the steps from each path can be slow and thus the rate determining step.

In Literature, hydrogen presence in electroplated copper is reported by many authors [62]. Gubin et al. [115] found that hydrogen can be present in different bound states and its concentration was found to be five to six orders of magnitude larger than the equilibrium solubility of hydrogen at room temperature. Other thermal desorption spectroscopy studies on electrodeposited copper revealed a pronounced H_2 outgassing peak, which was ascribed to the break-up of vacancy hydrogen clusters [116]. In particular, low impurity deposits were found when pentoses were used as additives [62]. D-xylose addition to the bath, produced very pure copper deposits and low hydrogen concentration in the deposit [48, 62, 69].

Furthermore, the use of pulse current in electrodeposition has been the target of many research papers [71, 74, 117, 118] as well as of industrial applications protected by patents [119, 120]. Ibl and Puippe [74, 121] found that each parameter which can be varied in pulse electroplating (on-time, off-time and current density) affects the properties of cadmium deposits. An increase in the off time leads to a decrease in the grain size. They explained the mechanism in terms of adsorption effects. During off-time there is adsorption of inhibitor species, resulting in a larger inhibitor coverage and crystal growth is inhibited. On the contrary, an increase in on-time leads to larger grain growth, since the ratio of the metal deposited to the amount of substance adsorbed increases, resulting in a less effective inhibition (see Figure 6.1).

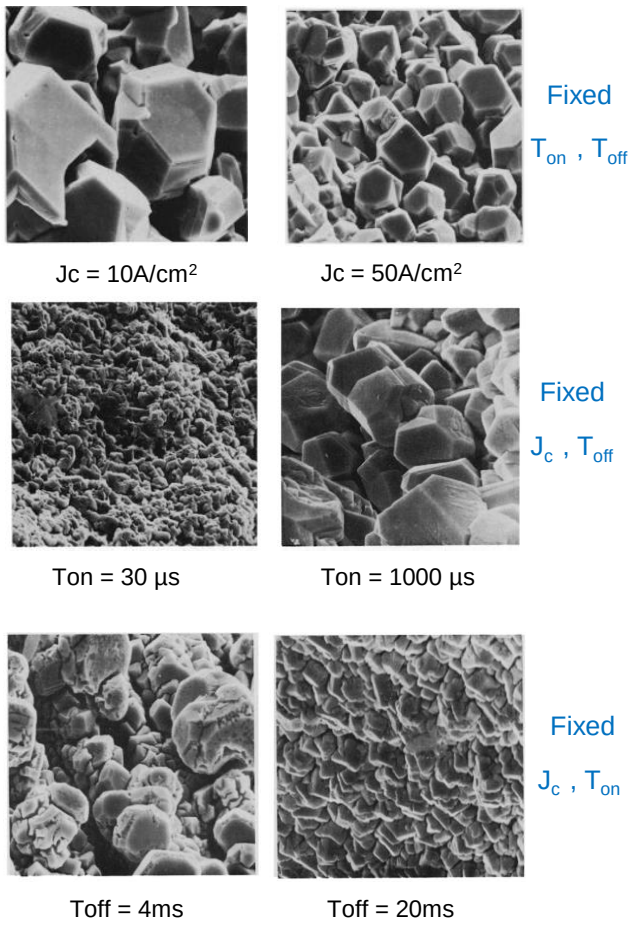

Figure 6.1. Influence of pulse parameters (peak current, on-time and off-time) on the structure of Cadmium deposits. From Ibl et al. [121].

The use of pulse current in copper plating and the influence on the incorporation of additives has also been studied [122–124]. De la Pena et al. [125] evidenced the effect of pulse parameters on copper coatings properties (crystalline structure and grain size) when a commercial additive is employed in comparison to a additives free bath. They reported that the mechanical and electrical properties were enhanced when pulse plating was applied, since a lower number of defects was produced in the plated layer. Imaz et al. [126] found that pulse plating and addition of agents mutually interfere with each other, causing changes in the microstructure that lead to changes in the mechanical properties of the deposits. Other studies [127, 128] show that pulse current improve deposit morphology and offers a large number of parameters for optimization (i.e. on-time, off-time, cathodic and anodic pulse, pulse duration). Pearson et al. [76] reported that the use of reverse pulse plating on the copper sulphate electrolyte containing organic additives changed the mechanism of adsorption of the additives in the deposit structure.

When applying pulse current, several parameters must be chosen: on-time, off-time and peak current. Already seen in Chapter 2, the typical pulse current wave form is shown again in Figure 6.2. The peak current density, j_c, is the imposed cathodic current during the on-time, t_{on}. The pulse period, T, is the sum of t_{on} and t_{off} and the duty cycle, θ, is given by t_{on}/T.

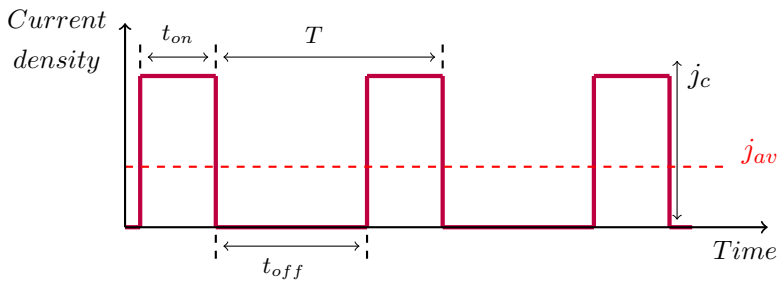

Figure 6.2. Schematic of pulse plating sequence and definition of the parameters.

Transient curves allow us to study the electrochemical behavior of different pulse parameters [117]. The transient curve is defined by five different regions (see Figure 6.3):

- Double layer loading. The ions go from the bulk of the electrolyte to the electrode surface
- Faradic range. The copper reduction takes place $Cu^{2+} + 2\,e \longrightarrow Cu$
- Diffusion limited range. The rate of the deposition is limited by the diffusion of the copper ions to the cathode
- Hydrogen permanent release
- Double layer discharge

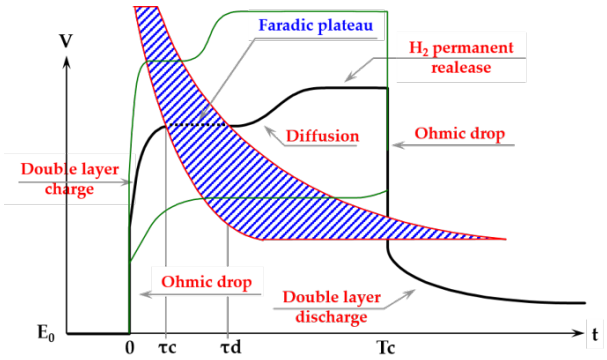

Figure 6.3. Transient curves example with identified regions. In blue is represented the Faradic plateau.

Furthermore, the faradic plateau is found by varying the peak current density, j_c or the off time, t_{off}, of the pulsed sequence. In this case, it is represented in blue in Figure 6.3).

In addition, τ_c and τ_d can be extracted from the transition curves. τ_c is the time needed for the charge of the double layer to occur and τ_d is the time when the process is limited by the diffusion of ions in solution, or also called transition time. The transition time can be calculated for the various pulse currents densities according to Sands Equation 6.4 [129].

$$\tau = \frac{\pi D_{Cu} C_{Cu}^2 (zF)^2}{4 J_c^2} \tag{6.4}$$

Where D_{Cu} is the diffusion coefficient of copper in the electrolyte ($m^2\,s^{-1}$), C_{Cu} is the copper concentration (mol m^{-3}), F is the Farady constant ($96\,485\,C\,mol^{-1}$), J_c is the peak current density (A m^{-2}) and z is the number of electrons taking part in the reduction reaction.

The aim of the present chapter is the evaluation of the effect of two main triggers, namely polarization wave modulation and copper electrolyte composition, by the addition of d-xylose, on the hydrogen production and the possible further hydrogen incorporation in the electroplated deposit.

6.2 Methods

Two acidic copper sulphate electrolytes were prepared, made up of $115\,g\,l^{-1}$ $CuSO_4\,5\,H_2O$, $165\,g\,l^{-1}$ H_2SO_4, and $0.075\,g\,l^{-1}$ Cl^-. Additionally, in the second bath, d-xylose ($OCH(CHOH)_3CH_2OH$, pentose) was added in a very low concentration as shown in Table 6.1.

Table 6.1. Bath concentrations of the two electrolytes.

	Bath without additives	Bath with d-xylose
$CuSO_4\,5\,H_2O$ ($g\,l^{-1}$)	115.0	115.0
H_2SO_4 ($g\,l^{-1}$)	165.6	165.5
NaCl ($g\,l^{-1}$)	0.124	0.124
d-xylose ($g\,l^{-1}$)	-	0.033

The cathodic polarization curves were recorded with a three-electrode cell connected to a PGZ 301 potentiostat (from Radiometer). The set-up consists of a rotating working electrode made of copper, a Pt counter electrode and a SCE electrode as reference. Curves were recorded by Linear Sweep Voltammetry starting at the OCP (41 mV vs. SCE) at a rotation speed of 400 rpm.

Transient curves were recorded in an experimental set-up, which consisted of a three-electrode cell which is connected to a PRT 20-2 type potentiostat, which is used to impose a rectangular current pulse, from which transient curves in potential were derived by the addition of a resistance [130]. A Scopix OX 7102-C oscilloscope is used to record the transient curves. The cell includes a rotating working electrode made of copper rotating at 400 rpm, a Pt counter electrode and a SCE electrode as reference. Pulse sequences were designed to deliver rectangular cathodic pulses with an amplitude ranging from $40\,\mathrm{A\,dm^{-2}}$ to $100\,\mathrm{A\,dm^{-2}}$, for a given cathodic time of 100 ms (T_{on}). Time off (between the rectangular pulses) was adjusted to keep a constant average current of $2\,\mathrm{A\,dm^{-2}}$ as seen in Equation 6.5.

$$J_{average} = \frac{J_{on} \cdot T_{on}}{T_{on} + T_{off}} \tag{6.5}$$

The electroformed samples followed the same production process. At the first stage of the process, aluminum flat mandrels were copper coated on one side in order to have an adherent layer for the subsequent plating. Flat aluminum samples of 2.5 cm x 2.5 cm, AW-1050 alloy, 99.5% purity, were copper coated at room temperature via magnetron sputtering using a cathode-substrate distance of 200 mm, using Kr as the sputtering process gas at a working pressure about 7×10^{-4} mbar for depositing 3 µm of copper layer. Electroforming was carried out in the two baths described using copper phosphorized anodes and magnetic stirring at a temperature of 25 °C with a Micronics System LabPulse model with an output current range of ±5 A and a voltage range of ±10 V.

The samples were masked on the external side and plated during 24 hours at an average of $2\,\mathrm{A\,dm^{-2}}$ in order to achieve a theoretical thickness of 634 µm (equation 1.5) following the respective pulse sequence for the two different electrolytes. Finally, the electroformed copper layer was peeled off from the aluminum flat parts.

To monitor the amount of incorporated hydrogen, thermal Desorption Spectroscopy analysis (TDS) was carried out in the ultra-high vacuum system described in Chapter 5.2.1. The gases desorbed during the thermal ramp are measured as a function of temperature by the calibrated RGA at a $10\,^{\circ}\mathrm{C\,min^{-1}}$ step rate from 20 °C to 700 °C. Sample size of 1cm x 1cm was required for the TDS measurements.

The X-ray diffraction (XRD) experiments were conducted using a D8 Advance Bruker diffractometer, in Bragg-Brentano geometry. The in-situ high-temperature chamber consisted of a HTK 1200 ANTON PAAR cell. A Cu Kα source, operated at 40 kV and 40 mA, and a Ni filter were used. After an optimization study where the heating ramp varied from 10 °C/min to 30 °C/min, the lowest was chosen and samples were heated at 300 °C, 500 °C and 700 °C at a measured ramp of $10\,^{\circ}\mathrm{C\,min^{-1}}$ in the diffractometer, which is in accordance with the TDS

protocol. Measurements were carried out under vacuum (1 mbar). For the measurements, 2Θ was used between 40 and 95°, with a step width of 0.02° and a scan speed of 0.3 s/step.

6.3 Electrochemical behaviour of both electrolytes

Kang et. al [131] and de la Pena et al. [132] studied the effect of additives in the polarization curves of the electrolytes. Kang [131] studied the effect of thiourea (TU) addition and reported that even a small amount of additive changed the I-V plot. The current density reduced and the cathodic reduction peak shifted into a more cathodic direction. This was attributed to the generation of new species from the reaction of TU with copper ions which inhibited the cathodic consumption of copper ions. De la Pena and Roy [132] studied the effect of commercial additives (copper Gleam A and copper Gleam B) on the cathode polarization when the additives were used separately or combined. They reported that copper Gleam B and Cl^- showed a strong inhibition, but when combined with copper Gleam A promoted acceleration and the limiting current increased.

The cathodic polarization curves for the bath without additives and the bath with d-xylose are displayed in Figure 6.4.

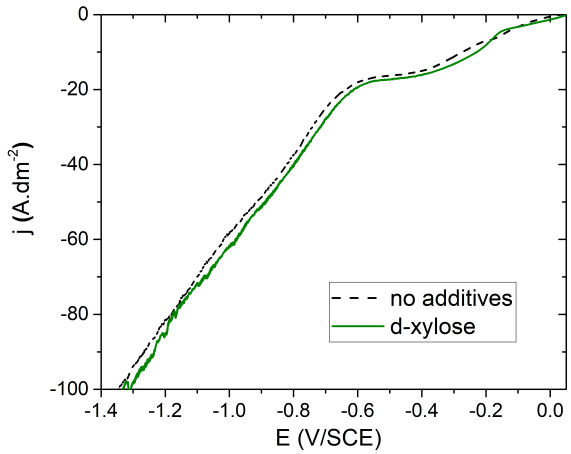

Figure 6.4. Cathodic polarization curve of $CuSO_4$ + H_2SO_4 bath without additives (dash line) and with with 33 mg/L of d-xylose (green solid line) scan rate 10 mV/s.

Curves present a very similar behavior in the presence or absence of xylose, especially under -0,3 V/ECS, where the reaction is controlled by diffusion. The zone of interest starts above 20 A dm^{-2} (-0.6 V/SCE), where the diffusional plateau ends and where a larger amount of hydrogen is produced, which is where the use of pulse sequence may be of interest to limit the competition between copper reduction and hydrogen production. It is interesting to note that, as soon as the copper reduction starts i.e. (-0.2 V/SCE), the current density is always higher in d-xylose

presence illustrating an inducing effect of copper growth.

For our study, the pulse sequences were designed to deliver rectangular cathodic pulses with an amplitude ranging from 40 A dm^{-2} to 100 A dm^{-2}, for a given cathodic time of 100 ms (T_{on}). Time off was adjusted to keep a constant average current of 2 A dm^{-2} as seen in Equation 6.5. Transient curves in response to pulsed currents were studied for various cathodic current densities. Two main patterns have been observed as shown in figure 6.5. At low current densities, i.e. below 50 A dm^{-2}, the potential increases rapidly and reaches a fairly constant value. For higher current densities, two characteristic plateaus can be observed: the first one corresponds to the faradic reduction of copper below the diffusion limit, and the second one, at higher potential, is attributed to an increase of the local resistance induced by the depletion of the copper concentration close to the interface. This situation called "diffusion-limited-range" interfere with the copper reduction, promoting competitive hydrogen production.

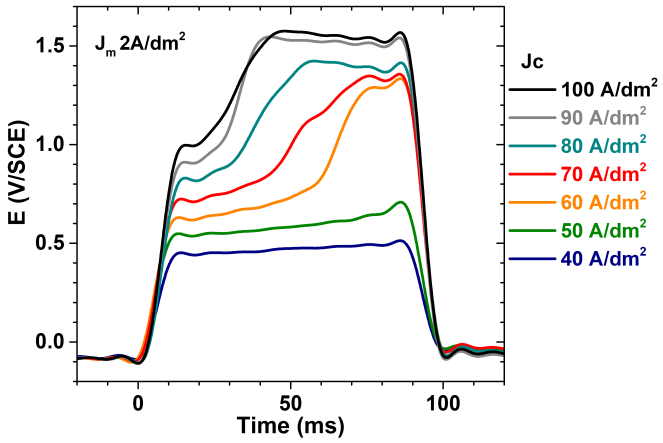

Figure 6.5. Transient curves in response of different cathodic currents (40-100 A dm^{-2}) for a fixed T_{on} of 100 ms, and constant $I_{average}$ of 2 A dm^{-2} recorded for the bath without additives.

In addition, τ values were calculated by applying Sands Equation 6.4 [129] and are displayed in Table 6.2. For our case, the $CuSO_4$ concentration is 0.46 M. For the determination of the diffusion coefficient of copper, the relationship in eq. 6.6 is used for a concentration between 0.002M<[$CuSO_4$]<1.0M [133]. For our electrolyte, this is 5.59×10^{-6} cm^2 s^{-1}.

$$10^6 \times D_{Cu} = 6.33 + 2.69log[C_{Cu}] + 1.62log^2[C_{Cu}] + 0.256log^3[C_{Cu}] \quad (6.6)$$

Table 6.2. Transition times for the single pulses.

J_c (A dm^{-2})	40	50	60	70	80	90	100
τ (ms)	217	139	96	71	54	43	35

It is interesting to note that, for the lower current densities i.e. 40 or 50 A dm^{-2}, τ values (calculated in Table 6.2) are much higher than the pulse durations. In these cases the pulse sequence could have included a longer t_{on}, without changes in potential value. The transition occurs around 60 A dm^{-2}, but the τ decrease is less and less pronounced as the current density increases as expected from the $1/Jc^2$ dependence (Eq. 6.4).

When adding 33 mg/L of d-xylose, it is possible to reach higher current densities before the occurrence of the transition between the faradic reduction of copper, near the electrode, and the diffusion-limited mechanism. The d-xylose acts by inhibiting the hydrogen production. τ values were not calculated in the case of d-xylose presence because of the uncertainty on diffusion coefficient rate in the Sands equation 6.4.

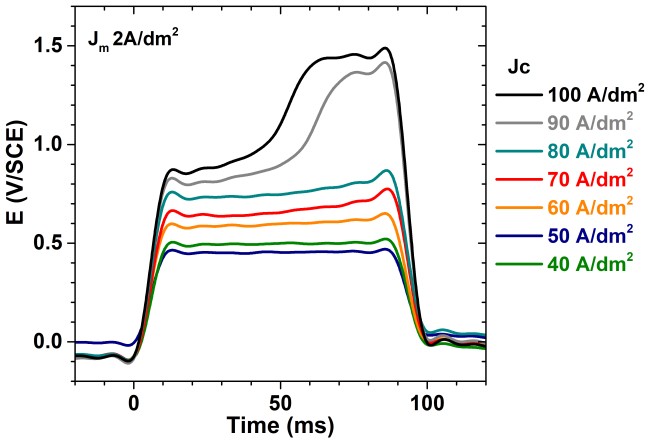

Figure 6.6. Transient curves in response of different cathodic currents (40-100 A dm^{-2}) for a fixed T_{on} of 100 ms, and constant $I_{average}$ of 2 A dm^{-2} recorded for the bath with d-xylose.

As a result of the above, four singular situations have been selected on the curves and they correspond to four pulse sequences (40 A dm^{-2}, Ton=20 ms), (40 A dm^{-2}, Ton=80 ms), (70 A dm^{-2}, Ton=20 ms), (70 A dm^{-2}, Ton=80 ms), being the last point in the diffusion limited regime for the bath without additives, and were used to prepare samples for characterization in terms of hydrogen outgassing by TDS and XRD measurements. The off-time was adjusted to keep the same constant average current of 2 A dm^{-2} and the respective values are given in Table 6.3.

Table 6.3. Pulse parameters of chosen sequences.

Current density	T_{on} (ms)	T_{off} (ms)
40 A dm^{-2}	20	380
40 A dm^{-2}	80	1520
70 A dm^{-2}	20	680
70 A dm^{-2}	80	2720

Due to very long off-times, the interface behavior in absence of current was checked. According to the performed tests, copper dissolution in the copper plating bath is negligible, because weight measurement does not show any variation even after hours of exposure. In the same manner, adsorption of d-xylose which may occur during off-times is also not related to reaction inhibition, as the corresponding polarization curves do not show an additional shift in the reduction potential. On the contrary, for the potential where copper reduction occurs, current densities in presence of xylose are always slightly higher than in absence of additive. Finally, surface tension of the electrolyte was also investigated as it was sought the possible contribution of wettability modification [65] by d-xylose in inhibiting the hydrogen to adsorb onto the growing crystals or modifying the formation of bubbles in solution. The surface tension was measured by the stalagmometric method for the two electrolytes and revealed similar value for both cases of 74.5 ±0.5 mN/m (as seen in Appendix IV).

6.4 Hydrogen desorption measurements

The samples were electroformed following the procedure described in section 6.2. TDS samples of 10 mm x 10 mm were extracted from the larger plated samples. Prior to all measurements, the samples were weighed, with an accuracy of 0.1%, in order to calculate the corresponding normalized outgassing and concentration.H_2 outgassing was measured for the different plated samples at a 10 °C min^{-1} step rate from 20 °C to 700 °C. The normalized H_2 outgassing rate (divided by each mass) is plotted as a function of heating temperature for each plating sequence and each electrolyte and the results are shown in Figures 6.7 and 6.8.

In Figures 6.7a and 6.8a, two different outgassing peaks (regions) are identified. The first peak occurs between 300 °C - 500 °C, while the second peak evolves at higher temperatures (600 °C - 700 °C). Approximately the same two peaks were found by Gubin et al. [115] (450 °C and 600 °C) on thin electroplated films of some tens of µm and as in the present case, the high energy peak was particularly marked for high currents. Fukai et al. [134, 135] also observed different outgassing peaks in their study of super vacancy hydrogen formation in copper. The super-vacancies occur in electrodeposition as M-H atoms and M-atom vacancies are deposited by atom-by-atom process [136]. The nature of the first peak can be ascribed to hydrogen diffusion from vacancies and is largely described in literature [63, 116]. Hydrogen is produced during electroplating as a side reaction and several atoms can replace the position of a copper

atom in the lattice. The second peak is not fully understood. Fukai et al. [134] suggest two different possible explanations for the high temperature peak. The first explanation is that it originates from precipitation of H from the vacancies in hydrogen bubbles that will undergo higher diffusion resistance in the copper lattice. The second explanation is that hydrogen can create super abundant vacancies with a higher number of H atoms sharing a vacancy site. Other authors [115, 137] suggest that hydrogen is stored in the material in two forms: atomic hydrogen in solid solution and molecular hydrogen in bubbles, which may be located at the grain boundaries.

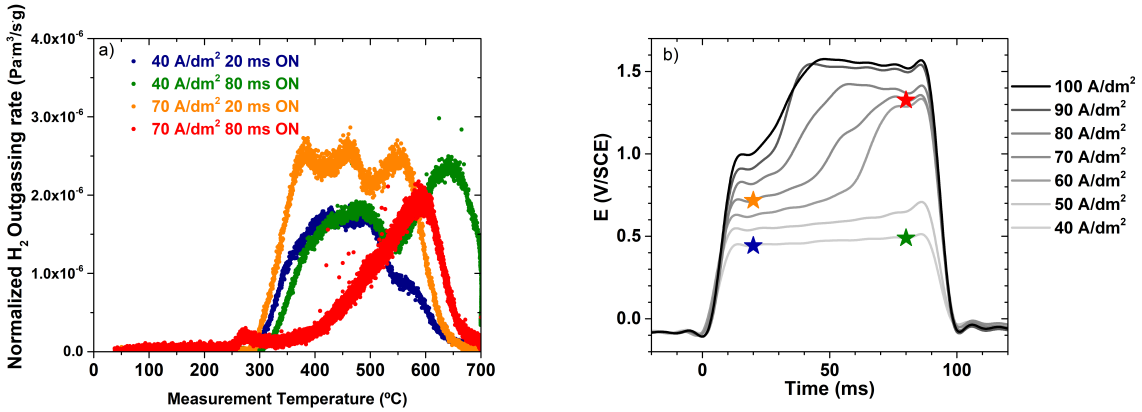

Figure 6.7. In (a) normalized H_2 outgassing rate as a function of heating temperature for the 4 different pulse sequences in the bath without additives. In (b) the four selected sequences marked with a star: 40 A dm^{-2}, 20 ms (in blue) and 80 ms (in green) cathodic time and 70 A dm^{-2}, 20 ms (in orange) and 80 ms (in red) cathodic time, with average current of 2 A dm^{-2} in all cases.

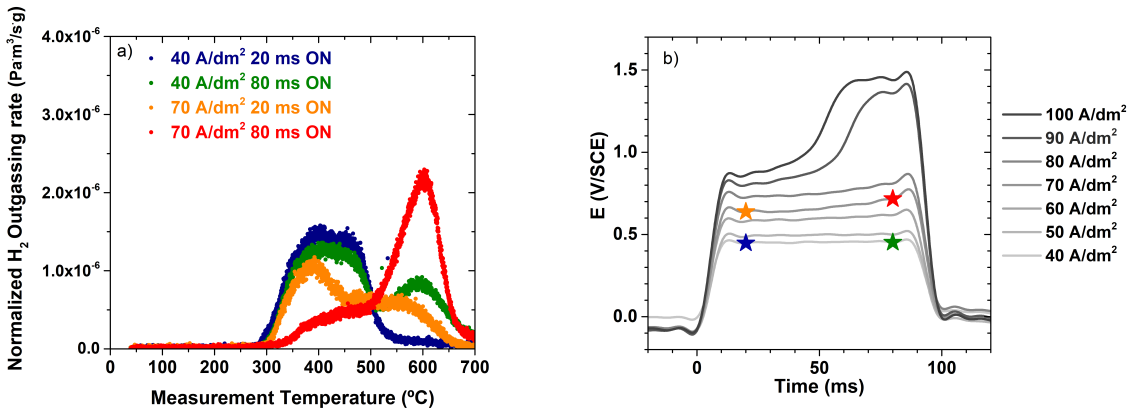

Figure 6.8. In (a) normalized H_2 outgassing rate as a function of heating temperature for the 4 different pulse sequences in the bath with d-xylose. In (b) the four selected sequences marked with a star: 40 A dm^{-2}, 20 ms (in blue) and 80 ms (in green) cathodic time and 70 A dm^{-2}, 20 ms (in orange) and 80 ms (in red) cathodic time, with average current of 2 A dm^{-2} in all cases.

For the d-xylose bath (Figure 6.8), the effect of increasing cathodic time on the outgassing trend can be followed (for 40 A dm^{-2}: 20 ms and 80 ms). For short pulses, hydrogen is mainly outgassed in the first peak (300 °C - 500 °C), while for long pulses it is additionally released around 600 °C.

For the non-additive case (Figure 6.7), the same trend is observed. Moreover, the samples that were plated at higher current and higher pulse time (in this case, the red star on Fig. 6.7b on the transient curves, represented by the red curve of outgassing rate in Fig. 6.7a), only exhibit the second peak at 600 °C and the first peak is absent.

In conclusion, the data in Figures 6.7 and 6.8 demonstrate that the pulse length influences the hydrogen trapping mode into the material. In the explored range of current density values, for both cases - with and without additive - the samples produced with pulses with longer T_{on} exhibit a larger proportion of hydrogen in the higher temperature peak of desorption (around 600 °C), compared to the samples with shorter T_{on}, where hydrogen desorbs mainly at lower temperature. As mentioned above, such two peaks were interpreted by other authors as belonging to different species of hydrogen incorporated in copper [135]. We remark that displacing the hydrogen to a state which contributes to outgassing only at very high temperature would be beneficial for electroformed vacuum chambers, which are used in a temperature range below 300 °C.

In order to compare the quantities of hydrogen released, the concentration (at. ppm) was calculated as per Equation 6.7, integrating the total amount of outgassed hydrogen, and is plotted versus the given pulse charge density per period (J_{on}x T_{on}) as seen in Figure 6.9 and Table 6.4.

$$H_2(atomic\ ppm) = \frac{mol\ H_2\ outgassed}{10^{-6}\ mol\ Cu\ total} \tag{6.7}$$

Table 6.4. Hydrogen incorporation, in atomic ppm, as measured in the TDS.

Plating parameters	Bath without additives	Bath with d-xylose
40 A dm^{-2}, T_{on}=20ms	65	42
40 A dm^{-2}, T_{on}=80ms	109	51
70 A dm^{-2}, T_{on}=20ms	101	37
70 A dm^{-2}, T_{on}=80ms	73	53

Comparing the quantitative results of hydrogen incorporation as a function of pulse charge density in the absence of additive, it can be assumed that the incorporation of hydrogen is proportionally to its generation. This is true for the following sequences (40 A dm^{-2}, T_{on}=20ms) <

(40 A dm^{-2}, T_{on}=80ms) < (70 A dm^{-2}, T_{on}=20ms). But one sequence (70 A dm^{-2}, T_{on}=80ms), does not fit into this scheme. This sequence is the single one of the test panel which presents a "diffusion-limited-range" plateau. During electroplating, strong hydrogen bubbling for this sample was noticeable, which confirmed high hydrogen generation. Outgassing results (Figure 6.7) evidenced a dominant outgassing peak at 600 °C. The high level of hydrogen generation in the case is also accompanied with a higher disturbances of the limiting diffusion zone, which will favor bubble coalescence and hydrogen removal.

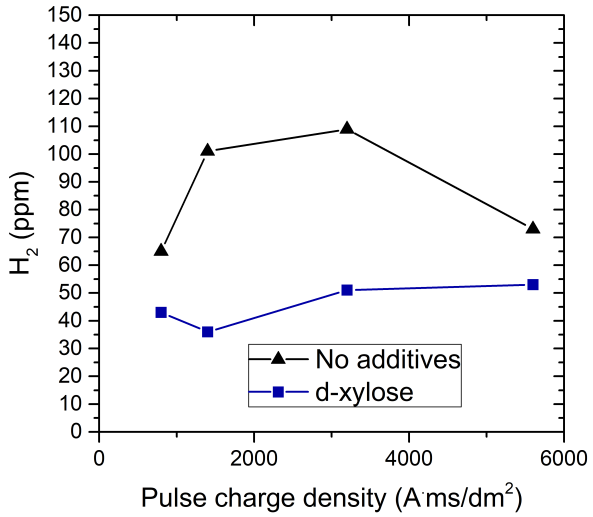

Figure 6.9. H_2 concentration (atomic ppm) as a function of pulse charge density per period (J_{on}x T_{on}). The two electrolytes are compared.

Thus, from the data in Figure 6.9 it can be concluded that the incorporation mechanism seems to play an important role in addition to the production of H in the bath. The amount of plated copper per pulse in each case (scaling from the total plated amount) can be compared with the diffusion length during the time T_{off} by using the diffusion coefficient D of H in copper at room temperature, extracted from reference [138]. The comparison is shown in table 6.5.

Table 6.5. Thickness deposited per pulse and diffusion length of H in copper during T_{off}.

Plating parameters	Thickness per pulse (nm)	D·$T_{off}^{1/2}$ (nm)
40 A dm^{-2}, T_{on}=20ms	2.4	267
40 A dm^{-2}, T_{on}=80ms	9.2	534
70 A dm^{-2}, T_{on}=20ms	2.6	357
70 A dm^{-2}, T_{on}=80ms	11.2	714

It is clear that the diffusion length is in all cases very large compared to the thickness per pulse, meaning that H dissolved in copper would have the time to move across the layer, diffuse in

and out. This phenomenon is independent of the time-off duration, because even at shorter T_{off} times, hydrogen would have already left the coating by diffusion. This would result in an equilibrium concentration of H corresponding to the solubility limit in all cases but would not explain the different amounts outgassed in TDS. Therefore, it confirms that the hydrogen is incorporated in a different state and cannot diffuse easily. All the values of concentration found in the samples are above the solubility limit [139] and this clearly demonstrate that hydrogen is incorporated in bound states in addition to the hydrogen dissolved in copper. This is consistent with the conclusions from figures 6.8 and 6.7 which indicates that the hydrogen trapping states are different for the long and short pulse times.

As a result of comparing H_2 concentration on samples from the d-xylose bath and the non-additive bath (see Figure 6.9) and table 6.4), it can be confirmed the role of d-xylose as an inhibitor for H_2 incorporation into the deposit. Indeed, all the samples without the additive show a higher hydrogen content than those with d-xylose and this is independent of the pulse parameters. The results match with previous studies conducted with d-xylose as an additive on the copper sulphate plating bath, where the same hydrogen evolution was observed at longer times [48, 62]. Other authors [62, 70] reported a H concentration of 1 wt. ppm (31 at. ppm for H_2) for a copper sulphate bath containing d-xylose as additive, and values 10 times higher for an acidic $CuSO_4$ bath without additives.

It is interesting to link the electrochemical behavior in presence of d-xylose to the reduction of hydrogen concentration into the coating. Looking closely to the outgassing rates (Figure 6.8), one can notice that for the lowest pulse charge density ($40\,A\,dm^{-2}$, T_{on}=20ms), the outgassing is restricted to the first peak, at 300 - 500 °C, ascribed to hydrogen diffusion from vacancies. Then, increasing the pulse length or the current density, the second peak at 600 °C appears and grows resulting from a second mode of hydrogen storage in super abundant vacancies or bubbles at grain boundaries, which may be considered as defects. The latests are already present in absence of d-xylose for the lowest pulse charge density and in a more significant manner for the other pulse charge densities as shown in Figure 6.7, suggesting a less efficient copper reduction. This is in agreement with the polarization curves (Figure 6.4) where the current density in presence of d-xylose is always higher. It is also in agreement with the transient curves (Figure 6.6) where the emergence of the diffusion-limited range plateau is delayed at higher current density. This confirms that copper reduction is favored due to d-xylose adsorption.

6.5 Microstructure and preferred orientation

XRD analysis was performed on twin electroformed samples in order to study the microstructure of the samples. Diffractograms were recorded at room temperature and the characteristic copper diffraction peaks corresponding to planes (111), (200), (220) and (311) were observed as shown in Figure 6.10. For these samples, we can see a difference in the relative intensities of the various

orientations. This can be quantified by calculating the relative proportion of the intensities for different crystallographic planes (h,k,l) in Equation 6.8, where I(h,k,l) are peak intensities on the diffraction patterns and $I_0(h,k,l)$ are the theoretical ones (taken from the Joint Committee on Powder Diffraction Standards (JCPDS) 070-3038 for Cu) for an isotropic sample.

$$RTC_{hkl} = \frac{I_{hkl}/I^0_{hkl}}{\sum I_{hkl}/I^0_{hkl}} \tag{6.8}$$

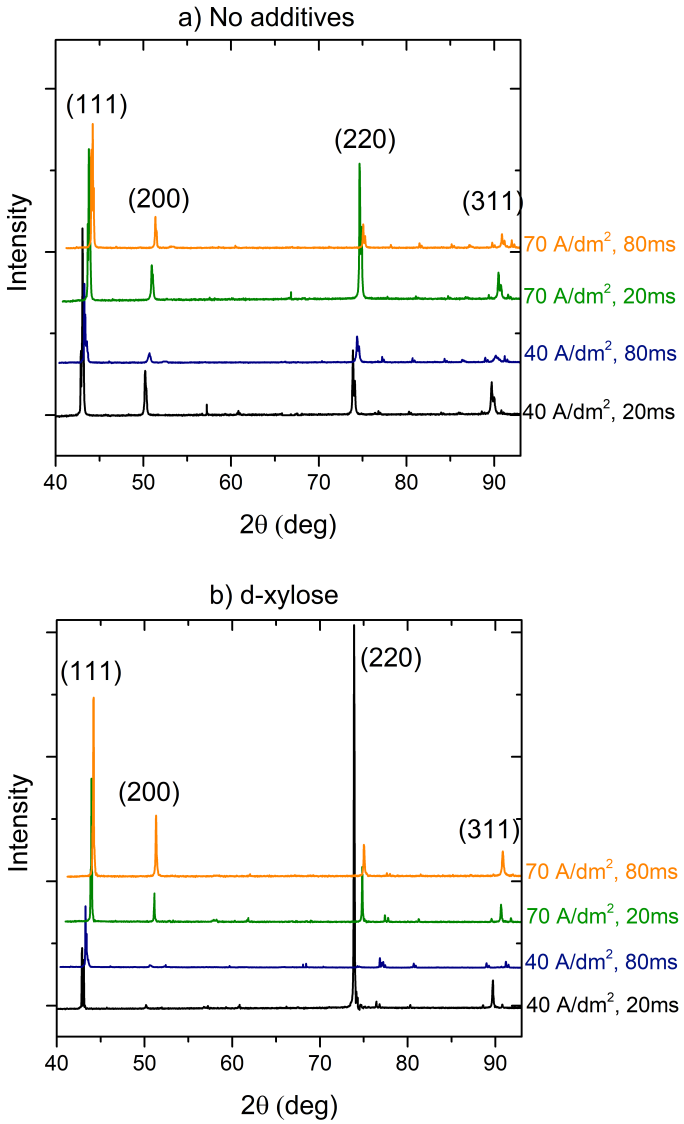

Figure 6.10. X-ray diffractograms of copper-plated samples produced at different pulse sequences for the two electrolytes (a) without additives, (b) with d-xylose at room temperature.

The relative texture coefficient (RTC) is compared for different pulse charge densities in Figure 6.11. For both baths a similar general trend is observed; the preferential orientation for (220) plane decreases while the pulse charge density increases, and nearly all samples show a similar preference for planes (200), (111) and (311) for the largest charge current density. However, the sample 40 A dm^{-2}, 20ms, of the bath without additives does not follow the trend. As the applied current density increases, the nucleation rate increases and thus the probability of grains oriented randomly in different planes [118]. Marro et al. [128] observed that an increase in pulse time is followed by a decrease in preferential orientation. They correlated this fact to the increase of residual stress in copper films.

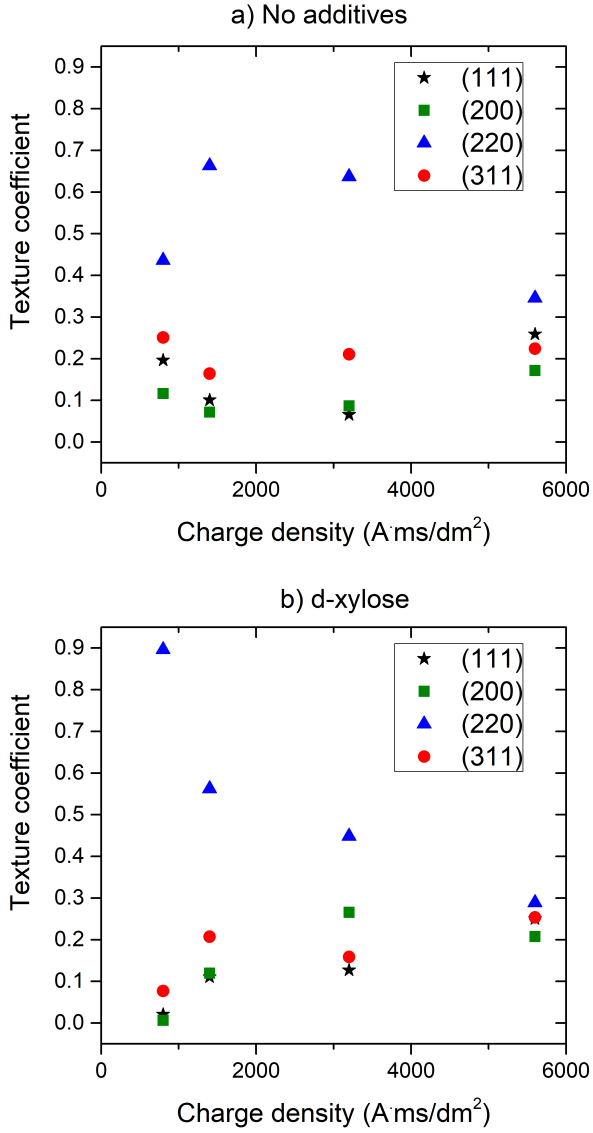

Figure 6.11. Relative texture coefficient of copper-plated samples as a function of pulse charge density per period ($J_{on}xT_{on}$). Samples from the non-additive bath (a) and d-xylose bath (b) are compared.

The lattice parameters and crystallite size was measured from the XRD results at room temperature. The crystallite size was calculated by the Scherrer equation 6.9 (already seen in Chapter 1.5).

$$w = \frac{K \cdot \lambda}{\beta cos\Theta} \tag{6.9}$$

Where w is the mean size of the ordered crystalline domain, λ is the wavelength of the X-ray source, K is a dimensionless shape factor (which has a typical value of 0.9), β is the line broadening at half of the maximum intensity, after subtracting the instrumental line broadening (in radians) and θ is the Bragg angle.

For the lattice parameter, the interplanar distances are calculated from the difraction angle of the peaks, employing the Bragg's law (Equation 6.10).

$$n\lambda = 2dsin(\Theta) \tag{6.10}$$

Where n is an integer representing the order of the diffraction peak, λ is the wavelength of the X-ray and θ is the scattering angle. From the interplanar distance d obtained above, the lattice parameter was determined. In the case of a cubic system, the following equation is applied:

$$a = \frac{d}{\sqrt{h^2 + k^2 + l^2}} \tag{6.11}$$

Where h, k, l are the Miller indices of the Bragg planes. The results of cell parameter and crystallite size at room temperature are shown in Table 6.6. The crystallite sizes are too big in order to be measured by this method. The lattice parameters are close to the one of OFE copper (3.6179 A).

In Figure 6.12, the lattice parameter is plotted vs. the heating temperature. Increasing the temperature leads to an increase of the lattice parameter of pure copper, due to thermal expansion. The simultaneous release of hydrogen during the heating, normally resulting in a contraction of the microstructure by vacancy migration or atomic positional shifts on other complex systems [140], is not sufficient to counterbalance this phenomenon and the variation of pure copper is globally positive (dots and black line on Figure 6.12, data extracted from literature [141,142]).

Table 6.6. Calculated values of the lattice parameter and crystallite size (from the XRD diffractograms at RT).

	Bath without additives		Bath with d-xylose	
Plating parameters	Lattice par. (A)	Crystallite (nm)	Lattice par. (A)	Crystallite (nm)
40 A dm^{-2}, 20 ms	3.612	>500	3.610	>500
40 A dm^{-2}, 80 ms	3.610	>500	3.608	>500
70 A dm^{-2}, 20 ms	3.611	>500	3.613	>500
70 A dm^{-2}, 80 ms	3.615	>500	3.614	>500

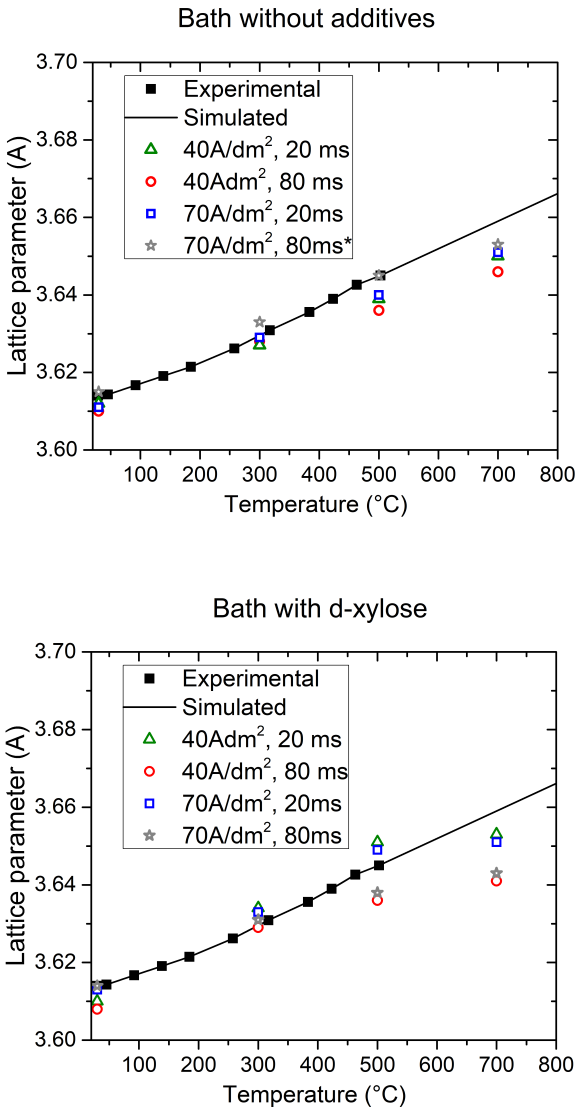

Figure 6.12. Lattice parameter evolution with increasing temperature from 20 °C to 700 °C with a 10 °C/min step for the different pulse sequences for the bath without additives (top) and with d-xylose (bottom). The data are compared with reference copper reported values [141, 142].

However, if the lattice parameter variation is consistent with the values from the literature between 25 °C and 300 °C, a difference arises above 450 °C. From there, the value of the lattice parameter stops increasing, which can be attributed to a more significant microstructure reorganization, due to H_2 vacancy diffusion. This must be seen in view of the outgassing measurement results, where two kinds of degassing peaks were reported: one centered around 400 °C and the other about 600 °C, representative of two kind of hydrogen trapping mode. The discrepancies found with the pure copper data can also be accounted for by the presence of a specific trapped hydrogen form, because it occurs above the temperature threshold. This is confirmed by the fact that longer pulses always exhibit a larger lattice parameter mismatch than shorter pulses, corresponding to the higher hydrogen outgassing level around 600 °C.

6.6 Microscopic studies

In addition, after the outgassing measurements, the samples were characterized by SEM. The different samples were imaged in the horizontal surface, which corresponds to the last plated surface. Figure 6.13 displays the SEM images of the top surface of the electroformed copper samples in the bath without additives (a) and in the bath with d-xylose (b), keeping the same average current density $2\,\mathrm{A\,dm^{-2}}$ by adjusting T_{off}. After SEM horizontal imaging the measurement of the grain size was performed after polishing and removing 10 µm of the top surface and micro-etching (according to ASTM E112) of the surface [96].

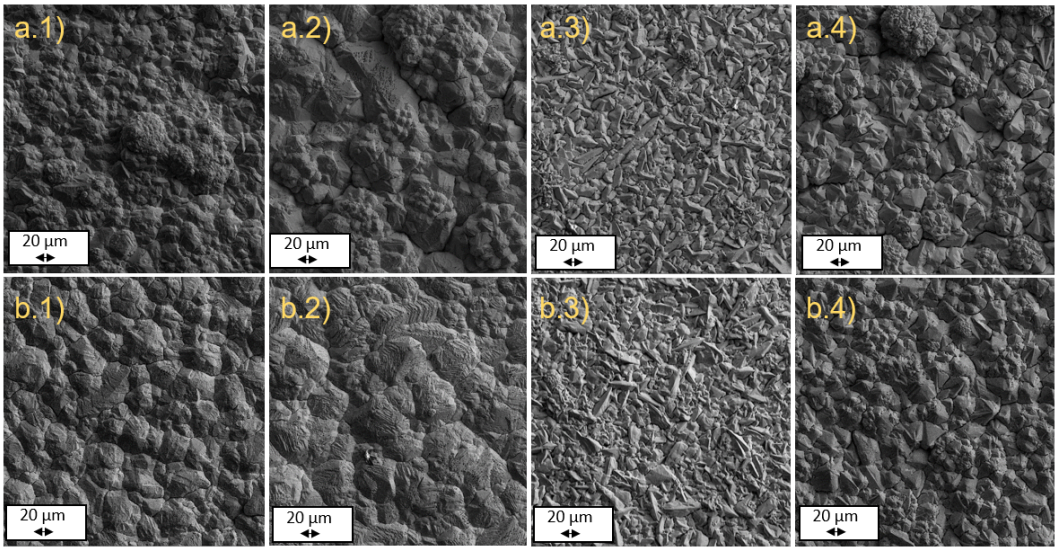

Figure 6.13. Optical microscope pictures of electroformed copper surface using different pulse sequences (1): $40\,\mathrm{A\,dm^{-2}}$, Ton=20 ms, (2): $40\,\mathrm{A\,dm^{-2}}$, Ton=80 ms, (3): $70\,\mathrm{A\,dm^{-2}}$, Ton=20 ms, (4): $70\,\mathrm{A\,dm^{-2}}$, Ton=80 ms. Average current density is kept at $2\,\mathrm{A\,dm^{-2}}$ by adjusting off-time. Samples from the non-additive bath (a) and the d-xylose bath (b) are compared.

From the SEM observations of Figure 6.13, the differences between the deposited layers from the two different electrolytes are less noticeable than those for the different pulse plating sequences. Malone et al. [48] found no changes in mechanical properties or microstructure when the only variation in the deposition conditions was the presence (or absence) of d-xylose. The most significant effect is visible when increasing the average current density from 40 to 70 A dm^{-2}.

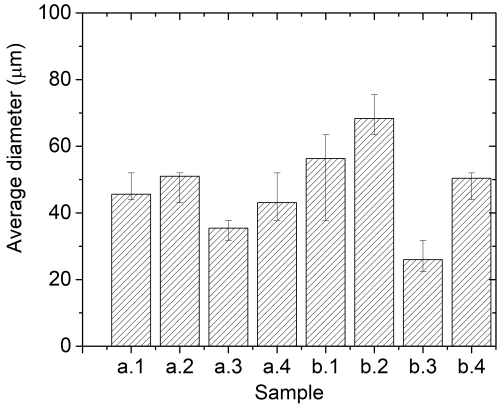

Figure 6.14. Grain size from the metallographic grain size analysis following ASTM E112 [96] (average (m) and absolute errors) for (1): 40 A dm^{-2}, Ton=20 ms, (2): 40 A dm^{-2}, Ton=80 ms, (3): 70 A dm^{-2}, Ton=20 ms, (4): 70 A dm^{-2}, Ton=80 ms. Average current density is kept at 2 A dm^{-2} by adjusting off-time. Samples from the non-additive bath (a) and the d-xylose bath (b) are compared.

The differences in grain size between both electrolytes for the same set of parameters (current density and T_{on}) are detailed in Figure 6.14. For both bath compositions, when the current density increases for a fixed T_{on} (Figures 6.13 and 6.14: the pair a1-a3 and b1-b3, for instance), the nucleation rate increases and thus does the number of grains per surface area, resulting in a smaller grain size [118]. This is explained by Ibl et al. [121] by the fact that the activation overpotential becomes larger with increasing current density, so that larger free energy is available for the formation of new nuclei. They reported similar conclusions in their study of the pulse parameters effect on the grain morphology of Cd deposits from sulphate baths. For the 40 A dm^{-2} current density, there is no significant tendency when changing the on-time. In the case of 70 A dm^{-2}, an increase in pulse time, T_{on}, leads to an increase of the average grain size (Figures 6.13 and 6.14: compare a3 with a4 and b3 with b4). This might be explained by the fact that for fixed current density a longer T_{on} enables a larger amount of material to be deposited continuously onto a grain during each pulse before adsorption of impurities during T_{off}. Such impurities might induce formation of defects setting a limit to grain growth. This effect is more marked at higher current density since more material is deposited in each pulse.

The SEM pictures also show the presence of cracks after outgassing for the higher pulse charge density (In Figure 6.13, a.4 and b.4). These samples mainly exhibited the second outgassing peak at 600 °C during heat treatment. A possible interpretation for the cracks is that they

were produced during release of hydrogen, which accumulates in bubble form on the grain boundaries [137].

6.7 Conclusions

With the view of reducing the impurities and especially the gas trapped during electroforming of thick copper layers, two parameters have been evaluated: current modulation by changing pulse duration and magnitude, and presence or absence of d-xylose.

The addition of d-xylose evidenced a big effect in the transient curves when pulses were applied. In the latter, d-xylose addition leads to higher current densities before the occurrence of the transition between the faradic reduction of copper, near the electrode and the diffusion limited mechanism. A rigorous analysis by transient curves and transition time calculations allowed us to select four different pulse current sequences, in which one is located in the diffusion limited regime.

H_2 outgassing results revealed different H-trapping states on the electroformed copper. One is ascribed to atomic hydrogen contained in copper vacancies, while the other could be interpreted by hydrogen trapped in other forms. Increasing pulse time led to the presence of a high temperature desorption peak in addition to the primary desorption peak, which is at around 400 °C. This is particularly surprising as it means that, even if no secondary plateau due to diffusion-limited range is observed, a high content of hydrogen can be trapped for longer pulse times. At the contrary, the situation expected to lead to an intense hydrogen incorporation (situation where the on-time exceeds the transition time to the diffusion limited regime) does not lead to that high content.

Addition of d-xylose reduced H_2 content in the deposit for the four pulse sequences applied. D-xylose addition led to a more strongly-oriented growth for the lower pulse charge density. The increase of the current density peak also enhanced (111) and (311) growth in detrimental of the preferred (220) growth for lower current densities.

From these results it was also evidenced that a sequence can be specifically designed in which H_2 degassing occurs only at very high temperatures. This could be convenient when applied to vacuum chamber electroforming.

The future path of chamber electroforming could include the addition of d-xylose as an additive. Nevertheless, other important factors as the maintenance of the additive in the bath must be consider before scaling-up the laboratory results. In addition the mechanical properties of the deposit were still not assessed yet.

7 Towards the real application: vacuum chambers for undulators

The transfer of technology to real scale prototypes is fundamental to prove the feasibility of this technique. Chambers up to 2 meters length where produced by using a new approach, where several mandrels (blocks) were connected together to reach the final target specification. Future developments are planned in order to assess other real chamber requirements as the use of stiffeners, thin walled chambers or cooling channels. Possible solutions for these requirements are also discussed.

7.1 Production of long chambers

The chamber production process had to be modified to achieve a final target of two meter length for the vacuum chambers. A new coating system to support the meters length mandrels should be designed based on a real application design.

To show the feasibility, a plug-in solution was developed, in which the mandrel tubes were connected one to each other as it is seen in Figure 7.1. The end of the tubes was machined accordingly to the drawing. The tubes fitted together as a female-male connector and the overall thickness was maintained.

The tubes were coated individually in the coating system, following the procedure described in Chapter 2. Firstly a NEG layer followed by a copper layer were sputtered on the aluminium mandrel. After the copper PVD coating, the tubes were connected together and attached to the prepared flanges (Chapter 2.4). In order to support the whole assembly, a special tooling was designed in PVC, as it is shown in Figure 7.2.

In addition, a plating tank was designed (3 meters depth) with copper phosphorized anodes in order to support the desired length. The length of the anodes was optimized to 2.5 m. The selected plating procedure was the DC plating with Gleam-PC, due to the best thickness distribution and mechanical performance, which would be very beneficial for these high aspect ratio chambers. Furthermore, the measured pumping performance was very similar for the two plating procedures as seen in Figure 4.29.

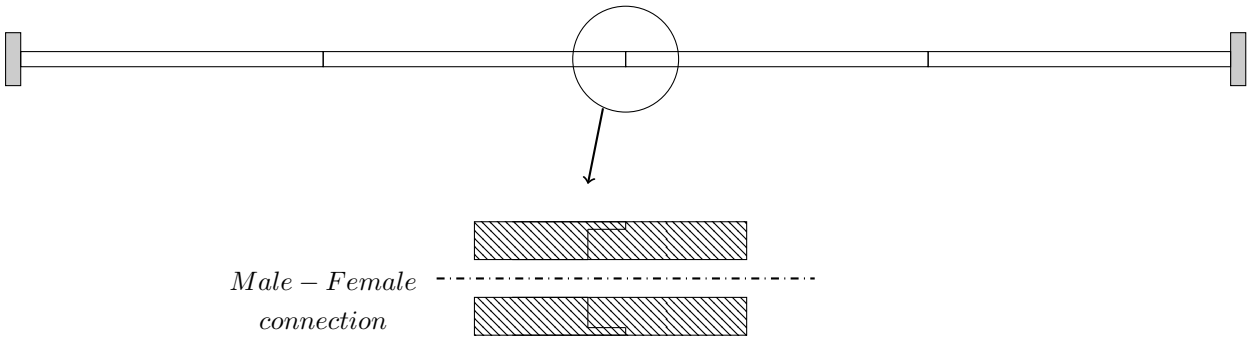

Figure 7.1. Sketch of a long chamber based on the joining of several short mandrels together.

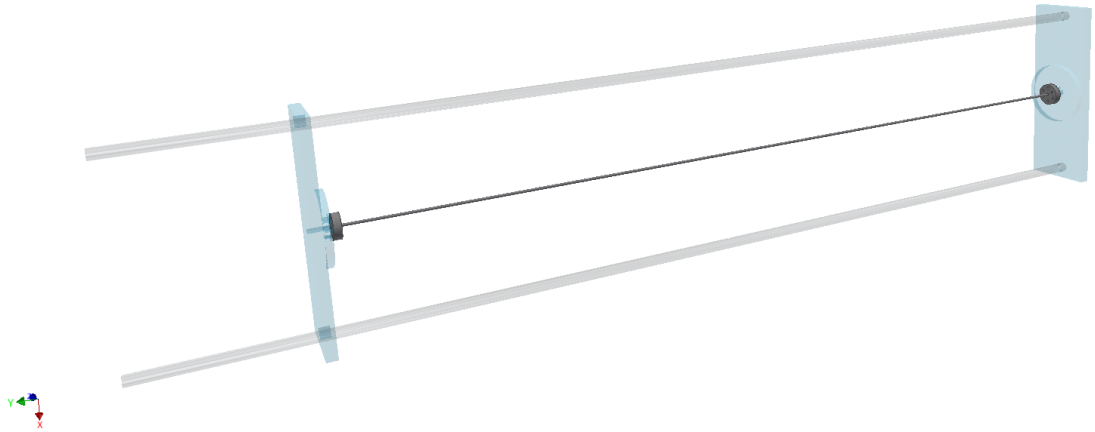

Figure 7.2. Support designed for electroforming long chambers.

All the assembly was degreased (NGL 17.40 sp ALU III, concentration: 20 g/l, temperature: 60 °C) for about 15 minutes and then activated in sulfuric acid solution (20% v). Afterwards, it was DC plated for 40 hours at $2\,\mathrm{A\,dm^{-2}}$. After the electroforming, the assembly was removed from the support and the chemical etching of the aluminium was performed by recirculating the solution inside the chamber (chapter 2.6). Finally, an acidic rinsing was performed followed by rinsing with DI water and drying. A picture of a 1.2 meters length, 5mm diameter chamber is shown in Figure 7.3. Chambers up to 2 m length were produced with this method (Figure 7.5).

7.2 Characterization of NEG coating

The TiZrV composition and thickness was measured along the length of the mandrels. Figure 7.4 presents the XRF thickness and TiZrV composition profile (at %). The thickness is $1 \pm 0.2\,\mu\mathrm{m}$ along the length of the chamber.

Figure 7.3. 5mm diameter, 1.2 meters length, NEG coated chamber.

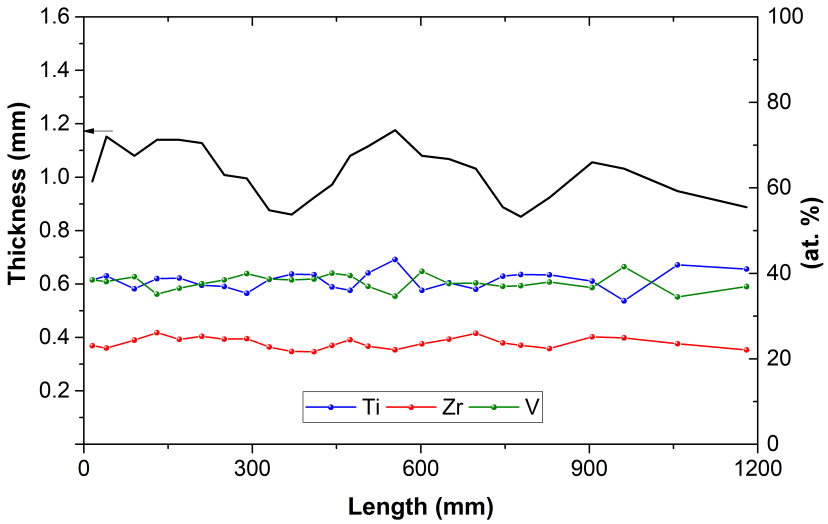

Figure 7.4. TiZrV thickness and at.% composition for the 5mm diameter, 1.2 meters length, NEG coated chamber.

In addition, the characterization of the mandrels used for the assembly of the 2 meters length, 4mm diameter NEG coated chamber, was performed. The atomic composition of TiZrV is kept constant along the chamber and the thickness varies between $1.1 \pm 0.2\,\mu m$.

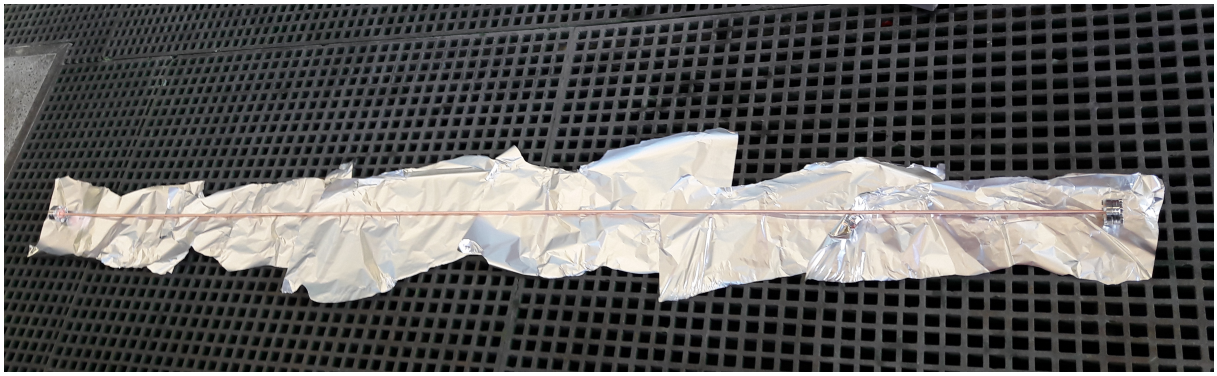

Figure 7.5. 4mm diameter, 2 meters length, NEG coated chamber.

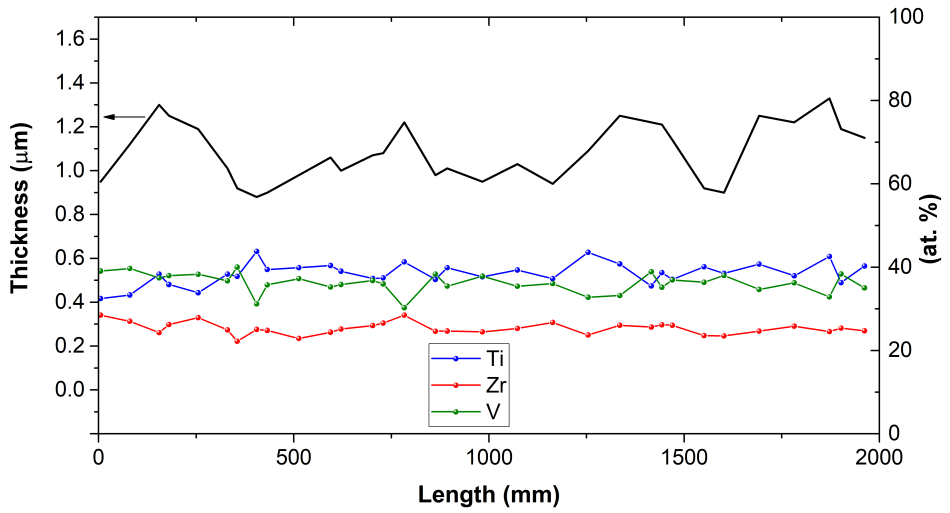

Figure 7.6. TiZrV thickness and at.% composition for the 4mm diameter, 2 meters length, NEG coated chamber.

The chambers were leak tight to $1 \times 10^{-10}\,mbar\,l\,s^{-1}$ after pump-down and bake-out procedures. The measurement of the sticking factor was not possible, due to the very high aspect ratio of the chambers (500-1000). In Figure 4.27 for the mentioned aspect ratio, the pressure ratio reaches a plateau (10^5, for P_1/P_2) and it will be necessary to inject 10^6 times the base pressure, reaching pressures above the molecular gas regime. The performance of such a device should be verified in real operation.

7.3 Undulator requirements

Some known requirements derived from future projects for accelerators are discussed in the following. To cope with assembling and handling during operation and maintenance, stiffeners should be integrated in the chamber manufacturing. In example [143, 144], for the new undulator chamber for Athos (PSI, Villingen), an ultra-thin copper vacuum chamber supported with a stiffener will be used. The chamber should be made in a one-step galvanic process (as is shown in Figures 7.7 and 7.8), with the assembly of the stiffener to the chamber by electroforming.

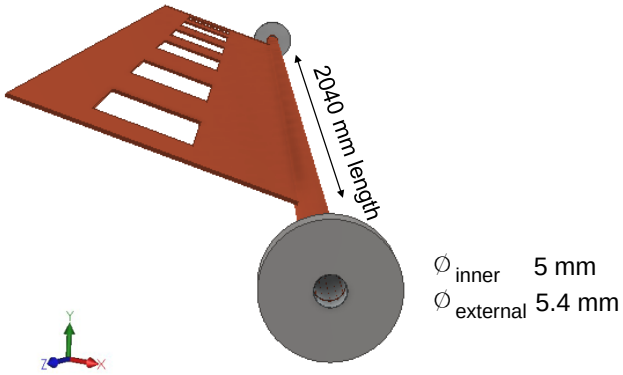

Figure 7.7. Electroformed vacuum chamber dimensions for Athos. Concept drawing.

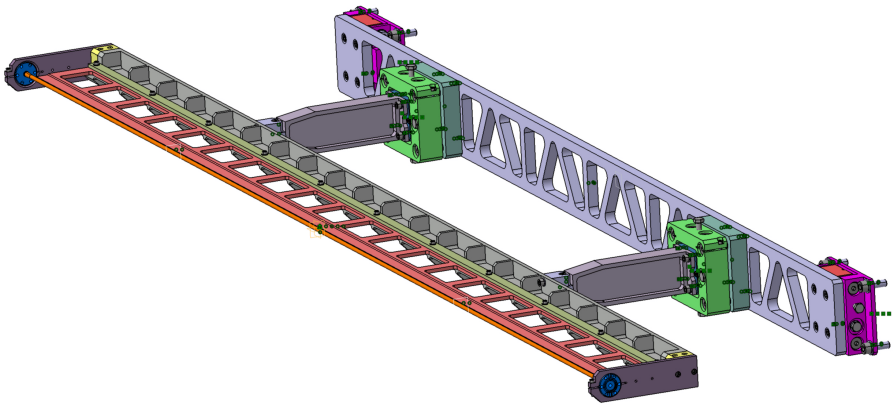

Figure 7.8. Stiffener addition by electroforming proposed by PSI [145].

In addition, the new upgrade of the ALS-U vacuum chambers [33, 146] proposed a 4mm diameter design, 2 meter length, with integrated cooling channels to cope with synchrotron light impinging on the wall (Figure 7.9 is a concept). To cope with these requirements, the future steps should also include the cooling channels in the galvanic process.

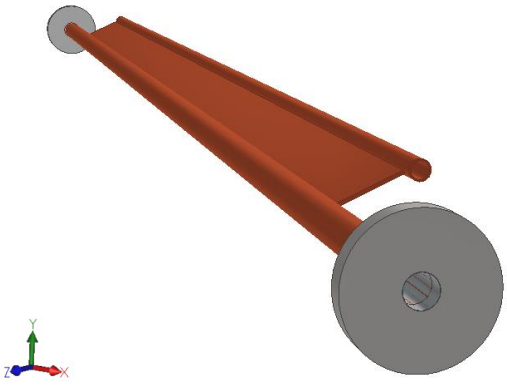

Figure 7.9. Cooling channels on the electroformed chamber. Concept drawing.

Finally for the requirements of CLIC [34, 147], the pressure in the vacuum chamber of the main beam quadrupole has a vacuum specification of 1×10^{-9} mbar. The diameter of this chamber should be designed according to the aperture of the poles of the magnet, which is 10 mm diameter for a two meters long length. The vacuum chamber walls must be the thinnest possible, in order to prevent the decrease of vacuum conductance. Thin walls of 0.3 mm thickness are proposed for this development. In addition, the heating load to the magnets should be minimized.

There are two possibilities to activate the NEG by heating the chambers in the magnets with the tight design mentioned above. First, in-situ heating can be performed, but is limited due to the risk of thermal damage of the magnet coils and poles. Second, the chamber is extracted from the magnet, which has been designed in two halfs to allow the opening, and undergoes an ex-situ activation (outside the magnet). For the first case, low activation temperatures are necessary (200 - 230 °C) in order to comply with the temperature limits imposed by the assembly. For the latter, the chamber could be heated up to the desired temperature (i.e. 280 °C) if the mechanical performance of this copper pipe remains sufficient. Such a solution has been already adopted by the achromats of MAX IV [39].

Conclusions

TiZrV thin film coatings are used in particle accelerators and synchrotron light sources to maintain ultra-high vacuum conditions. They transform the outgassing inner walls of the vacuum chambers from a gas source into a chemical pump. In addition, NEG coatings reduce the particle induced degassing, the secondary electron yield, and simplify the vacuum chamber design.

This thesis has demonstrated the feasibility of the production of small diameter vacuum chambers with a functional NEG coating through a scheme of inverted NEG manufacturing. This new scheme consists in the production of the vacuum chamber by copper electroforming on an aluminum mandrel, which has been pre-coated with a getter thin film. The stainless steel flanges are integrated in the copper chamber directly during the electroplating step.

Chambers of this type were elaborated up to 2 meters long for a range of diameters, which spans from 3 mm to 16 mm. To built the longest chambers, a dedicated strategy was developed based on joining several mandrels segments. This approach can be extended to longer chambers or various pipe shapes, and is limited only by the depth of the available copper plating tank.

The different aspects regarding the performance of the vacuum chamber with the inverted NEG were evaluated.

- The mechanical performance of the assembly (yield strength and hardness) show results close to copper OFE reference values. The DC electroformed copper in presence of the brightener is stronger than the pulse plated one without additives. Furthermore, the junction of the flange to the tube was stronger than the copper properties itself. It was also observed that the vacuum chambers were leak-tight up to the rupture.

- The NEG coating is adherent and exhibits an uniform thickness and composition along the length of the chamber. Coatings exhibit impurity-free surfaces at the level of sensitivity of XPS, and nanocrystalline structures with grain sizes lower than 3nm, as demonstrated by XRD.

- The coating is functional but requested a higher temperature for activation. At activation temperatures higher than 250 °C, the sticking coefficient for H_2 reaches 5×10^{-3} and the surface saturates after 5×10^{14} CO molecules/cm^2. A standard NEG coating (with the standard sputtering technique) reaches those values after an activation at 200 °C for 24 hours. In the reverse NEG, activation at 230 °C exhibits a lower sticking for H_2 between 1 - 2 $\times 10^{-3}$ and a saturation of 1×10^{14} CO molecules/cm^2.

The delayed activation is tentatively explained by the higher level of impurities reaching the getter film compared to the standard coating case. We have investigated several impurity sources during the production process. H and O are bulk impurities of the TiZrV layer which reduce the available sites for pumping.

The impurities may come from:

- Residual gas from the sputtering system which is adsorbed/absorbed during the coating process.
- Diffusion of impurities from electroformed copper and from the copper/film interface during thermal activation.
- Impurities adsorbed by the getter film during wet etching of the mandrel.

More in detail, measurements of oxygen concentration in the depth of the TiZrV coating by XPS depth profiling of the inverted coating found that oxygen is trapped in the getter during the sputtering process (from the residual gas of the sputtering system). Moreover, it is also incorporated from the electroformed copper during the NEG activation procedure. The TiZrV coatings ageing occurs when the content of oxygen in the bulk of the coating increases. At low activation temperatures (below 250 °C), the sticking factor decreases as the inverse of the number of activation cycles. If we assume that between 1 -2 $\times 10^{16}$ atoms/cm^2 diffuse into the bulk in every cycle, our reverse NEG sample behaves as a 4-5 cycles aged standard TiZrV coating. This is supported by the fact that an increase in the activation temperature (above 250 °C) recovers the optimum pumping speed.

TDS measurements show that hydrogen is the main impurity in the electroformed copper and could contribute to the delay of the activation of the NEG. Measurements at CERN evidenced a decrease in the H_2 pumping speed for a TiZrV film which was saturated with hydrogen. The results also showed that the H_2 saturation does not affect the CO pumping capacity and lowers the H_2 pumping speed by only half of its value.

One possible optimization route to reduce the activation delay consists of decreasing the quantity of impurities (both O and H) in the electroformed layer. A new electrolyte, which in literature evidenced very pure deposits, was tested. All electroformed samples from the mentioned bath exhibited lower H_2 concentrations in the layer. However, more work is needed in order to transfer the process from the lab to the workshop.

During this PhD thesis a 2m length, 4mm diameter NEG coated chamber was successfully produced. At present no other method exists to integrate the NEG coating in such a shape.

Future work

The feasibility of production of long NEG-coated vacuum chambers with small diameters is demonstrated. However, a better characterization of these chambers is still necessary. For instance, in terms of ageing as a function of venting/activation cycles.

In order to produce a chamber, which is fully equipped for insertion in an accelerator, the future steps involving the chamber manufacturing are the following:

- The production of chambers with thinner walls in order to minimize the aperture of the magnet poles.
- The inclusion of a stiffener to make the chamber less fragile.
- The inclusion of cooling channels in order to cope with the synchrotron radiation on the walls.

The general optimization path for the TiZrV film is to decrease the quantity of impurities at the coating and electroforming steps. For the former, a new coating system which allows the integration of a 2 meter mandrel and enables a full bake-out procedure of its components must be designed. Future work should also center in the optimization of the current electroforming procedures in the workshop. New additives and new pulse sequences can be tested in order to further optimize the purity of the electroformed layer. In particular, d-xylose addition will be evaluated when used in big components in the workshop. Furthermore, reverse pulse plating could be a promising technique and must be investigated.

Apart from cylindrical shapes, in the search for new application fields, the development of copper substrates for Superconducting radiofrequency (SRF) cavities will also be explored. It was found in this research that the PVD coating resembles the mandrel topography. Therefore, it is plausible to obtain very smooth copper electroformed layers, when the copper PVD coating is applied to a very smooth mandrel surface. The absence of welds in the process further simplifies the production of elliptical cavities, and will avoid to create porosities and surface defects in the functionally relevant areas.

Finally, another application will be to apply the reverse electroforming process for other functional thin films on complex geometries: e.g. carbon coatings, which create low SEY surfaces, or niobium coatings, which provide super-conducting properties.

Appendix

Appendix I: Pourbaix diagrams

The oxidation-reduction behavior of a given metal in an aqueous solution is not dominated by a single process and usually involves multiple pH dependent half-reactions. Furthermore, hydroxides and solid oxides may also be present and could complicate the overall chemistry by associated homogeneous and heterogeneous equilibrium. A method to summarize the oxidation-reduction chemistry is the Pourbaix diagram, which includes all important half-reactions of a given metal.

The Pourbaix diagrams of titanium, zirconium, vanadium and aluminium [148] are represented below.

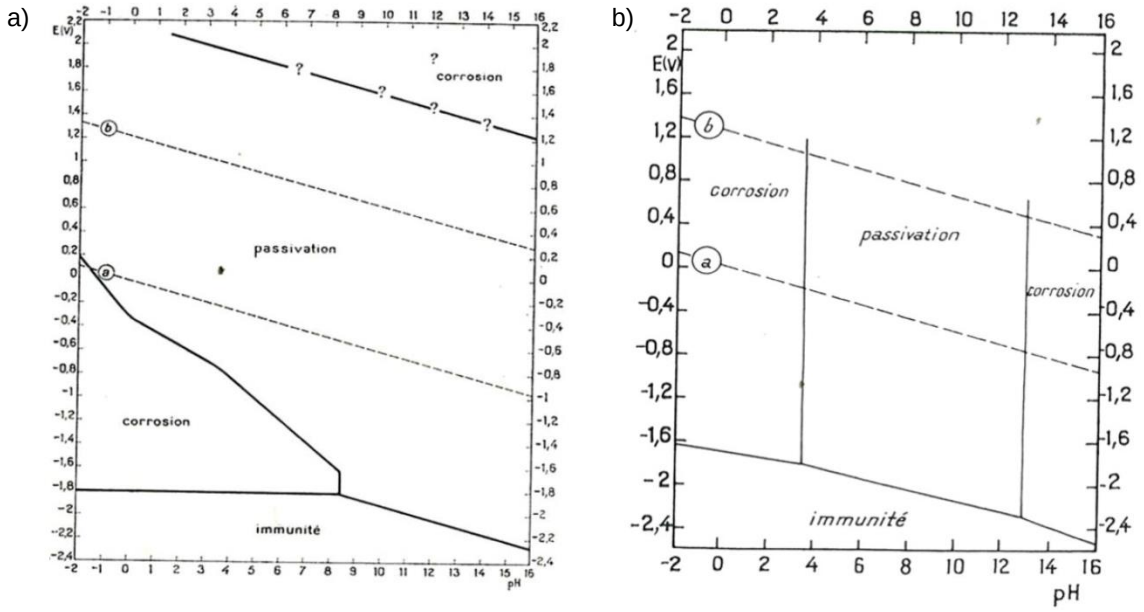

Figure 7.10. Pourbaix diagram for (a) Ti and (b) Zr [148].

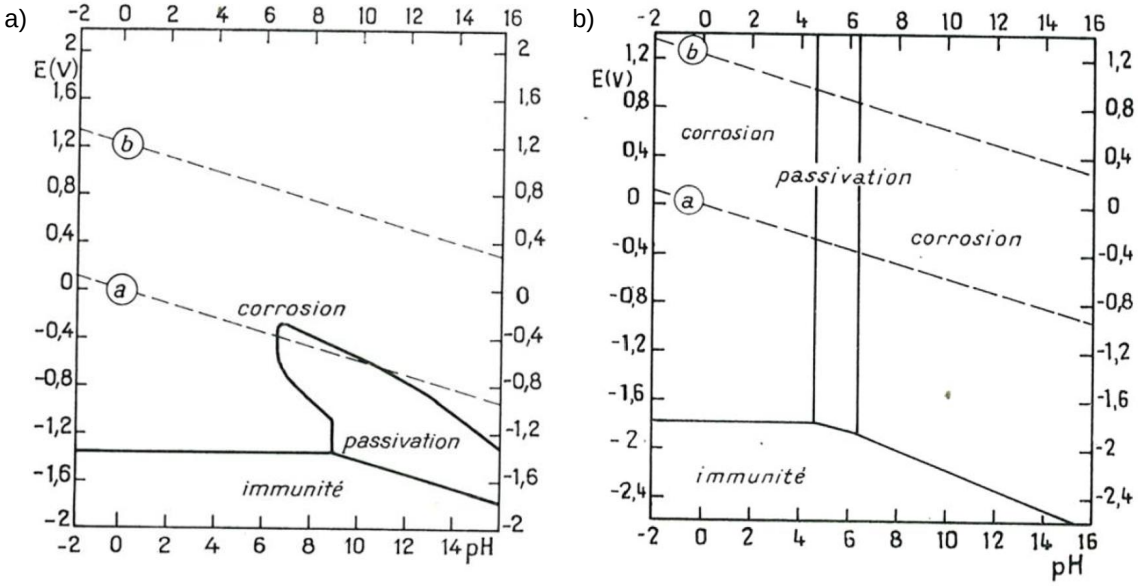

Figure 7.11. Pourbaix diagram for (a) V and (b) Al [148].

Appendix II: CO saturation measurement comparison

The standard CO saturation measurement is done in a Fisher-Mommsen system [106] provided with a calibrated conductance, which is used to calculate the pumping speed at the aperture of the chamber to be measured. When the transmission method is used, the CO pumping speed at the aperture is calculated with the sticking factor for each time interval. The two methods are described and are compared in two twin samples.

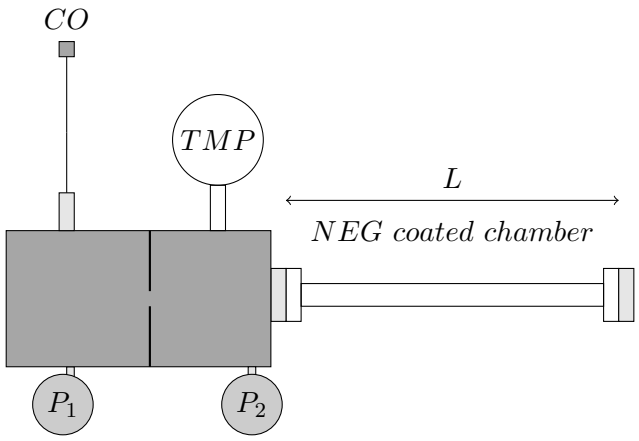

Figure 7.12. Schematic representation of the Fisher-Mommsen dome with the getter coated chamber connected to it. The system is provided by two chambers separated by a conductance, two Bayard-Alpert gauges (P1 and P2), a pumping group composed by a turbo molecular pump (TMP) and a primary pump and an injection line for the different gases.

A schematic of the Fisher-Mommsen dome can be observed in Figure 7.12. The flux of a gas is measured by recording the pressure drop across a known conductance that separates the two chambers. The geometrical shape of the dome is designed to represent a spherical system having a perfect Maxwellian distribution of gas molecule velocities [24]. The right chamber is pumped by both the NEG and the turbomolecular pump (8 l/s for CO). The conductance that separates the two chambers has an aperture of $0.78\,\mathrm{cm}^2$. Pressure measurements are performed by means of two Bayard-Alpert gauges (P_1 and P_2). They are calibrated in-situ by comparing their values to a previously calibrated gauge.

In steady state conditions, the pump throughput is equal to the injected flux of gas (F_{CO}, torr $\mathrm{l\,s^{-1}}$), which can be expressed as:

$$\begin{aligned} F_{CO} &= C_{CO}(P_1 - P_2) \\ F_{CO} &= (S_{CO}^{NEG} + S_{CO}^{turbo}) \cdot P_2 \end{aligned} \tag{7.1}$$

Where P_2 and P_1 are the pressures during injection in chamber 1 and 2 respectively, S_{CO}^{NEG} is the pumping speed of CO at the aperture of the NEG chamber, S_{CO}^{turbo} is the CO pumping speed of the TMP and C_{CO} is the conductance inside the Fisher-Mommsen dome, which is known for CO (at 20 °C):

$$C_{CO} = 3.64\sqrt{\frac{T}{M}} \cdot Area_{orifice} = 11.9(\mathrm{l\,s^{-1}\,cm^{-2}}) \cdot Area_{orifice}(cm^2) \tag{7.2}$$

Therefore, the pumping speed S_{CO}^{NEG} at the entrance can be calculated with the pressure variation during injection (as the pumping speed for the TMP is known):

$$S_{CO}^{NEG} = C_{CO}(\frac{P_1}{P_2} - 1) - S_{CO}^{turbo} \tag{7.3}$$

Furthermore, the pumping speed (S_{CO}^{NEG}) can be evaluated as a function of the quantity of gas adsorbed (Q_{CO}). The measurement consists in the recording of the pumping while the injection flux is maintained constant. The quantity of gas that had been pumped is obtained by integrating the pumping flux with time (expressed in torr l):

$$Q_{CO} = \int_0^t S_{CO}^{NEG} \cdot P_2 \cdot dt \tag{7.4}$$

Where S_{CO}^{NEG} is the pumping speed of CO at the aperture and P_2 is the pressure at the entrance.

In the case of the transmission system (Figure 4.23), the pumping at the aperture is calculated with the capture factor (β) which is obtained from each sticking factor for every given time (dt). For this, a Molflow + simulation is used to obtain the relation between the sticking factor and the capture factor (see Figure 7.13). Then, the pumping speed of CO at the aperture can be expressed as:

$$S_{CO}^{NEG} = \beta \cdot S_{CO}^{max} \tag{7.5}$$

Where S_{CO}^{max} is calculated assuming sticking factor = 1 and is defined by the conductance of the chamber (eq. 7.2). The quantity of gas that has been pumped can be then calculated as:

$$Q_{CO} = \int_0^t \beta \cdot S_{CO}^{max} \cdot P_{entrance} \cdot dt \tag{7.6}$$

Where $P_{entrance}$ is the pressure at the entrance of the chamber (P_1 in Figure 4.23).

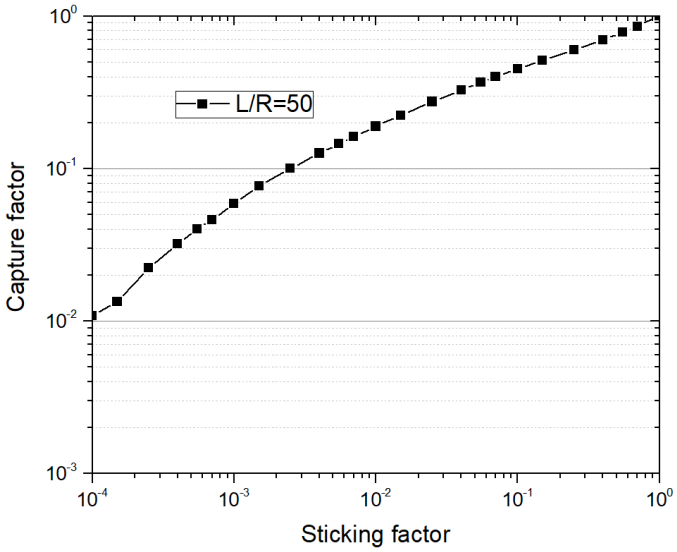

Figure 7.13. Sticking coefficient against capture factor for a L/R=50 aspect ratio chamber. Results from Molflow+ simulation.

The maximum number of CO molecules adsorbed on the surface was measured for two twin 16 mm diameter chambers (mandrel AW-6060, 1.5mm thickness) by applying both measurement procedures: Fisher-Mommsen and Transmission (equation 7.4 and 7.6) after 24 hours activation at 250 °C and 280 °C. The results (Table 7.1) show a good agreement between both measurements.

Table 7.1. CO saturation of 16mm diameter vacuum chamber (aluminium 6060, 1.5 mm thickness) after 24 hours heating in vacuum measured on the Fisher-Mommsen dome and in the transmission system after gauge calibration.

CO molecules cm^{-2}	250 °C (24 hours)	280 °C (24 hours)
Fisher-Mommsen	4.5×10^{14}	7.2×10^{14}
Transmission	5.1×10^{14}	8.3×10^{14}

Appendix III: Thermal desorption spectroscopy

The thermal desorption spectroscopy analysis was performed on a TDS system from Hiden Analytical [149]. A schematic representation of the system in detailed in Figure 7.14. The UHV system consists of a vacuum chamber and a pumping system. The pumping system is made of a turbo-molecular pump backed by a primary rotary vane pump. The UHV conditions are necessary to increase the molecular mean free path and enable the contaminants to reach the detector. The UHV conditions allows also to detect very small desorption rates. Thus, the pressure of the chamber can be considered proportional to the desorption rate of the sample.

A residual gas analysis (RGA) is placed on top of the sample and measures the intensity of the different gases, which are outgassed, as a function of time. The mass spectrometer is calibrated for the different gases of interest. The absolute amounts are within a factor of 2 in accuracy. The relative errors are given by bars in the different plots.

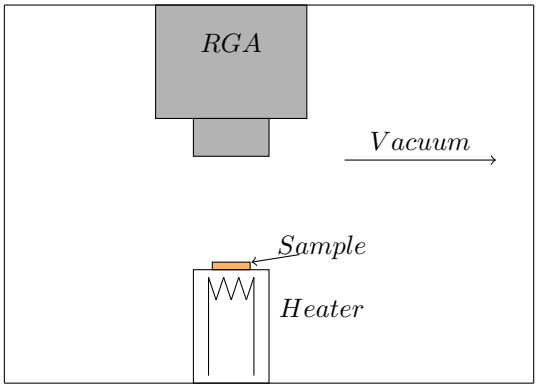

Figure 7.14. Thermal desorption spectroscopy system layout: UHV chamber with heater and mass spectrometer.

The temperature is measured close to the sample through a thermocouple, which is situated at the heater. The temperature limits of the system are 25 °C up to 940 °C. Even though the upper limit is never reached for the copper samples because at 940 °C, evaporation is high enough to cause possible damage at the system. The upper limit for copper measurement used in this system is 700 °C, since the Cu vapour pressure is 10^{-8} mbar at 990 K (717 °C) and 10^{-7} mbar at 1050 K (777 °C) [150]. It can be considered that for 10^{-8} mbar pressure, one mono-layer is deposited in 100 s, which is considered safe enough for the system.

Appendix IV: Measurement of the surface tension with the stalagmometric method

The surface tension of the baths was measured with the stalagmometric method. This method uses a well-defined volume (a calibrated bulb glass or syringe) which ends in a capillary as seen in Figure 7.15. The measurement follows the formation of droplets, which flow freely from the capillary and their weight is dependent on the surface tension of the liquid.

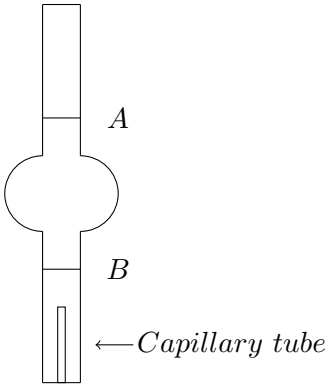

Figure 7.15. Stalagmometric instrument.

The weight of a single drop (Q) can be determined by dividing the weight of the liquid contained in the volume (V, between A and B notations) by the number of formed droplets (n):

$$Q = \frac{\rho \cdot V \cdot g}{n} \tag{7.7}$$

Where ρ is the density of the liquid and g is the acceleration due to gravity. Assuming that when a drop separates from the capillary, the value of the force and the weight is equal, the surface tension σ can be calculated as:

$$\sigma = \frac{\rho \cdot V \cdot g}{2 \cdot \pi \cdot r \cdot n} \tag{7.8}$$

Where r is the radius of the throat of drop at the moment of detachment.

If we calculate the relative surface tension compared to a standard liquid (i.e. deionized water), the formulas can simplify in:

$$\sigma = \frac{\rho \cdot n_o \cdot \sigma_o}{\rho_o \cdot n} \tag{7.9}$$

Where: n_o is the number of drops of the standard liquid, n is the number of drops of the test liquid, ρ_o is the density of the standard liquid, ρ is the density of the test liquid.

Prior to electrolyte characterisation, deionized water was tested in the same instrument at constant ambient conditions. The results for the different electrolytes are shown in Table 7.2. The addition of d-xylose does not change the surface tension of the solution, whereas the addition of Gleam-PC decreases the surface tension to 61.8 mN/m [65].

Table 7.2. Surface tension measured with Stalagmometric method.

Solution	Surface tension (mN/m)
Bath without additives	74.5 ± 0.4
Bath with d-xylose	74.6 ± 0.5
Bath with Gleam-PC	61.8 ± 0.3

Appendix V: TiZrV depth profile analysis by GDOES

Glow discharge optical emission spectroscopy analysis (GDOES) can be used to obtain the concentration depth profile of the coating. The method obtains the depth profiles by measuring the constituent elements as a function of the sputtering time. Firstly, the chamber is pumped down to 10^{-4} mbar and argon is injected and is ionized to Ar^{+} by applying a voltage between the anode and the sample which is polarized negatively. Afterwards, the sputtering process begins in which the sample's surface is bombarded by the argon ions. The ejected atoms, which are excited by the ions or electrons of the plasma, return to the non-excited state by releasing photons with a particular wavelength. The characteristic elements are interpreted thanks to the specific signals carried by the photons. In this case, the equipment used is a GD Profiler from HORIBA Jobin Yvon.

The results for a Ti bulk sample and a reference NEG coating in OFE are shown in Figure 7.16. The chamber does not work in UHV, and this affects the measurement since the material is reactive to the residual vacuum. A concentration of 5 at.% of oxygen was found in the Ti bulk, which is the quantity that is pumped by Ti from the residual vacuum. We see the same behavior with the NEG sample since a bulk concentration of 10 at.% is measured.

Therefore, this method is unable to accurately measure bulk impurities in the getter.

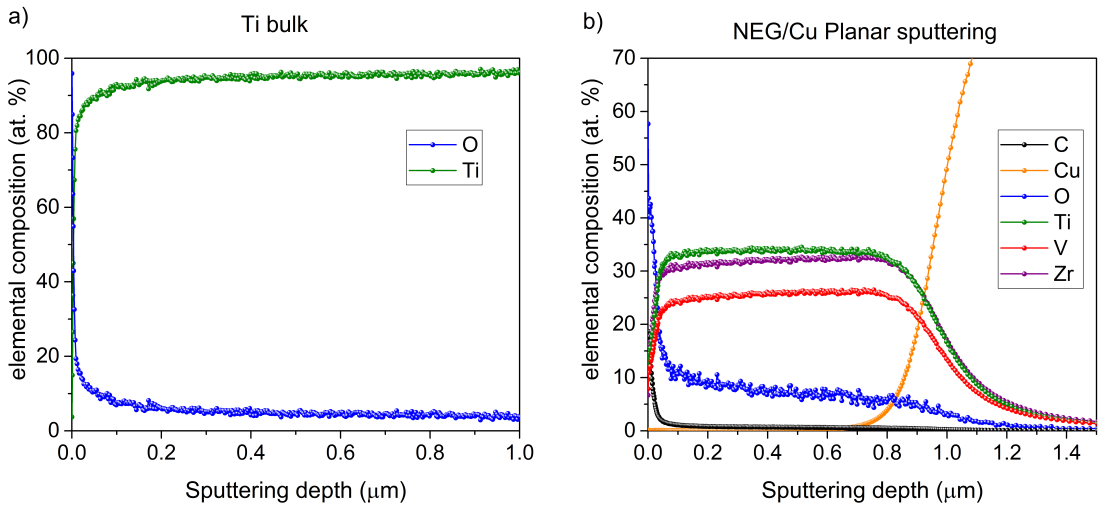

Figure 7.16. GDOES results from the (a) Ti bulk sample and (b) TiZrV coating on copper OFE.

References

[1] G. K. ONeill, "Storage rings for electrons and protons," *Phys. Rev.*, vol. 102, no. 590, 1959.

[2] G. K. ONeill and E. J. Woods, "Intersecting-beam systems with storage rings," *Phys. Rev.*, vol. 115, no. 659, 1959.

[3] K. Johnsen, "CERN intersecting storage rings," *CERN courier*, vol. 8, no. 11, pp. 263–266, 1968.

[4] H. Schopper, *LEP, The lord of the collider Rings at CERN 1980-2000.* Springer, 2009.

[5] C. Benvenuti, "A new pumping approach for the large electron positron collider (LEP)," *Nuclear Instruments and Methods in Physics Research*, vol. 205, no. 3, pp. 391 – 401, 1983.

[6] LEP vacuum group, "LEP vacuum system: present status," *Vacuum*, vol. 41, no. 7, pp. 1882 – 1886, 1990.

[7] O. Grobner, "Experience from the LEP vacuum system," tech. rep., CERN, LHC-VAC, Mar. 2001.

[8] N. S. Harris, *Modern Vacuum Practice.* McGraw-Hill, 2005.

[9] J. Lafferty, *Foundations of Vacuum Science and Technology.* Wiley, 1998.

[10] C. Benvenuti, "Molecular surface pumping: The getter pumps," *CAS - CERN Accelerator School and ALBA Synchrotron Light Facility : Course on Vacuum in Accelerators*, p. 8 p, 2007.

[11] C. Benvenuti, "Pumping device by non-vaporisable getter and method for using this getter," Dec. 24 1997. WO Patent App. PCT/EP1997/003,180.

[12] C. Benvenuti, "Extreme high vacuum technology for particle accelerators," in *Proceedings of PAC*, (Chicago, USA), p. 602, 2001.

[13] C. Benvenuti, P. Chiggiato, A. Mongelluzzo, A. Prodromides, V. Ruzinov, C. Scheuerlein, M. Taborelli, and F. Lvy, "Influence of the elemental composition and crystal structure on the vacuum properties of TiZrV nonevaporable getter films," *J. Vac. Sci. Technol., A*, vol. 19, no. 6, p. 2925, 2001.

[14] C. Benvenuti, P. Chiggiato, F. Cicoira, and Y. LAminot, "Nonevaporable getter films for ultrahigh vacuum applications," *J. Vac. Sci. Technol., A*, vol. 16, p. 148, 1998.

[15] C. Benvenuti, P. Chiggiato, F. Cicoira, and V. Ruzinov, "Decreasing surface outgassing by thin film getter coatings," *Vacuum*, vol. 50, no. 1-2, pp. 57–63, 1998.

[16] E. Belli, P. C. Pinto, G. Rumolo, A. Sapountzis, T. Sinkovits, M. Taborelli, B. Spataro, M. Zobov, G. Castorina, and M. Migliorati, "Electron cloud buildup and impedance effects on beam dynamics in the future circular e^+e^- collider and experimental characterization of thin TiZrV vacuum chamber coatings," *Phys. Rev. Accel. Beams*, vol. 21, p. 111002, 2018.

[17] K. Wasa, *Handbook of Sputter Deposition Technology.* Elsevier, 2012.

[18] D. M. Mattox, *Handbook of Physical Vapor Deposition (PVD) Processing.* Elsevier, 2010.

[19] R. Stuart, *Vacuum Technology, Thin Films, and Sputtering. An Introduction.* Academic Press, Inc., 1983.

[20] N. Matsunami et. al, "Energy dependence of the ion-induced sputtering yields of monatomic solids," *Atomic Data and Nuclear Data Tables*, vol. 31, pp. 1–80, 1984.

[21] D. Smith, *Thin film Deposition. Principles and Practice.* McGraw-Hill, Inc., 1995.

[22] A. E. Prodromides, C. Scheuerlein, and M. Taborelli, "Lowering the activation temperature of tizrv nonevaporable getter films," *Vacuum*, vol. 60, no. 1-2, p. 35, 2001.

[23] C. Benvenuti, P. Chiggiato, P. C. Pinto, A. Prodromides, and V. Ruzinov, "Influence of the substrate coating temperature on the vacuum properties of TiZrV non-evaporable getter films," *Vacuum*, vol. 71, p. 307, 2003.

[24] A. Prodromides, *Ph.D Thesis No. 2652.* Ph.d thesis no. 2652, Faculté Sciences de Base, Section de Physique, EPFL, 2002.

[25] C. Benvenuti, S. Calatroni, J. Carver, P. Chiggiato, H. Neupert, W. Vollenberg, S. Amorosi, and M. Anderle, "Study of the discharge gas trapping during thin film growth," *Proceeding of the Sixth European Vacuum Conference*, 1999.

[26] C. Benvenuti, P. Chiggiato, P. C. Pinto, A. E. Santana, T. Hedley, A. Mongelluzzo, V. Ruzinov, and I. Wevers, "Vacuum properties of TiZrV non-evaporable getter films," *Vacuum*, vol. 60, no. 1, pp. 57 – 65, 2001. The Sixth European Vacuum Conference.

[27] M. Ohring, *Materials Science of Thin Films.* Academic Press, 2001.

[28] P. C. Pinto, J. Ahlback, E. Al-Dmour, B. Bartova, M. Grabski, B. Holliger, S. M. dos Santos, V. Nistor, C. Pasquino, A. Sapountzis, M. Taborelli, and I. Wevers, "Development and production of non evaporable getter coatings for the vacuum chambers of the 3 GeV storage ring of MAX IV," in *Proceedings of IPAC*, (Richmond, USA), p. 3145, 2015.

[29] P. Chiggiato and P. C. Pinto, "TiZrV non-evaporable getter films: From development to large scale production for the Large Hadron Collider," *Thin Solid Films*, vol. 515, no. 2, p. 382, 2005.

[30] P. Chiggiato and R. Kersevan, "Synchrotron radiation-induced desorption from a NEG-coated vacuum chamber of ESRF beamline," *Vacuum*, vol. 60, no. 1-2, pp. 67–72, 2001.

[31] M. Ady, *Monte Carlo Simulation of ultra high vacuum and synchrotron radiation for particle accelerators*. PhD thesis, Ecole polytechnique federale de Lausanne (EPFL), 2016. These 7063.

[32] R. Kersevan, "Ageing of non-evaporable getter (NEG) thin film coatings," in *BPPC Meeting*, 2013.

[33] C. Steier, A. Anders, D. Arbelaez, J. Byrd, K. Chow, S. D. Santis, R. Duarte, J.-Y. Jung, T. Luo, A. Madur, H. Nishimura, J. Osborn, G. Pappas, L. Reginato, D. Robin, F. Sannibale, D. Schlueter, C. Sun, C. Swenson, W. Waldron, E. Wallen, and W. Wan, "Progress of the R-D towards a diffraction limited upgrade of the Advanced Light Source," in *Proceedings of IPAC*, (Richmond, USA), p. 1840, 2015.

[34] C. Garion and H. Kos, "Design of the CLIC quadrupole vacuum chambers," in *Proceedings of PAC*, (Vancouver, Canada), p. 363, 2009.

[35] A. Vorozhtsov and M. Modena, "Design and manufacture of a main beam quadrupole model for CLIC," in *IEEE Transactions on applied superconductivity, vol. 22, No 3*, 2012.

[36] P. F. Tavares, "MAX IV perspective," in *CREMLIN meeting*, 2018.

[37] A. Vorozhtsov, "Design study of the high gradient magnets for a future diffraction limited light source at MAX IV," in *Future Ligth Source*, 2018.

[38] A. Steier *et al.*, "Status of the conceptual design of ALS-U," in *IPAC 2018, Vancouver, Canada*, 2018.

[39] P. F. Tavares, E. Al-Dmour, A. Andersson, F. Cullinan, B. N. Jensen, D. Olsson, D. K. Olsson, M. Sjöström, H. Tarawneh, S. Thorin, and A. Vorozhtsov, "Commissioning and first-year operational results of the MAXIV 3 GeV ring," *Journal of Synchrotron Radiation*, vol. 25, pp. 1291–1316, Sep 2018.

[40] T. Porcelli, M. Puro, S. Raimondi, F. Siviero, E. Maccallini, P. Manini, and G. Bongiorno, "NEG coating deposition and characterisation of narrow-gap insertion devices and small-diameter chambers for light sources and particle accelerators," *Vacuum*, vol. 138, p. 157, 2017.

[41] L. Lain Amador, P. Chiggiato, L. Ferreira, V. Nistor, A. Perez Fontenla, M. Taborelli, W. Vollenberg, M.-L. Doche, and J.-Y. Hihn, "Development of copper electroformed vacuum chambers with integrated nonevaporable getter thin film coatings," *J. Vac. Sci. Technol. A*, vol. 36, no. 2, 2018.

[42] W. K. Kelley, J. W. Dini, and C. M. Logan *Plating Surf. Finish.*, vol. 69, no. 54, 1982.

[43] D. Hopkins, G. Koehler, H. Krapf, W. Cowden, J. Dini, W. Kelley, M. Prokosch, C. Steffani, J. Farmer, and A. Gardea, "Electroforming process development for a 33 GHz High-Gradient Accelerator," *Proceedings of the 1987 IEEE particle accelerator conference*, 1987.

[44] F. Arranz, B. Braas, M. Busch, M. Gonzlez, A. Muoz, B. Szcepaniak, L. Castro, P. Galn, D. Iglesias, J. Lapea, D. Lpez, I. Rucandio, D. Plaza, M. Garca, and B. Gmez, "Evaluation of the electroforming technique for IFMIF-EVEDA beam dump manufacturing," *Fusion Science and Technology*, vol. 60, no. 2, pp. 538–543, 2011.

[45] F. Arranz, M. Serrano, A. Muoz, B. Szcepaniak, B. Braas, O. Nomen, and J. Castellanos, "Stress strain curves for thick electroformed Cu pieces," *Fusion Engineering and Design*, vol. 127, pp. 17 – 22, 2018.

[46] P. Agostinetti, M. D. Palma, S. D. Bello, and et al., "Investigation of the thermo-mechanical properties of electrodeposited copper for ITER," *J. Nucl. Mater.*, vol. 417, 2011.

[47] N. Overman, D. Edwards, and C. Overman, "Majorana electroformed copper mechanical analysis," *PNNL-21315*, 2012.

[48] G. Malone, W. Hudson, B. Babcock, and R. Edwards, "Improved electroformed structural copper and copper alloys," Tech. Rep. NASA/CR–1998-20868, NASA, 1998.

[49] J. W. Dini and D. D. Snyder, "Electrodeposition of copper," in *Modern Electroplating* (M. Schlesinger and M. Paunovic, eds.), pp. 33–78, Hoboken, USA: John Wiley and Sons, fifth edition ed., 2010.

[50] M. Schwartz, *Handbook of Deposition Technologies for Films and Coatings Science*, ch. Deposition from Aqueous Solutions: An Overview, p. 506. William Andrew Publishing, 1994.

[51] E. F. Kern and M. Y. Chang *Trans. Am. Electrochem. Soc.*, vol. 41, no. 181, 1922.

[52] B. F. Rothschild, "Carbon treatment of pyrophosphate copper baths for improved printed wiring board production," *Plating Surf. Finish.*, vol. 66, no. 70, 1979.

[53] M. Hill and G. T. Rogers, "Polyethylene glycol in copper electrodeposition onto a rotating disk electrode," *J. Electroanal. Chem.*, vol. 86, no. 179, 1978.

[54] L. F. Spencer, "Surface preparation of metals," *Metal Finishing*, vol. 57, no. 5, p. 48, 1959.

[55] E. M. Dela Pena, *Electrodeposition of Copper using Additive-containing Low Metal Ion concentration Electrolytes for EnFACE Applications.* PhD thesis, University of Strathclyde, 2017.

[56] T. Moffat, D. Wheeler, and D. Josell, "Electrodeposition of copper in the sps-peg-cl additive system i. kinetic measurements," *J. Electrochem. Soc.*, vol. 151, no. 4, pp. C557–C561, 2004.

[57] M. Walker, L. Richter, and T. Moffat, "Competitive adsorption of peg, cl-, and sps/mps on cu: an in situ ellipsometric study.," *J. Electrochem. Soc.*, vol. 153, no. 8, p. C557C561, 2006.

[58] B. Basol and A. West, "Study on mechanically induced current suppression and super filling mechanisms," *Electrochem. Solid-State Lett.*, vol. 9, no. 4, pp. C77–C80, 2006.

[59] F. A. Lowenheim, *Modern Electroplating.* Wiley, New York,, 1974.

[60] A. S. Woodman and et al., "Proc 2nd international symp. on electrochemical technology applications in electronics," in *Electrochemical Society* (L. T. Romankiw, M. Datta, T. Osaka, and Y. Yamazaki, eds.), (NJ), p. 86, 1993.

[61] W. H. Safranek, *The Properties of Electrodeposited Metals and Alloys, 2nd Ed.* American Electroplaters and Surface Finishers Soc.,, 1986.

[62] J. W. Dini, "Electrodepositiona viable coating alternative," *Thin Solid Films*, vol. 95, no. 2, pp. 123–129, 1982.

[63] J. Farmer, "Electroforming process development for the twobeam accelerator," *Plating Surf. Finish.*, vol. 75, no. 48, 1988.

[64] W. Metzger, E. Knaak, and J. Hupe, "An acid copper plating solution with a single sulfur-free additive for high-tech applications," *Plating Surf. Finish.*, vol. 75, no. 64, 1998.

[65] C.-W. Liu, J.-C. Tsao, M.-S. Tsai, and Y.-L. Wang, "Effects of wetting ability of plating electrolyte on Cu seed layer for electroplated copper film," *Journal of Vacuum Science & Technology A*, vol. 22, no. 6, pp. 2315–2320, 2004.

[66] S. Gandikota, D. Padhi, S. Ramanathan, C. McGuirk, R. Emami, S. Parikh, G. Dixit, and R. Cheung, "Effects of wetting ability of plating electrolyte on cu seed layer for electroplated copper film," *Proc. of Int. Interconnect Technology Conference (IITC)*, p. 197, 2002.

[67] M. Kang and A. A. Gewirth, "Influence of additives on copper electrodeposition on physical vapor deposited (PVD) copper substrates," *Journal of the Electrochemistry Society*, vol. 150, no. 9, pp. C426–C434, 2003.

[68] R. D. Srivastava and S. Kumar, "Anodic impurities in electrodeposited copper," *Trans. Inst. Met. Finish*, vol. 50, no. 102, 1972.

[69] J. R. Denchfield, "Process for electroforming low oxygen copper," 1971.

[70] F. Schuler, H. A. Tripp, and M. J. Mullery, "Electrodeposited copper for elevated temperature usage," in *Copper Development Association-American Society for Metals*, (Cleveland, OH), 1972.

[71] W. E. G. Hansal and S. Roy, *Pulse Plating*. Bad Saulgau, Germany: Leuze Verlag KG, 2012.

[72] G. Devaraj and S. Guruviah, "Pulse plating," *Mater. Chem. Phys*, vol. 25, no. 439, 1990.

[73] A. J. Avila and M. J. Brown, "Design factors in pulse plating," *Plating*, vol. 57, no. 70, 1970.

[74] J. C. Puippe and N. Ibl, "Influence of charge and discharge of electric double layer in pulse plating," *J. Appl. Electrochem.*, vol. 10, 1980.

[75] V. A. Lamb, C. E. Johnson, and D. R. Valentine, "Physical and mechanical properties of electrodeposited copper," *J. Electochem. Soc.*, vol. 117, no. 9, pp. 291C–341C, 1970.

[76] T. Pearson and J. K. Dennis, "Effect of pulsed reverse current on the structure and hardness of copper deposits obtained from acidic electrolytes containing organic additives," *Surface and Coatinys Technology, 42 (1990) 6979*, vol. 42, pp. 69–79, 1990.

[77] K. Popov, D. Totovski, and M. Maksimovic, "Fundamental aspects of pulsating current metal eletrodeposition vii: The comparison of current density distributions in pulsating current and periodic reverse current electrodeposition of metals.," *Surf Tech*, vol. 19, no. 2, pp. 181–185, 1983.

[78] A. C. Merz, "Non-evaporable getter coating on small diameter vacuum chambers with application for particle accelerators," Master's thesis, Universidad federal de Santa Catarina, 2014.

[79] D. Muehle, "Non-evaporable getter pre-coated vacuum chambers," Master's thesis, Ecole Polytechnique Federale Lausanne, 2012.

[80] Dow, "Copper gleam pc."

[81] M. A. Streicher, "The dissolution of aluminium in sodium hydroxide solutions," *J. Electrochem. Soc.*, vol. 93, no. 6, pp. 285–316, 1948.

[82] N. Takeno, *Atlas of Eh-pH diagrams Intercomparison of thermodynamic databases*. National Institute of Advanced Industrial Science and Technology, 2005.

[83] E. McCafferty, *Introduction to Corrosion Science*. Springer Science +Business Media, LLC, 2010.

[84] T. C. Huang, *Concise Encyclopedia of Materials Characterization: 6.1 - XRF: X-Ray Fluorescence*. Pergamon Press Ltd., 1993.

[85] J. B. Bindell, *Concise Encyclopedia of Materials Characterization: 2.2 - SEM: Scanning Electron Microscopy*. Pergamon Press Ltd., 1993.

[86] M. A. Meyer, I. Zienert, and E. Zschech, *Electron backscatter diffraction: application to Cu interconnects in Top-view and cross section. Materials for information technology.* Springer, 2005.

[87] R. H. Geiss, *Concise Encyclopedia of Materials Characterization: 3.1 - EDS: Energy-Dispersive X-Ray Spectroscopy.* Pergamon Press Ltd., 1993.

[88] L. F. Dobrzhinetskaya, "Focused ion beam technique and transmission electron microscope studies of microdiamonds from the saxonian erzgebirge, germany," *Earth and Planetary Science Letters*, vol. 210, pp. 399–410, 2003.

[89] M. F. Toney, *Concise Encyclopedia of Materials Characterization: 4.1 - XRD: X-Ray Diffraction.* Pergamon Press Ltd., 1993.

[90] Wikipedia, "X-ray crystallography."

[91] P. van der Heide, *X-Ray Photoelectron Spectroscopy.* John Wiley and sons, Inc., 2012.

[92] I. Lindau, P. Pianetta, S. Doniach, and W. E. Spicer, "X-ray photoemission spectroscopy," *Nature*, vol. 250, no. 5463, pp. 214–215, 1974.

[93] C. Hauviller, "Design rules for vacuum chambers," *CERN document server*, p. 12 p, 2007.

[94] ASTM-E8M, "Standard test methods for tension testing of metallic materials," tech. rep., ASTM international, 2011.

[95] ASTM-E1876-09, "Standard test methods for dynamic young's modulus, shear modulus and poisson's ratio by impulse excitation method," tech. rep., ASTM international, 2009.

[96] ASTM-E112, "Standard test methods for determining average grain size," tech. rep., ASTM international, 2013.

[97] ASTM-E407, "Standard practice for microetching metals and alloys," tech. rep., ASTM international, 2011.

[98] K. Ping and A. Bushby, "Mechanical properties of electroformed copper," Tech. Rep. N RD 033-2389, Centre for Materials Research, Queen Mary, University of London,, 2009.

[99] D. Chapman, "High conductive copper," *Copper Development Association Publication No 122*, 2016.

[100] D. J. Marcinek, *Model of discontinuous plastic ow at temperature close to absolute zero.* PhD thesis, Cracow University of Technology, 2016.

[101] Innovatest, "Vickers hardness test." Catalog.

[102] H. P. Klug and L. E. Alexander, *X-Ray Diffraction Procedures: For Polycrystalline and Amorphous Materials.* Wiley, New York, USA: John Wiley and Sons, 1974.

[103] O. Malyshev and K. Middleman, "Test particle Monte-Carlo modelling of installations for NEG film pumping properties evaluation," *Vacuum*, vol. 83, no. 6, pp. 976 – 979, 2009.

[104] R. Kersevan and J.-L. Pons, "Introduction to Molflow+: New graphical processing unit-based Monte Carlo code for simulating molecular flows and for calculating angular coefficients in the compute unified device architecture environment," *J. Vac. Sci. Technol. A*, vol. 27, no. 4, 2009.

[105] X. Tingwei, J.-M. Laurent, and O. Grobner, "Monte Carlo simulation of the pressure and of the effective pumping speed in the large electron positron collider (LEP)," Tech. Rep. CERN-LEP-VA-86-02, CERN, Geneva, 1986.

[106] E. Fisher and M. Mommsen, "Monte Carlo computations on molecular flow in pumping speed test domes," *Vacuum*, vol. 17, no. 6, p. 309, 1967.

[107] A. de Jong and J. Niemantsverdriet, "Thermal desorption analysis: Comparative test of ten commonly applied procedures," *Surface Science*, vol. 233, no. 3, pp. 355 – 365, 1990.

[108] D. A. King, "Thermal desorption from metal surfaces: A review," *Surface Science*, vol. 47, no. 1, pp. 384 – 402, 1975.

[109] D. Rosenthal, "TDS," in *Modern methods in heterogeneous catalysis research*, 2011.

[110] P. Chiggiato, "Outgassing," in *CERN Accelerator School 2006*, (Platja d'Aro, Spain), May 2006.

[111] J. F. Moulder et al., *Handbook of X-ray Photoelectron Spectroscopy*. Perkin-Elmer Corporation, Physical Electronics Division, 1992.

[112] P. Massuti-Ballester, "Outgassing analysis of dierent copper materials for ultra-high vacuum by thermal desorption spectroscopy," Master's thesis, Universitat des Saarlandes - Leibniz Institut fur neue Materialien, 2017.

[113] C.-W. Liu, Y.-L. Wang, M.-S. Tsai, H.-P. Feng, S.-C. Chang, and G.-J. Hwang, "Effect of plating current density and annealing on impurities in electroplated Cu film," *Journal of Vacuum Science & Technology A*, vol. 23, no. 4, pp. 658–662, 2005.

[114] M. Paunovic and M. Schlesinger, *Fundamentals of Electrochemical deposition, Electrochemical Society series*. John Wiley and sons, 1998.

[115] V. V. Gubin, L. T. Zhuravlev, B. M. Platonov, and Y. Polukarov, "Hydrogen incorporation into electrolytic copper deposits obtained from sulphate solutions," *Soviet Electrochem.*, vol. 20, no. 5, p. 671, 1984.

[116] N. Fukumuro, T. Adachi, S. Yae, H. Matsuda, and Y. Fukai, "Influence of hydrogen on room temperature recrystallisation of electrodeposited cu films: thermal desorption spectroscopy," *Transactions of the IMF*, vol. 89, no. 4, pp. 198–201, 2011.

[117] F. Lallemand, L. Ricq, E. Deschaseaux, L. de Vettor, and P. Bercot, "Electrode-position of cobalt-iron alloys in pulsed current from electrolytes containing organic additives.," *Surface Coatings Technology*, vol. 197, no. 1, pp. 10–17, 2005.

[118] A. Rashidi and A. Amadeh, "Effect of electroplating parameters on microstructure of nanocrystalline nickel coatings," *J. Mater. Sci. Technol.*, vol. 26, no. 1, pp. 82–86, 2010.

[119] E. Taylor and M. Inman, "Electrodeposition of catalytic metals using pulsed electric fields," 2000.

[120] E. Taylor, C. Zhou, and J. Sun, "Pulse reverse electrodeposition for metallization and planarization of semiconductor substrates," 2005.

[121] N. Ibl, J. Puippe, and H. Angerer, "Electrocrystallization in pulse electrolysis," *Surface Technology*, vol. 6, no. 4, 1978.

[122] E. Michailova, I. Vitanova, D. Stoychev, and A. Milchev, "Initial stages of copper electrodeposition in the presence of organic additives," *Electrochimica Acta*, vol. 38, no. 16, pp. 2455 – 2458, 1993.

[123] S. Kruglikov, N. Kudriavtsev, G. Vorobiova, and A. Antonov, "On the mechanism of levelling by addition agents in electrodeposition of metals," *Electrochimica Acta*, vol. 10, no. 3, pp. 253 – 261, 1965.

[124] S. Kruglikov, N. Kudryavtsev, and R. Sobolev, "The effect of some primary and secondary brighteners on the double layer capacitance in nickel electrodeposition," *Electrochimica Acta*, vol. 12, no. 9, pp. 1263 – 1271, 1967.

[125] E. M. Dela Pena and S. Roy, "Electrodeposited copper using direct and pulse currents from electrolytes containing low concentration of additives," *Surface and Coatings Technology*, vol. 339, pp. 101 – 110, 2018.

[126] N. Imaz, E. Garca-Lecina, C. Surez, J. A. Dez, J. Rodrguez, J. Molina, and V. Garca-Navas, "Influence of additives and plating parameters on morphology and mechanical properties of copper coatings obtained by pulse electrodeposition," *Transactions of the IMF*, vol. 87, no. 2, pp. 64–71, 2009.

[127] N. Tantavichet and M. D. Pritzker, "Effect of plating mode, thiourea and chloride on the morphology of copper deposits produced in acidic sulphate solutions," *Electrochimica Acta*, vol. 50, no. 9, pp. 1849–1861, 2005.

[128] J. B. Marro, T. Darroudi, C. A. Okoro, Y. S. Obeng, and K. C. Richardson, "The influence of pulsed electroplating frequency and duty cycle on copper film microstructure and stress state," *Thin solid films*, vol. 621, pp. 91–97, 2017.

[129] H. J. S. Sand, "On the concentration at the electrodes in a solution, with special reference to the liberation of hydrogen by electrolysis of a mixture of copper sulphate and sulphuric acid," *Phis. Mag.*, vol. 6, 1901.

[130] J. Rolet, *Influence de la forme de l'onde de polarisation sur la microstructure et les proprits de revtements lectrolytiques labors base de chrome trivalent.* PhD thesis, Ecole doctorale Carnot-Pasteur, 2017.

[131] M. S. Kang, S.-K. Kim, K. Kim, and J. J. Kim, "The influence of thiourea on copper electrodeposition: Adsorbate identification and effect on electrochemical nucleation," *Thin Solid Films*, vol. 516, no. 12, pp. 3761 – 3766, 2008.

[132] E. M. Dela Pena and S. Roy, "Electrochemical effect of copper gleam additives during copper electrodeposition," *Transactions of the IMF*, vol. 95, no. 3, pp. 158–164, 2017.

[133] J. T. Hinatsu and F. R. Foulkes, "Diffusion coefficients for copper (11) in aqueous cupric sulfate-sulfuric acid solutions," *J. Electrochem. Soc.*, vol. 136, no. 1, 1989.

[134] Y. Fukai, M. Mizutani, S. Yokota, M. Kanazawa, Y. Miura, and T. Watanabe, "Superabundant vacancyhydrogen clusters in electrodeposited Ni and Cu," *Journal of Alloys and Compounds*, vol. 356-357, pp. 270–273, 2003.

[135] Y. Fukai, "Formation of superabundant vacancies in MH alloys and some of its consequences: a review," *Journal of Alloys and Compounds*, vol. 356-357, pp. 263–269, 2003.

[136] Y. Fukai, "Hydrogen-induced superabundant vacancies in metals: Implication for electrodeposition," *Defect and Diffusion Forum*, vol. 312-315, pp. 1106–1115, 2011.

[137] A. Martinsson and K. Swerea, "Hydrogen in oxygen-free, phosphorus-doped copper," Tech. Rep. Report TR-13-09, INIS, 2013 2013.

[138] H. Nakamura, S. Ohira, W. Shu, M. Nishi, T. Venhaus, R. Causey, D. Hyatt, and R. Willms, "Tritium permeation experiment using a tungsten armored divertor-simulating module," *Journal of Nuclear Materials*, vol. 283-287, pp. 1043 – 1047, 2000. 9th Int. Conf. on Fusion Reactor Materials.

[139] H. Wipf, "Solubility and diffusion of hydrogen in pure metals and alloys," *Physica Scripta*, vol. T94, no. 1, p. 43, 2001.

[140] S. A. Acharya, V. M. Gaikwad, V. Sathe, and S. K. Kulkarni, "Influence of gadolinium doping on the structure and defects of ceria under fuel cell operating temperature," *Applied Physics Letters*, vol. 104, no. 11, p. 113508, 2014.

[141] F. C. Nix and D. MacNair, "The thermal expansion of pure metals: Copper, gold, aluminum, nickel, and iron," *Physical Review*, vol. 60, no. 8, pp. 597–605, 1941.

[142] C. Q. Sun, "An approach to local band average for the temperature dependence of lattice thermal expansion," Tech. Rep. arXiv:0801.0771, Nanyang Technological University, 2008.

[143] T. Schmidt and M. Calvi, "APPLE X undulator for the SwissFEL soft X-ray beamline Athos," *Synchroton Radiation News*, vol. 31, no. 3, 2018.

[144] L. Schulz, "New design for SwissFEL undulator chambers." indico.cern.ch, June 2012. Paul Scherrer Institut.

[145] R. Ganter, "Concept of vacuum chamber of Athos, PSI." Discussion.

[146] S. Omolayo, "Vaccum chamber concept for ALS-U narrow gap chambers from Berkeley Lab accelerator." Discussion.

[147] CLIC team, "A multi-TeV linear collider based on CLIC technology, CLIC conceptual design report," tech. rep., CERN, 2012.

[148] M. Pourbaix, *Atlas of Electrochemical Equilibria in Aqueous Solutions, Volume 1.* National Association of Corrosion Engineers, 1966.

[149] Hiden-Analytical, "Mass spectrometers for thin films, plasma & surface engineering," Tech. Rep. Technical data sheet 184/3, Hiden Analytical Ltd., 420 Europa Boulevard Warrington WA5 7UN England, 2016.

[150] C. Alcock, V. P. Itkin, and M. K. Horrigan, "Vapor pressure of the metallic elements," *Canadian Metallurgical Quarterly*, vol. 23, p. 309, 1984.

Abstract

Keywords: Vacuum, getter, electroforming, pump

Titanium Zirconium Vanadium (TiZrV) thin film coatings are used in particle accelerators and synchrotron light sources to maintain ultra-high vacuum conditions. They are deposited on the internal walls of the vacuum chambers, transforming them from a gas source into a chemical pump. The trend in electron accelerators design consists in approaching the poles of the steering magnets close to the electron beam. This implies reducing the bore hosting the vacuum chamber and using very small diameter vacuum pipes. The application of physical vapor deposition (PVD) in such small diameter chambers becomes then very difficult. The aim of this project is to develop a novel procedure of coating/assembly, using a sacricial aluminium mandrel as substrate of the thin film together with the creation of a surrounding copper chamber by electroforming. The first part of the study deals with the production and characterization of the electroformed chambers. The mechanical robustness of the assembly is checked, and the film characterization is performed by secondary electron microscopy (SEM), X-ray diffraction analysis (XRD), X-ray Fluorescence Spectroscopy (XRF) and X-Ray Photoelectron Spectroscopy (XPS). Moreover, the pumping performance is measured and compared with reference values of coatings produced by the standard PVD technique. The second part of the study evaluates the impurities included during the different steps of the process: PVD coating, electroforming and chemical etching of the mandrel. Thermal desorption spectroscopy and XPS depth profiling allow to quantify the impurities in the electroformed copper and the TiZrV thin film. Furthermore, the presence of hydrogen trapped in the electroformed copper is studied for different copper sulphate baths. One of them, without additives, require the use of pulse currents. The electrochemical behaviour of the bath allows the selection of different pulse parameters, derived from typical situations on the transient curves. Finally, the development of real-scale prototypes was achieved with the creation of a 4 mm diameter, 2 meters TiZrV coated vacuum chamber, which is unrivalled up to date.

Résumé

Mots clés : Vide, getter, électroformage, pompe

Des couches minces co-deposées de Titanium Zirconium Vanadium (TiZrV) sont utilisées dans les accélérateurs de particules et les sources de lumière synchrotron pour maintenir les conditions d'ultravide. Elles sont pulvérisées sur les parois internes des chambres à vides, transformant celles-ci en pompe chimique de gaz. La tendance dans la conception d'accélérateurs d'électrons consiste à approcher les pôles des aimants de direction au plus près du faisceau d 'électrons. Cela implique la réduction du diamètre des tubes hébergeant le vide et nécessite l'utilisation de très petits diamètres pour les chambres à vide. L 'application du dépôt physique en phase vapeur (PVD) dans un aussi faible diamètre devient alors très difficile. Le but de ce projet est de développer une nouvelle procèdure de dépôt couplé à l'assemblage, en utilisant un mandrin sacrificiel en aluminium comme substrat de la couche mince en même temps que la création autour de lui de la chambre à vide elle-même par électroformage de cuivre. La première partie de l'étude concerne la production et la caractérisation de chambre de cuivre électroformées. La robustesse mécanique de l'assemblage complet a été validée, et les caractéristiques du film lui-même ont été etudiées par microscopie électronique à balayage (MEB), diffraction des rayons X (DRX), spectrométrie de fluorescence-X (XRF) et spectrométrie de photoélectrons X (XPS). De plus, les performances de pompage chimique des gaz des nouvelles chambres à vide ainsi élaborées sont mesurées et comparées avec des valeurs de références de revêtements déposés par des procédures classiques. La deuxième partie de l'étude concerne l'évaluation des impuretés incluses lors des différentes étapes du procédé: le revêtement PVD du getter, l'électroformage et l'étape de dissolution chimique du mandrin. La spectrométrie de désorption thermique et les profils de composition en épaisseur par XPS permettent de quantifier les impuretés dans le cuivre électroformé et dans le film de TiZrV. De plus, la présence d'hydrogène emprisonné dans le cuivre électroformé est étudiée à partir de différents bains à base de sulfate de cuivre. L'un d'entre eux, sans additifs, nécessite l'utilisation de courants pulsés. Le comportement électrochimique du bain permet la sélection de différents paramètres de séquences de pulses, dérivées de situations typiques partir des courbes transitoires. Finalement, l'objectif de realisation de prototypes de taille réelle a été atteint avec la création de chambres à vide revêtues de TiZrV de 2 mètres de long et 4mm de diamètre, ce qui n'a pas d'équivalent à ce jour.